Università degli Studi della Tuscia di Viterbo

Department of Economics, Engineering, Society and Business

PhD Course in

Engineering for Energy and Environment (curriculum Biosystems and Environment)- **XXXVII cycle**

Optical methods for the detection of phenolic pollutants in aqueous matrices

Scientific Disciplinary Sector
(s.s.d FIS/07)

PhD Thesis of:
Dr. Pauline Conigliaro

PhD Coordinator:
Prof. Andrea Luigi Facci

Tutor:
Prof. Ines Delfino

A.Y. 2024/2025

Tesi redatta con il sostegno finanziario del programma FSE-REACT-EU, PON "Ricerca e Innovazione" 2014-2020 (D.M. 1061/2021) Azione IV.5 "Dottorati su tematiche Green"

INDEX

ABSTRACT

Water pollution, especially by phenolic compounds such as phenol, bisphenol A, catechol, resorcinol and hydroquinone, poses significant risks to both human health and the environment; consequently, they are considered priority pollutants. In this framework, the interest in studying innovative schemes for phenol compound detection based on optical methods is increasing because of the advantages in terms of versatility and economic efficiency compared to other methods, such as traditional chromatographic techniques, which are expensive and require specialised equipment and trained personnel. The PhD project was devoted to investigating optical methods for the detection of phenolic compounds by exploiting biosensing and sensing approaches, and to explore the potential of a better understanding of the interaction of phenols with biomaterials (especially cell membranes) in the view of an innovative optical detection scheme. In the PhD project, catechol, a common phenol derivative, was selected and used as a model compound for detection. Regarding the biosensing approach, the attention as a biological element was focused on utilising laccase from *Trametes versicolor*, which can oxidize phenolic substrates, thereby transforming them into less toxic compounds, which have, together with laccase, peculiar optical properties well suited for optical biosensing schemes. By exploiting these properties, biosensing schemes, based on the use of laccase properties to monitor catechol through absorbance and fluorescence measurements, were investigated, highlighting the potential of fluorescence spectroscopy. For the optical sensing scheme, Surface-Enhanced Raman spectroscopy (SERS), a variant of Raman spectroscopy based on the Raman signal enhancement by using nanostructured substrates, was considered. Accordingly, a SERS-based sensing scheme was studied, using both commercial and homemade SERS substrates to identify the most effective one for detecting catechol in an aqueous matrix.

These processes were investigated to study the potential application of the effects of catechol exposure on biological systems for designing sensing schemes. To this end, two models were tested: one in a pure liquid-condensed phase and the other with coexisting liquid-condensed and liquid-expanded phases. The impact of catechol exposure was evaluated using compressibility measurements (π-A isotherms) and atomic force microscopy (AFM). The presence of catechol on lipid monolayers causes evident effects, promising for understanding its influence on membrane functionality and relevance in biological processes.

KEYWORDS: Water pollution, optical biosensors, optical sensors, catechol, membrane models.

RIASSUNTO

L'inquinamento delle acque, soprattutto da parte di composti fenolici come fenolo, bisfenolo A, catecolo, resorcinolo e idrochinone, comporta rischi significativi sia per la salute umana che per l'ambiente. Per questo motivo questi composti sono considerati inquinanti prioritari. In questo contesto, l'interesse per lo studio di nuovi schemi di rilevamento dei composti fenolici basati su metodi ottici è in aumento considerati i vantaggi in termini di versatilità ed efficienza economica di questi metodi rispetto, ad esempio, alle tecniche cromatografiche tradizionali, che sono costose, richiedono particolari attrezzature e personale qualificato. Obiettivo dell'attività di ricerca svolta durante il dottorato è stato lo studio di diversi schemi di rivelazione di composti fenolici basati su metodi ottici, anche investigando approcci basati su sistemi ibridi, ovvero basati anche sull'uso di elementi biologici (biosensing). Inoltre, è stata investigata l'interazione dei fenoli con i biomateriali (in particolare le membrane cellulari) per esplorare il potenziale della migliore descrizione di tali processi per lo sviluppo di nuovi schemi di rilevamento.

Nel progetto di dottorato, il catecolo, un comune derivato del fenolo, è stato scelto e utilizzato come composto modello per il rilevamento. Per quanto riguarda l'approccio basato sull'uso di sistemi ibridi, l'attenzione come elemento biologico si è concentrata sulla laccasi da *Trametes versicolor*, in grado di ossidare i substrati fenolici, trasformandoli così in composti meno tossici che, insieme alla laccasi, possiedono proprietà ottiche peculiari. Sfruttando queste proprietà, sono stati studiati schemi di rivelazione basati sull'uso delle proprietà della laccasi per monitorare il catecolo attraverso misure di assorbanza e fluorescenza, i cui risultati hanno evidenziato il potenziale della spettroscopia di fluorescenza. Per lo schema di rilevamento ottico, è stata presa in considerazione la tecnica SERS (Surface-Enhanced Raman spectroscopy), una variante della spettroscopia Raman basata sull'amplificazione del segnale mediante l'utilizzo di substrati nanostrutturati. Di conseguenza, è stato studiato uno schema di rilevamento basato sul SERS, utilizzando substrati SERS commerciali e fatti in casa, per identificare quello più efficace per rilevare il catecolo in una matrice acquosa. Inoltre, sono stati studiati gli effetti dell'esposizione al catecolo in membrane modello, che imitano l'organizzazione lipidica naturale, per comprendere le potenzialità di una migliore conoscenza di questi processi nella realizzazione di nuovi approcci di sensing ottico. A tale fine sono stati testati due modelli: uno in fase liquida-condensata pura e l'altro con fasi liquide-condensate e liquide-espanse coesistenti. L'impatto dell'esposizione al catecolo di tali sistemi è stato valutato mediante misure di compressibilità (isoterme π-A) e microscopia a forza atomica (AFM). La presenza del catecolo nei monostrati lipidici provoca effetti evidenti, promettenti per la comprensione della sua influenza sulla funzionalità delle membrane e della sua rilevanza nei processi biologici.

PAROLE CHIAVE: Inquinamento idrico, biosensori ottici, sensori ottici, catecolo, membrane modello.

INTRODUCTION

In recent years, water pollution has threatened the quality of human life and hurt environmental health. Attention to issues related to the environment and its pollution has become of major interest (Delfino, 2021; Lin, 2022; du Plessis, 2022). Phenolic compounds, such as phenol, bisphenol A, catechol, resorcinol, and hydroquinone, which are released in wastewater and can even contaminate drinking and surface water, have recently attracted the attention of the scientific community and have been classified as priority pollutants (Priority Substances and Certain Other Pollutants according to Annex II of Directive 2008/105/EC. European Commission. Available online: http://data.europa.eu/eli/dir/2008/105/oj (accessed on 15 April 2025). They are produced in various processes, from paper production to pharmaceutical applications, with dangerous acute and chronic health effects. It is crucial to monitor their levels in local wastewater samples, test their biological activity, and develop new sustainable and environmentally friendly strategies for their removal and detection.

Chromatographic techniques, such as gas chromatography (GC), liquid chromatography (LC), and capillary electrophoresis (CE), are commonly used methods for detecting phenolic compounds in water (Marrubini, 2005; Hong-Wei, 2012). However, these methods have disadvantages, such as the need for expensive equipment and specialized operators and the inability to perform in situ measurements, which fuels the interest in developing new methods for sensing phenols in various matrices. In this context, optical sensing schemes can play a key role since they can provide non-invasive tools, and their flexibility and range of application are continuously increasing, thanks to the continuous development of innovative light sources and detectors at low cost.

In this framework, interest in studying different schemes for phenol compound detection based on optical methods is increasing because of their advantages in terms of versatility and economic efficiency compared to other methods. In the specific case of phenol detection, optical biosensing and optical sensing schemes are considered, which can be further developed to realize biosensors and sensors for phenol detection.

A biosensing scheme typically involves the integration of a biological recognition element with a physicochemical transducer to detect a target analyte with high specificity and sensitivity. The biological recognition component, such as an enzyme, antibody, nucleic acid, or molecularly imprinted polymer-is responsible for the selective interaction with the analyte of interest. Upon recognition, this interaction induces a measurable change in the transducer element, which converts the biochemical event into a quantifiable signal. In optical biosensors, this signal may be manifested

as a change in absorbance, fluorescence, chemiluminescence, or refractive index, depending on the nature of the detection system. The transduced signal is then processed and correlated to the analyte concentration through a calibration model. Key performance parameters of a biosensing scheme include sensitivity, selectivity, limit of detection, response time, and stability. The design and optimization of each component in the scheme are crucial for achieving robust analytical performance, particularly in complex real-world samples such as environmental matrices or biological fluids.

Regarding optical sensing schemes not employing the use of biomolecules, in recent decades, vibrational spectroscopy techniques, including Raman spectroscopy, have gained ground for the optical detection of phenolic compounds. These techniques provide information on the vibrational energy levels associated with the functionality of the sample examined. Furthermore, the design and fabrication of nanostructured substrates has enabled the development of complementary techniques, such as surface-enhanced Raman spectroscopy (SERS), a variant of Raman scattering used for the chemical analysis of compounds (Pilot, 2018). It is a very active research field in which new nanomaterials are being developed to improve the reliability and sensitivity of experiments. This approach exploits the effect of Raman signal amplification by metallic nanostructures (e.g., gold or silver nanoparticles). Metal plasmonic nanomaterials support localized surface plasmon resonance (LSPR), which is responsible for signal amplification (Abin, 2022). The advantages of SERS spectroscopy include the simplicity of sample handling, the speed of analysis and the identification of the analyte *in situ*. A crucial aspect for designing a SERS-based sensing scheme is the selection of the substrate for the specific application.

Innovative sensing schemes could be designed for detecting phenol in specific matrices if their interaction with biosystems can be better described.

This is the framework of the PhD research activity, devoted to the study of potential optical sensing and biosensing schemes for the detection of catechol, selected as a representative phenol of interest. In addition, the interaction of catechol with membrane models was investigated, aiming at opening the root for detecting phenols by using new approaches based on a more detailed knowledge of this interaction.

The first step for the biosensing scheme investigation was to evaluate the possibility of using laccase's peculiar properties in the study for monitoring catechol; accordingly, absorbance and fluorescence measurements were made in the ultraviolet-visible range to assess the possibility of using the changes produced in the spectra of laccase and/or catechol and/or other products of the reaction involving the phenol and the enzyme to monitor the presence of this substrate. Laccase from *Trametes versicolor* was used during the study.

To design a SERS-based sensing scheme, we analysed and studied the characteristics of some commercial SERS substrates (i.e. substrates with nanostructures and patterns suitably designed to obtain an effective Surface-Enhanced Raman signal) and one home-made SERS substrate and tested their potential for catechol detection (Baumberg, 2017).
To study the effects of catechol exposure on biological systems, two membrane models were employed to mimic the lipid organisation of natural cell membranes, with the potential application in designing new phenol detection schemes (Schweigert, 2001).

This PhD thesis work is therefore organized as follows:

a) The first chapter describes the properties and general characteristics of phenols, their applications in industry and their effects on human health and the environment. Some knowledge on the physicochemical properties of laccase and the mechanisms of interaction with phenols is provided.
b) In the second chapter, the optical techniques underlying the detection processes are reported. The basic principles and spectral characteristics of absorption and fluorescence spectroscopies, as a tool for identifying biosensing schemes, are described. Attention is then on the study of vibrational spectroscopies, including Raman and SERS spectroscopies, the focus of this PhD project.
c) In the third chapter, the main biosensors and optical sensors for catechol detection based on absorption, fluorescence, Raman and SERS spectroscopies reported in the literature are described.
d) In the fourth chapter, the membrane models are introduced along with the main experimental approaches for studying their characteristics and their interaction with molecules, such as tensiometry and ellipsometry techniques. We then focus on lipid monolayers, the DPPC (1,2-dipalmitoyl-sn-glycero-3-phosphocholine) in the pure liquid-condensed phase and the DPPC-DOPC (1,2-dioleoyl-sn-glycero-3-phosphocholine) mixture, in coexisting, condensed liquid and expanded liquid phase, which are the subject of our study. To assess the effects of phenols on lipid monolayers, atomic force microscopy (AFM) was used, as a decisive technique for studying the structural properties of biological molecules at the nanoscale and sub-nanoscale.
e) The fifth chapter describes the materials used and the instrumentation employed to perform the experiments.
f) In the sixth chapter, the results obtained during the PhD project on optical methods for catechol detection in aqueous matrices, and the analysis of their effects on membrane models are reported and discussed.

g) Finally, the main conclusions are reported, identifying possible future developments.
h) A summary of the research periods spent outside the University of Tuscia during the PhD and of the outcomes of the research activity is reported in the appendix.

1. The impact of phenols on the environment and human health

1.1 Properties and characteristics of phenols

Phenolic compounds are one of the classes of bioactive molecules most studied by the scientific community for numerous applications. From a structural point of view, they consist of a phenolic part, which contains one or more hydroxyl groups (-OH) attached to a carbon atom in a benzene ring (Al Mamari, 2022); the structures of some phenols of interest, namely bisphenol A, catechol, resorcinol, and hydroquinone, are shown in Figure 1. This unique structural motif imparts a range of physicochemical properties that are critical to both their reactivity and detectability. One of the most notable features of phenols is their relatively high acidity compared to aliphatic alcohols, attributed to the resonance stabilization of the phenoxide ion formed upon deprotonation. This resonance delocalization facilitates interactions with various reagents and functional groups, making phenols versatile targets in chemical sensing and analytical applications (Olasz, 2005).

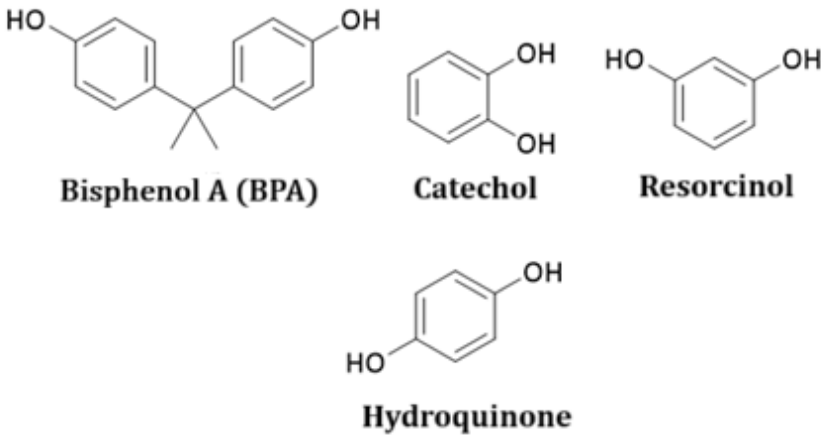

Figure 1. Chemical structure of bisphenol A (BPA), catechol, resorcinol and hydroquinone.

In aqueous environments, the solubility of phenols varies depending on the number and type of substituents attached to the aromatic ring. Lower molecular weight phenols are moderately soluble due to hydrogen bonding, while hydrophobic substitutions decrease solubility and influence their partitioning behaviour in complex matrices.

Phenols display strong absorbance in the ultraviolet region due to π-π* transitions within the aromatic system, and in some cases, n-π* transitions associated with the hydroxyl group. These spectral characteristics enable sensitive detection via UV-Vis absorption spectroscopy. Additionally, many

phenols can undergo derivatization or complexation with chromogenic or fluorogenic reagents, leading to changes in absorbance or fluorescence that form the basis of colorimetric and fluorometric sensing strategies. Furthermore, the propensity of phenolic compounds to participate in redox reactions can be exploited in the development of chemiluminescent or electrochemiluminescent sensors.

1.2 Natural and industrial production of phenols

In nature, phenols are known to play a crucial role in the defence of plants against ultraviolet (UV) radiation, pathogens, and other predators, as well as in pigmentation and interactions with the environment. They are mainly found in fruit, legumes, vegetables, tea, wine and coffee and are responsible for the organoleptic characteristics of plant foods. They are biosynthesized via the shikimate and phenylpropanoid pathways, leading to a wide array of secondary metabolites including flavonoids, lignins, and tannins. In ecosystems, phenols can also result from the microbial degradation of organic matter, contributing to the phenolic load in soils and aquatic systems (Ahmaruzzaman, 2024).

Industrially, phenols are significant chemical intermediates. The primary method of production is the cumene process, which involves the oxidation and acid-catalyzed cleavage of cumene (isopropylbenzene), yielding phenol and acetone. Other methods include the hydrolysis of chlorobenzene and the catalytic oxidation of benzene, both dependent on fossil fuel feedstocks. Increasing demand for phenol-based products and energy has led to higher oil production and, consequently, large volumes of phenol-containing industrial wastewater (Helmy, 2015; Salehi, 2021; Delfino, 2021; Mainali, 2020).

Phenols are used across multiple sectors. In the pharmaceutical and cosmetics industries, certain phenolic compounds are valued for their biological activities (Taofiq, 2019). In the packaging and food industries, their antioxidant and antimicrobial properties are leveraged to enhance product shelf life (Jia, 2017; Mark, 2019). The cosmetics industry has particularly focused on natural phenolics as safer alternatives to synthetic additives (Soto, 2015). Compounds like anthocyanins and phenolic acids (e.g., gallic acid, caffeic acid) have been incorporated into packaging films to provide UV protection and inhibit bacterial growth (Wang, 2019; Zeng, 2019).

The rapid and large-scale industrial production of phenols has resulted in increased hazardous waste generation. Significant quantities of phenols enter wastewater, eventually contaminating natural water sources and drinking water (Albuquerque, 2021; Delfino, 2021; Mainali, 2020; Gami, 2014).

The persistent nature of many phenols, combined with their bioactivity, has raised environmental and public health concerns, necessitating better detection and waste management strategies.

Several phenols are of environmental and toxicological interest because of their increasing use in the industrial application and because of their specific characteristics. Among the others, we can found bisphenol A, catechol, resorcinol, and hydroquinone (whose structure was shown in Figure 1). Bisphenol A (BPA) is a synthetic compound with endocrine activity and is one of the most extensively produced substances worldwide. It is used in producing polycarbonate plastics and epoxy resins and is commonly found in milk containers for children and water bottles (İyigündoğdu, 2020). Exposure to BPA primarily occurs through consuming food and beverages contained in recycled bottles, epoxy-coated cans, and polycarbonate containers where BPA has leached (Mokra, 2017; Mita, 2011; Errico, 2014). Resorcinol can be obtained by distillation of Brazilian wood extract or through synthetic fusion processes. Its production mainly occurs in the rubber industry (Suresh, 2012). Significant exposure to resorcinol occurs through cosmetics, particularly in hair dyes and dermatological products. Catechol (or pyrocatechol, 1,2-dihydroxybenzene) is a crystalline compound whose chemical formula is $C_6H_6O_2$; it is one of the main phenol derivatives and is involved in the benzene metabolism (Vishwanath, 2022). Obtained for the first time in 1839 by Reinsch through the dry distillation of catechin, it is today produced industrially from phenol (Morash, 2022). It is used as a matter first in the synthesis of polymerization inhibitors, perfumes, flavoring substances, pesticides, products for photographic development, oxidizing agents, and analytical reagents. In nature, it is present in raw sugar, in wood, in various plant species (e.g. eucalyptus) and in coal. The catechol and many of its derivatives can be obtained in the dry distillation of tannins, lignin, wood and bituminous products. Catechol forms colorless monoclinic crystals and is easily soluble in water, cold or lukewarm and in hydrophilic organic solvents such as ethanol or acetone. It dissolves more difficult in hydrophobic solvents, such as benzene or chloroform, requiring effective heating. Although information on catechol is available, its toxicity is not yet fully understood (Morash, 2022). Hydroquinone is the primary metabolite of benzene, featuring two hydroxyl groups attached to a benzene ring in the para position (Vishwanath, 2022). It is produced through oxidation processes or by the alkylation of benzene with propylene to isolate the para isomer (Raff, 1966), followed by an oxidation process and treatment with an acid to produce hydroquinone and acetone (IARC, 1977). Hydroquinone is used in various fields, including as a photographic developer and in motor fuels.

1.3 Relevant effects of phenols on environmental and human health

The uncontrolled release of phenols into the environment contributes significantly to hazardous waste and water contamination, particularly in regions with inadequate wastewater treatment (Ramos, 2021). Phenols are found in industrial effluents, agricultural runoff, and natural waters, where they can harm microbial life and disrupt aquatic ecosystems by reducing dissolved oxygen levels. Persistent phenols may infiltrate groundwater, damaging cells, disrupting DNA synthesis, and accumulating in food chains (Pradeep, 2015).

While dietary intake of natural phenols (from fruits and vegetables) can have beneficial antioxidant effects, industrial phenols can be toxic. They generate oxidative stress, contributing to serious health issues such as cancer, cardiovascular disease, neurological disorders, hypertension, and diabetes (Caleja, 2017; Durazzo, 2019). Phenols like BPA are endocrine disruptors, and exposure through contaminated food or water is a major concern (İyigündoğdu, 2020).

Phenolic compounds in drinking water can react with chlorine during treatment to form toxic chlorophenols and polychlorophenols, affecting taste and posing health risks (Qu, 2010). Conventional water treatment methods are often insufficient to remove such micropollutants (Ramos, 2021). For this reason, the European Commission and the U.S. Environmental Protection Agency (US EPA) have classified phenolic compounds as priority pollutants (https://www3.epa.gov/region1/npdes/permits/generic/priority_pollutants.pdf), Due to the high toxicity of some phenols, the World Health Organisation (WHO) has set a threshold of 9.08 µM for phenolic compounds in drinking water (WHO, 2017).

The scientific community has highlighted the need to monitor and reduce the presence of phenolic compounds in surface and drinking water, improve treatment efficiency, and develop new water quality standards to protect the environment and human health. Chromatographic techniques (for example, Gas Chromatography, Gas Chromatography-Mass Spectrometry (GC-MS) and High-Performance Liquid Chromatography) are commonly used methods to detect phenolic compounds. As can be seen in Table 1, with these techniques, it is possible to work in a range from 0.03 to 5.72 µM. However, these methods present some disadvantages, such as being very time-consuming, requiring expensive equipment and specialized operators and not allowing for *in situ* measurements. For all these reasons, there is an interest in identifying simple, sensitive, specific, and accurate optical methods for detecting phenolic compounds in the aqueous matrix.

Phenolic compounds	Limit of detection (LOD)	Techniques	References
Catechol	0.9 µM	HPLC/GC-MS	(Marrubini, 2005)
Resorcinol	0.03 µM	HPLC	(WU, 2012)
	5.72 µM	HPLC	(De, 2014)
Hydroquinone	0.4 µM	HPLC	(Marrubini, 2005)
	0.2 µM	HPLC	(Lin, 2005)

Table 1. Ranges of LOD parameters for detecting phenolic compounds with chromatographic techniques.

1.4 Characteristics and properties of laccases and their interaction with phenols

Laccase (EC 1.10.3.2, p-diphenol: dioxygen oxidoreductase) is part of the multi-copper oxidase (MCO) superfamily, which comprises a different group of enzymes with varying substrate specificities and biological roles. Identified as one of the earliest enzymes, it was first discovered in 1883 in a Chinese lacquer tree (*Rhus vernicifera*) (Yoshida, 1883). Over nearly 140 years of research, these copper-dependent enzymes' distinctive properties and significant functions have been extensively studied. The first bacterial laccase, isolated from the rice rhizosphere in 1993, came from *Azospirillum lipoferum* (Givaudan, 1993). In nature, laccases primarily contribute to lignin polymerization and degradation. However, they are also key players in other biological processes, as lignification is vital for maintaining the integrity and mechanical strength. Laccases also help plants respond to environmental stressors and aid their defence mechanisms, facilitating wound repair, iron metabolism, and the polymerization of phenolic compounds (Janusz, 2020; Zhang, 2021).

As of now, the BRENDA database has documented approximately 280 laccases (http://www.brenda-enzymes.org/, accessed 14 April 2025), predominantly found in fungi (Basidiomycetes and Ascomycetes) (Hoegger, 2006), but also in bacteria, insects, and algae (Debnath, 2020). Laccases can oxidize a wide variety of compounds, including mono-, di-, and polyphenols, aromatic and aliphatic amines, hydroxyindoles, benzenethiols, carbohydrates, and inorganic/organic metal complexes (Debnath, 2020; Karaki, 2017). This versatility in substrate oxidation and using oxygen as the terminal electron acceptor gives laccases wide-ranging applications in various industries and environmental cleanup. Laccases can oxidize phenolic compounds, such as resorcinol (*m*-benzenediol), hydroquinone (*p*-benzenediol) and catechol (*o*-benzenediol), converting them into less carcinogenic quinones (*m,p,o*-quinone) according to the following reaction (Portaccio, 2006):

$$o,m,p\text{-benzenediol} + \frac{1}{2}\,O_2 \xrightarrow{Laccase} o,m,p\text{-quinone} + H_2O \quad (1)$$

where oxygen is reduced directly to water, without producing hydrogen peroxide as an intermediate. Numerous crystallographic studies have explored the structure of laccases, particularly those from fungi and bacteria. However, laccases derived from plants and animals are challenging to crystallize due to their scarcity and intricate purification processes. Despite differences in taxonomy and substrates, the molecular architecture of laccases remains consistent across all polyvalent copper oxidases (Wang, 2021; Dwivedi, 2011). Their domains and amino acid sequences share commonalities with other multivalent copper oxidases, featuring relatively simple three-dimensional structures predominantly composed of beta-sheets and loops. The 3D crystal structure of *Trametes versicolor* was first reported in 2002 (Piontek, 2002). Most laccases contain four copper atoms, essential for the redox process, distributed across three distinct sites (T1, T2, and T3), which are classified based on their spectroscopic properties. The T1 site features trigonal coordination with histidine and cysteine as equatorial ligands, while leucine or phenylalanine serve as axial ligands (Wang, 2019), and is known to absorb electromagnetic radiation at around 600 nm. At the T2 site, copper is coordinated with two histidines and a water molecule, whereas the T3 site includes three histidines and a hydroxyl bridge linking two copper atoms. The T3 site is characterized by an absorption band around 330 nm. Together, these form a trinuclear center responsible for catalyzing oxygen reduction to water. As a representative example of the distribution of the amino acids of the catalytic site, the structure of laccase from *T. versicolor* is shown in Figure 2 (Arregui, 2019).

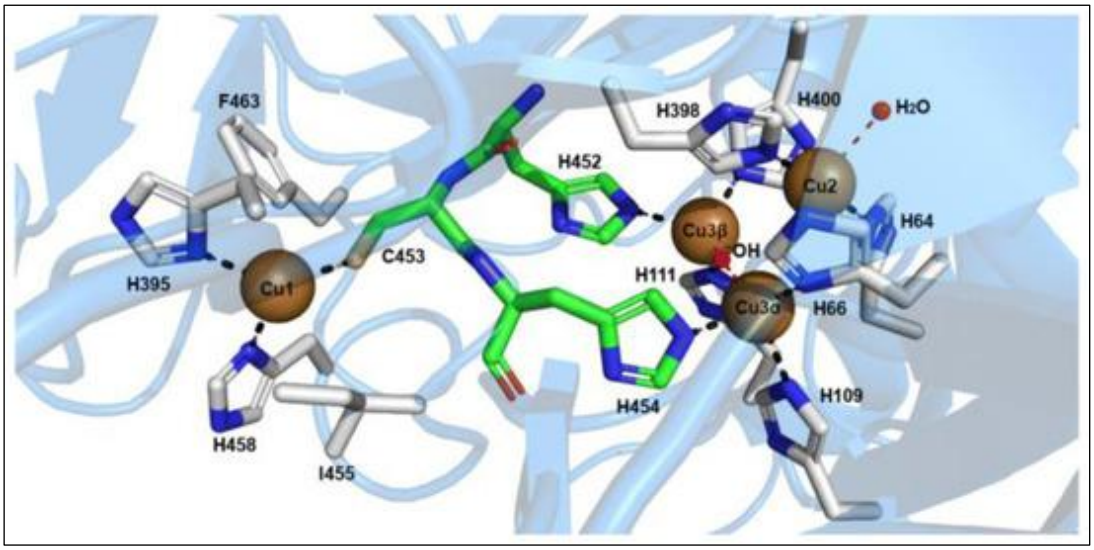

Figure 2. Representation of the laccase from *Trametes versicolor* structure. Reprinted from Ref. (Arregui, 2019).

Monomeric laccases typically have molecular weights ranging from 60 to 110 kDa, with glycosylation levels between 10% and 50%. Their thermostability, up to 70°C, is attributed to their high carbohydrate content (Yaropolov, 1994).

Fungal laccases are typically secreted extracellularly, although some fungi produce intracellular laccases with molecular weights ranging from 38 to 150 kDa (Manavalan, 2015). These enzymes generally contain three cupredoxin-like domains, each comprising around 500 amino acids. In contrast, bacterial laccases are primarily intracellular, with molecular weights between 50 and 70 kDa, and are predominantly found in the Bacillus and Streptomyces genera. More recently, smaller bacterial laccases, composed of only two domains and around 200 amino acids, have been identified. Certain fungi, such as *Pleurotus ostreatus*, also produce similar smaller laccases, consisting of just two domains (Komori, 2010). Although the amino acid sequences of fungal and bacterial laccases differ significantly, their molecular structure and the arrangement of their active sites are highly conserved (Chandra, 2015).

Laccases can be categorized based on the redox potential of the T1 site (low, medium, or high), which affects the efficiency of their catalytic function (Xu, 1996). Bacterial laccases typically exhibit low redox potentials (up to 460 mV), whereas laccases from Ascomycetes and Basidiomycetes fall into the medium range (460-710 mV). Laccases with high redox potentials (over 710 mV) are predominantly found in white rot fungi that degrade lignin (Loi, 2021).

The optical properties of laccases present valuable opportunities for developing various biotechnological applications, such as assays to evaluate their activity. Both laccases and phenol oxidation products have peculiar optical properties in the UV and visible light range of the spectrum, which can be utilized to develop absorbance or fluorescence-based methods for tracking their activity (Cantarella, 2003).

2. Optical techniques for sensing

The interaction of electromagnetic (EM) radiation (or of the corresponding photons) with matter underpins a wide range of optical sensing techniques used in environmental monitoring, analytical chemistry, and molecular spectroscopy. When EM radiation hits a material medium, several processes may occur depending on the energy of the radiation and the electronic, vibrational, and structural properties (Martin, 1973). The primary modes of interaction include absorption, fluorescence, and scattering, each providing a distinct set of observables that can be harnessed for qualitative and quantitative analysis. In the following, some of the techniques exploiting these interactions and of interest for the present thesis are briefly introduced, and some related experimental aspects are discussed.

2.1 UV-VIS Absorption and Fluorescence spectroscopy

2.1.1 Basic principles of UV-VIS Absorption and Fluorescence spectroscopy

Absorption occurs when the energy of incident photons matches the energy gap between molecular or atomic energy levels, resulting in the promotion of electrons from a lower to a higher energy state (Klotz, 1945). This process is highly dependent on the molecular structure and the electronic configuration of the absorbing species. It forms the basis of spectroscopic techniques, including UV-Vis absorption, which relies on the excitation of electrons within molecules in response to light in the ultraviolet (200–400 nm) and visible (400–700 nm) spectral regions. The resulting absorption spectrum—displayed as absorbance versus wavelength—reflects the electronic structure and chromophoric content of the molecule. The Beer-Lambert law, which expresses the linear relationship between the absorbance (A) and the concentration of an absorbing species (Hossain, 2022), is used for obtaining quantitative information from an absorption spectrum:

$$A = log(I_0/I) = \varepsilon \cdot d \cdot c \quad (2)$$

In this equation, A is the absorbance, ε is the molar absorption coefficient, d represents the thickness of the sample, and c is the concentration of the absorbent (Oshina, 2021; Guo, 2020). This law describes how the amount of absorbed light varies with the concentration and thickness of the sample (Figure 3) (Guo, 2020).

Solvent polarity, pH, and temperature of samples can shift or broaden absorption bands, impacting spectral interpretation.

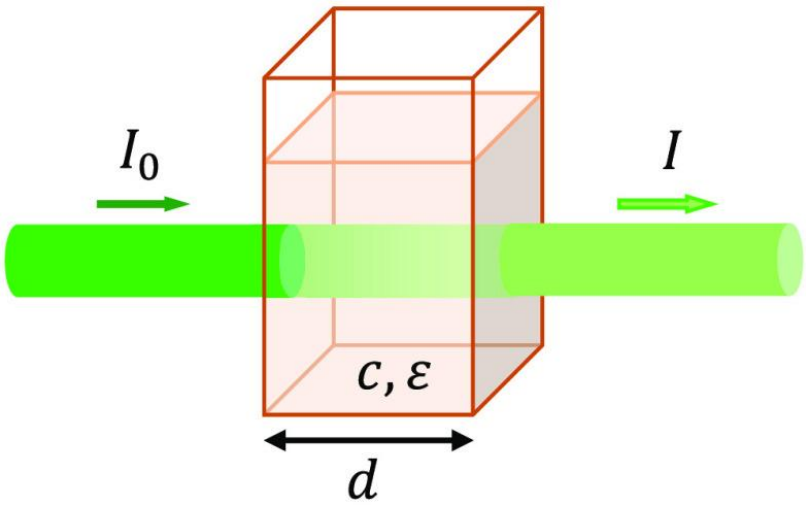

Figure 3. Description of Lambert-Beer law: (I) is the intensity of transmitted light, (I_0) is the intensity of incident light, (c) is the concentration of the absorbent, (d) is the thickness of the sample, and (ε) is the molar absorption coefficient. Reprinted from Ref. (Oshina, 2021).

Another phenomenon in the interaction between radiation and matter is emission (Weber, 1972; Lakowicz, 2006; Penner, 2017), which involves releasing energy by a molecule or atom that has previously absorbed radiation and transitioned to an excited state (Williams, 1964). As the system returns to a lower energy state, it emits a photon. Emission processes are often illustrated using the Jablonski diagram (Figure 4), which shows the various energy levels of the molecule involved in this interaction (Karoui, 2011; Momin, 2023; Zacharioudaki, 2022).

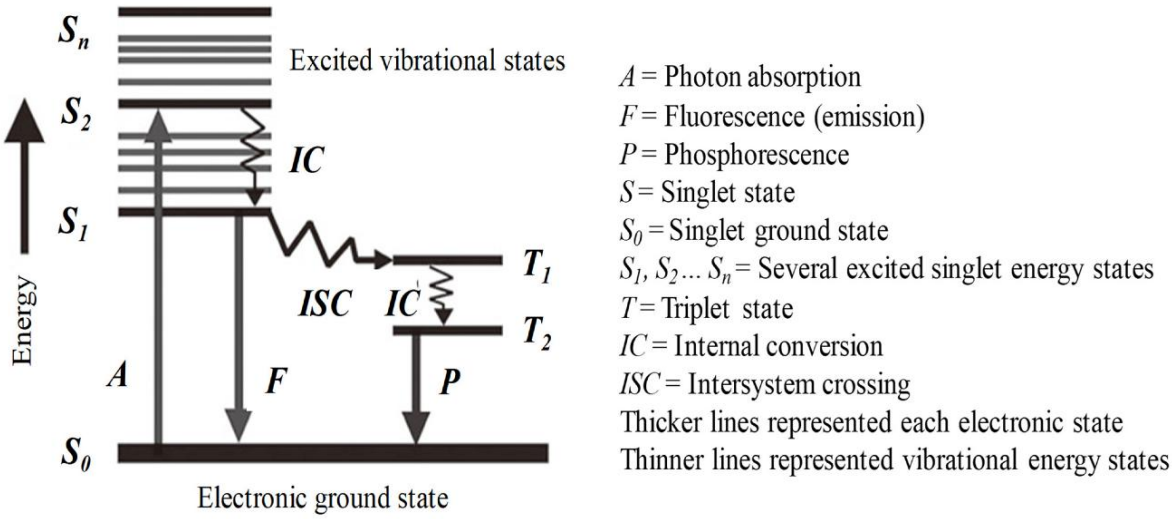

Figure 4. Representation of the Jablonski diagram showing the various energy levels of the molecule. Reprinted from Ref. (Momin, 2023).

When light is absorbed by a molecule, an electron in the molecule's ground state (S_0) is excited to a higher energy state (S_1 or S_2). As the electron relaxes back to its original state, it releases energy in the form of light, which has lower energy and a longer wavelength than the absorbed light. This difference in energy is called the Stokes shift and is due to non-radiative energy loss (Internal conversion (IC)) (Nijegorodov, 1997). The process of light emission that results from the electron's return to its lower energy state, which can occur in two forms: fluorescence (F) and phosphorescence (P). Fluorescence occurs when the electron transitions back from an excited singlet state to the ground state in a very short time frame (10^{-10} to 10^{-7} seconds). On the other hand, phosphorescence involves a transition from a singlet excited to a triplet state (T_1), which results in a slower emission process that can last from 10^{-6} seconds to several seconds (Intersystem crossing (ISC)) (Zhang, 2023; Momin, 2023; Zacharioudaki, 2022; Hachiya, 2009; Zhu, 2008; Marian, 2021; Karoui, 2018).
In environmental sensing, especially for compounds like phenols, both absorption and fluorescence methods are extensively utilized. Many phenolic compounds have characteristic UV absorbance due to their aromatic nature and can also exhibit intrinsic or induced fluorescence. This makes them ideal targets for optical sensors, which can be integrated into portable platforms for in situ monitoring of water quality.

2.1.2 Experimental aspects of UV-VIS absorption spectroscopy

An UV-Vis spectrophotometer is the usual device employed to obtain UV-Vis absorption spectra of samples, i.e., absorbance as a function of wavelength. UV-visible spectrophotometers have five main components: the light source, the monochromator, the sample holder, the detector, a data acquisition and analysis system.
The source consists of a lamp, emitting the most constant and reproducible radiation possible. For emission in the visible region, xenon lamps cover wavelengths in the 330-930 nm range. For emissions in the UV region, deuterium lamps are used (Patel, 2022; Shinde, 2020). The light beam from the lamp is directed towards a moving mirror and then reflected towards the monochromator. The monochromator partially separates the components of the radiation. There are two classes of spectrophotometers: single-beam and dual-beam, both schematically shown in Figure 5. A single-beam spectrometric instrument requires a reference sample to be measured separately from the sample under examination (Figure 5A). In a dual-beam spectrophotometer, the light from the source is split into two separate beams after passing through the monochromator (Figure 5B). One beam is used for

the sample, while the other is used for reference determination, so the sample and reference readings can be conducted simultaneously (Nilapwar, 2011).

Proper software is used to set the measurement parameters and acquire the spectra.

Some of the parameters to be defined before performing the acquisition are explained below:

- Scan speed refers to the speed at which wavelengths are scanned during spectral measurements. This has an impact on the time of acquisition of the signal at each wavelength to be analysed.
- The spectral bandwidth is defined as the wavelength width of the light at half the maximum intensity leaving the monochromator.
- The data pitch defines the number of data points collected during the scan. The data pitch and the spectral resolution are related.

Once the parameters have been entered, it is necessary to acquire the corresponding background (in the case of a single-beam spectrometer) or, in the case of a double-beam spectrometer, it is asked to insert the 'blank' (i.e., the reference sample) in the proper position.

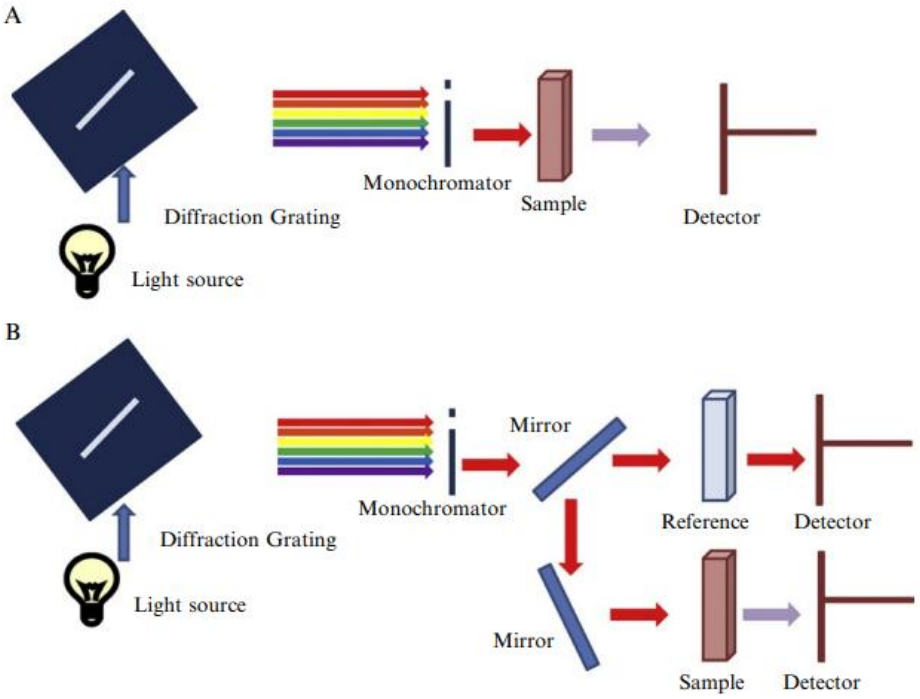

Figure 5. Block diagram of a spectrophotometer. Description of **A**) a single-beam spectrophotometer instrument, and **B**) a dual-beam spectrophotometer. Reprinted from Ref. (Nilapwar, 2011).

2.1.3 Experimental aspects of Fluorescence emission spectroscopy

A spectrofluorimeter is the device usually adopted for obtaining fluorescence spectra of a sample; a schematic diagram of a spectrofluorometer is shown in Figure 6. It consists of a light source produced by a lamp (in Fig.6, a Xenon lamp is shown) focused on the entrance to an excitation monochromator

that, through a diffraction grating, selects the desired wavelength (Gryczynski, 2019). The output monochromatic beam reaches the beam splitter, which divides the excitation beam into two parts: one for the sample (excitation beam) and one for the reference photomultiplier tube (reference beam). The excitation beam reaches the sample compartment and excites the sample. The light emitted by the sample is analysed by another monochromator and detected by the detector (Bag, 2024; Kumar, 2023; Raj, 2023). Hence, the instrument has two monochromators, the first positioned between the lamp and the sample to be measured, which selects the excitation wavelength, while the second monochromator is positioned between the sample and the detector, which selects the emission wavelength. The latter is placed at 90° to the direction of the incident beam to minimise the number of photons arriving directly at the detector from the source (Kumar, 2023). Some spectrofluorimeters are equipped with excitation and/or emission polarisers to polarise the incoming and/or outgoing light. The polarisers are usually removable and are only used for measurements requiring polarised light or for anisotropy measurements.

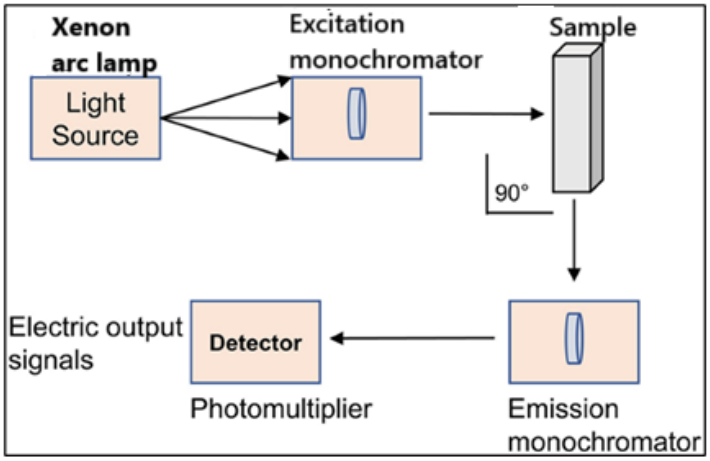

Figure 6. Schematic diagram of a spectrofluorometer with a light source, an excitation monochromator and an emission monochromator. The light emitted by the sample is finally detected by the detector. Reprinted from Ref. (Kumar, 2023).

Proper software is used to set the measurement parameters and acquire the spectra.

Some of the parameters to be defined before performing the acquisition are explained below:

- Excitation and emission slits are fundamental components that regulate the quantity and selectivity of the light that enters or exits the instrument. The excitation slit is located before the sample. Its main function is to regulate the light hitting the sample, both in terms of intensity and wavelength range. The narrower it is, the more precise the wavelength selection will be (better spectral resolution), but the less intense the light will be that reaches the sample. Emission slit is located after the sample, before the detector. It is used to select the wavelength of the fluorescent light emitted by the sample you want to measure. A narrower slit also gives

greater spectral resolution in the measurement, but less signal intensity. Both are therefore important because they act as selective steps to ensure that only the desired wavelength ranges are measured.

- Scan speed refers to the speed at which wavelengths are scanned during the measurements. This has an impact on the time of acquisition of the signal at each wavelength to be analysed.

2.2 Raman and SERS spectroscopy

2.2.1 Raman basic principles

Besides the absorption and emission processes, scattering can also occur when EM radiation interacts with matter. Scattering refers to the redirection of EM radiation, without a net transfer of energy to the absorbing species in elastic scattering (e.g., Rayleigh scattering), or with a partial transfer of energy in inelastic scattering (e.g., Raman and Brillouin scattering). Scattering techniques provide powerful complementary information to absorption and emission. These processes are especially useful in environments where direct absorption or emission measurements are challenging.

Raman spectroscopy is a technique based on the inelastic Raman light scattering, a phenomenon discovered in 1928 by Chandrasekhara Venkata Raman (Raman, 1928). When a monochromatic light impinges on a sample, it can be scattered at the same frequency as the incident light (this is Rayleigh scattering) or Raman Stokes or Raman anti-Stokes scattering can occur, in the case of lower or higher frequencies (Rostron, 2016; Fălămaș, 2020; Pasteris, 2020). Rayleigh scattering, which represents by far the largest contribution in the diffusive process due to its high probability, is therefore characterised by the absence of energy exchange between molecule and photon, and this reason is also called ‘elastic’ scattering. On the other hand, Stokes and anti-Stokes scattering are characterised by ‘inelastic’ scattering: the molecule respectively gives up or acquires vibrational energy for discrete quanta by interacting with the incident laser radiation (Figure 7) (Liu, 2022). It is precisely because of the inelastic phenomena of interaction that it is possible to obtain detailed information on the vibrational states of the material that scatters the radiation, resulting in true ‘fingerprints’ of the molecules. The Raman shift is defined by a molecule’s vibrational energy level, varying with the chemical group but independent of the excitation wavelength. The intensity of the Raman peak, shown as the vertical coordinate of the Raman spectrum, depends on factors like excitation light wavelength, power, concentration, molecular polarization, and the instrument's collection efficiency.

Therefore, Raman spectroscopy can effectively identify the properties and structures of different substances without requiring sample labelling, making it a versatile and non-invasive analytical tool.

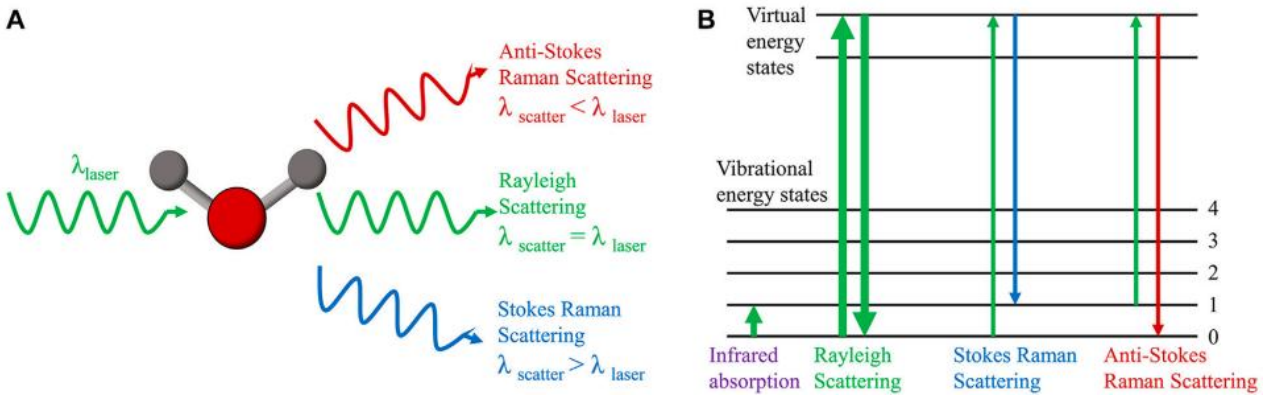

Figure 7. Principle of Raman scattering. (**A**) Comparison between Raman and Rayleigh scattering. (**B**) Representation of energy levels involved in Raman scattering, Rayleigh scattering, and infrared absorption. Reprinted from Ref (Liu, 2022).

The Raman signal is typically weak and, due to noise and fluorescence, may sometimes not be easily detectable. For this reason, it is not suitable for detecting molecules at low concentrations (Eskandari, 2022).

2.2.2 SERS and SERS substrates

To overcome Raman limitations, it is necessary to amplify the Raman signal. One of the most effective techniques to achieve this enhancement is Surface-Enhanced Raman Scattering (SERS). SERS is a detection technique in which the Raman signal by molecules hit by a laser beam is significantly enhanced when the molecules are adsorbed onto rough metallic surfaces, such as silver or gold nanoparticles (Langer, 2020). The discovery of the SERS effect occurred in 1974 by Fleischmann and colleagues during Raman measurements of pyridine on rough silver electrodes (Fleischmann,1974). They attributed the enhancement to a surface area effect. This phenomenon was independently identified by Jeanmaire and Van Duyne and by Albrecht and Creighton in 1977 (Jeanmaire, 1977; Albrecht, 1977), who suggested enhancement factors of 10^5 to 10^6. Albrecht and Creighton also proposed the connection to plasmonic excitation, a resonant Raman effect involving surface plasmon excitation, a concept introduced earlier by Philpott (Philpott, 1975). Later, Moskovits recognized the link between SERS intensities and the enhanced fields generated by surface-localised plasmons in nanostructured metals (Moskovits, 1978).

The intensity of the Raman signal is amplified via two main mechanisms: electromagnetic and chemical. A chemical effect occurs when the analyte's polarizability changes due to charge transfer

with the substrate (Kim, 2019). The electromagnetic effect, the dominant contributor, results from the excitation of localized surface plasmons (LSPs) on metal nanoparticles (NPs), creating intense electric fields, especially in "hot spots" (Ding, 2017). These regions, often formed at nanoparticle junctions or on irregular surfaces, can amplify Raman signals by up to 11 orders of magnitude.

Thanks to its ability to amplify the signal, the SERS technique has become one of the most powerful analytical tools for investigating molecules at low concentrations, even at single-molecule levels (Eskandari, 2022). It is widely applied in various scientific and technological fields, such as environmental monitoring (instrumental in detecting pollutants at low concentrations) (Rahmani, 2023), food safety (monitoring contaminants, pesticides and food quality, ensuring compliance with safety standards) (Shi, 2018), medical diagnostics, biomolecular analysis and, forensic science (Chen, 2020; Wu, 2020).

The performance of SERS heavily depends on the substrate used, as it governs the enhancement factor and the reproducibility of measurements. For this reason, over the years, significant progress has been made in developing various substrates. The simplest and most cost-effective are the colloidal metal (especially gold and silver) nanoparticles in solution. Well-assessed protocols are available in the literature (Turkevich, 1951; Frens, 1973), and it is well-known that, as the synthesis parameters change, it is possible to modulate the shape and size of the particles, thus shifting the plasmonic absorption peak (Mosier-Boss, 2017).

Several commercial SERS substrates have been introduced on the market, with different levels of performance and reproducibility. Among the first to commercialize SERS substrates, Real-Time Analyzers developed sol-gel-coated glass vials for Raman analysis. These vials were durable and used in applications like cocaine detection in saliva (Dana, 2015).

Sigma-Aldrich produces silica-coated gold nanoparticles and nanobars using tetraethyl orthosilicate (TEOS) to form mesoporous silica layers. These layers enhance chemical functionality, broadening the range of analytes detectable by SERS (Mosier-Boss, 2017).

Horiba offers lithographically fabricated gold nanorod substrates (http://www.horiba.com/us/en/scientific/products/raman-spectroscopy/accessories/sers-substrates/), while Ocean Optics provides flexible solutions, including handheld Raman devices with raster orbital scanning (ROS) capability and Ag/Au-based substrates (https://oceanoptics.com/product/sers/). AtoID creates disposable substrates by sputter-coating Ag or Au onto the plasmonic soda-lime glass (http://www.atoid.com/shop/). Silmeco specializes in silicon nanopillars coated with gold or silver, ensuring uniform enhancement over large surfaces (https://silmeco.com/products/).

The P-SERS substrates utilize inkjet-printed gold nanoclusters on cellulose paper, offering flexibility and ease of use. These substrates are particularly effective for detecting substances like pesticides and explosives (https://www.diagnosticansers.com/).

Premium substrates from SERSitive are individually fabricated by photolithography, enabling the creation of accurately defined shapes and dimensions for the active surface applied to the ITO glass. The glass surrounding the 4 mm x 5 mm active area makes these substrates comfortable to handle. These substrates consist of specially designed ITO glass coated with silver and gold nanoparticles https://sersitive.eu/about-substrates/.

Combining SERS with microfluidics, OndaVia produces cartridges for rapid chemical separation and detection. Their devices target analytes like arsenic, perchlorate, and nitrates, with detection limits reaching parts per billion (ppb) https://www.ondavia.com/about.

Lithographically prepared substrates, such as Mesophotonics' Klarite, feature arrays of pyramidal silicon wells coated with roughened gold, optimised for plasmon resonance http://www.mesophotonics.com/sers_central/index.html. These substrates allow reproducible measurements and have been used for applications such as ibuprofen quantification and melamine detection at ppb levels (Mosier-Boss, 2017).

Recent advancements have focused on creating large-area substrates with consistent topography to enhance uniform signals. For instance, substrates with 2D and 3D nanostructures have shown promise, and techniques like photoemission electron microscopy (PEEM) are being employed to map hot spot distributions for substrate optimization (Awada, 2012).

Thus, gold and silver are the most widely used metals for SERS measurements due to their optical properties. Both have plasmonic resonances in the VIS-NIR range, where the main wavelengths of the lasers used to fall, and the achievable resonance is, therefore, maximum.

The performances of the substrates must be tested for the specific molecule of interest since they can significantly vary.

2.2.3 Experimental aspects of Raman spectroscopy

A schematic representation of the experimental setup for Raman spectroscopy integrated with a microscope—commonly referred to as a Raman microspectroscopy system—is illustrated in Figure 8. This configuration highlights several key components: the excitation light source, a Rayleigh filtering system, a monochromator (represented schematically by mirrors and a diffraction grating), and a detector. Among these, the excitation source is particularly critical (Butler, 2016). Raman

spectroscopy relies on laser illumination, and the choice of laser has a profound impact on the quality and interpretability of the resulting spectra. The choice of laser wavelength is also crucial. Near-infrared (NIR) lasers (e.g., 785 nm or 1064 nm) are often preferred for biological or fluorescent samples because they minimize fluorescence background, thus improving the quality of the Raman spectra. However, longer wavelengths typically produce weaker Raman signals due to the inverse dependence of Raman scattering intensity on the fourth power of the wavelength. Conversely, ultraviolet (UV) lasers can yield stronger Raman signals and may help shift fluorescence emission away from the fingerprint region of the Raman spectrum, but they also carry a higher risk of sample photodegradation and often require more complex optical alignment. Thus, laser power, wavelength, and beam quality must be balanced according to the sample type and the experimental goals. Furthermore, the selected laser employed in a Raman system can affect other aspects of interest for different applications. Diode lasers have gained significant traction due to their compact size, durability, energy efficiency, and cost-effectiveness. These features make them suitable for portable or benchtop Raman systems. In contrast, gas lasers such as helium-neon (HeNe) and argon-ion lasers are bulkier and more expensive but still widely used, particularly where specific wavelength outputs or higher optical stability are required (Angel, 1995; Müller, 2013; Yan, 2007).

To separate the weak inelastically scattered Raman signal from the intense elastically scattered Rayleigh signal, an efficient filtering system is essential. Optical filters, such as notch filters and edge filters, are placed in the detection path to suppress Rayleigh scattering. Notch filters block a narrow band of wavelengths centred around the laser line, allowing both Stokes and anti-Stokes Raman signals to pass. In contrast, long-pass edge filters block only the laser wavelength and transmit Stokes-shifted signals. These filters typically use dielectric multilayer coatings, offering high optical density (OD >6) rejection of the laser line while maintaining excellent transmission in the Raman-shifted regions. Their role is vital in enhancing the signal-to-noise ratio and enabling the detection of subtle spectral features close to the excitation wavelength. The detector is another critical element in Raman microspectroscopy. Charge-coupled devices (CCDs) are the most used detectors due to their high quantum efficiency, low dark noise, and excellent spatial resolution (Cooper, 1994). CCDs capture photons and convert them into electrical signals, with pixel arrays that allow high-resolution spectral analysis (Matousek, 2010). Finally, microscope objectives are pivotal in determining both spatial resolution and light collection efficiency. Objectives with high numerical apertures (NA) improve signal collection and resolution, making them ideal for analyzing thin or microstructured samples. However, they often have shorter working distances. Lower-magnification objectives, with longer working distances, are better suited for bulkier or liquid samples, where precise spatial mapping is less critical (Butler, 2016).

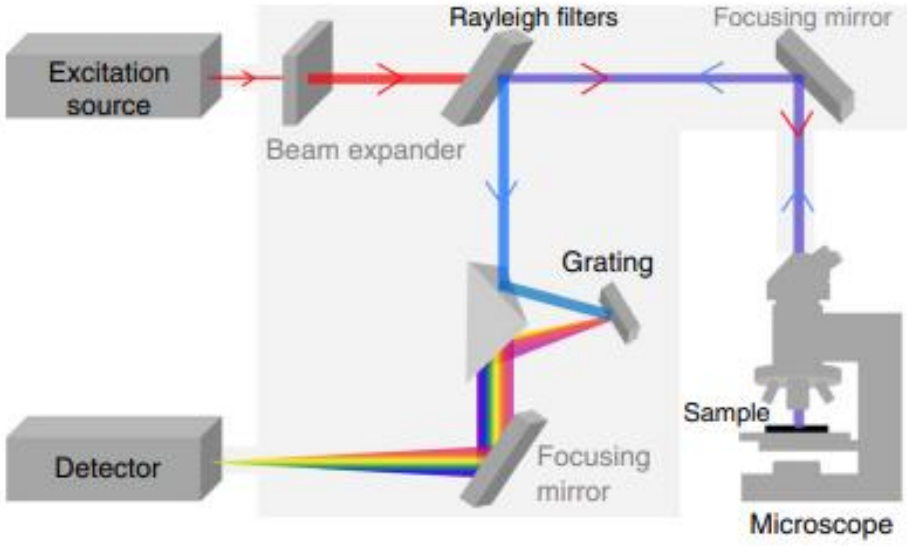

Figure 8. Representation of the components of a Raman spectrometer coupled with a microscope (Raman micro-spectrometer). Reprinted from Ref. (Butler, 2016).

Experimental parameters like exposure time, wavelength effects on resolution and sensitivity, and laser spot size are crucial in mitigating sample damage while optimizing data quality (Butler, 2016). Also, in the case of Raman systems, some parameters must be optimized before starting the measurements:

- Laser power (usually in milliwatts, mW) on the sample.
- Optical density (OD) of the attenuating filters inserted along the optical path of the laser beam.
- Accumulation is the number of times the signal is acquired and summed for the same point. The higher the number of accumulations, the greater the signal/noise ratio is, therefore making the spectrum "cleaner".
- Acquisition time indicates how long the detector records the Raman signal for each scan.
- Optical objectives.
- Density of grooves of the diffraction grating (in terms of lines/mm).

2.2.4 Data Analysis procedures

Pre-processing is a critical step in Raman spectroscopy data analysis. Following the correction of measurement artefacts during pre-treatment, pre-processing addresses sample-related issues and spectral contributions (Bocklitz, 2011; Ryabchykov, 2019). This involves baseline correction and noise reduction through smoothing and normalization.

Baseline correction is essential for removing the fluorescence background, which often overwhelms the weaker Raman signal. There are two main approaches (Ryabchykov, 2019):

- Subtracting a spectrum acquired with the shutter closed or from a region of the sample representing a blank (to account for the background signal).
- Using mathematical estimation methods to remove the baseline.

Smoothing techniques help reduce noise and enhance spectral interpretability. Popular methods include Savitzky-Golay smoothing (Savitzky, 1964), mean filtering, Gaussian filtering, and median filtering. Savitzky-Golay is particularly effective at preserving spectral peaks, while mean and Gaussian filters efficiently reduce noise. Median filtering is adept at removing outliers. However, all filtering methods risk losing useful spectral details. For large datasets, averaging spectra or applying dimension reduction can achieve smoother results without resorting to filtering.

Pre-processed spectra are then analysed to obtain information about single modes contributing to the spectra. At this aim, the position, height and width of the single peaks are obtained by peak fitting procedures, usually available in the software of the experimental apparatus.

3. Optical Methods for phenol detection in aqueous matrices

3.1 Biosensor designing based on optical methods

A biosensor is a device consisting of an immobilised biological component coupled to a physical component, or transducer. The former provides a specific response to specific analytes translated by the latter into an easily detectable signal (Figure 9) (Chen, 2020). Biological components include antigens, antibodies, enzymes, nucleic acids, receptors, cells and cell organelles (Chen, 2020). Various types of transducers can be used depending on the nature of the signal and the application:

- Electrochemical transducers: These use electrodes to convert chemical changes (such as redox reactions) into electrical signals.
- Optical transducers: These detect changes in light properties, such as absorbance, fluorescence, or refractive index, resulting from the biological interaction.
- Piezoelectric transducers: These measure changes in mass or force by detecting variations in the oscillation frequency of piezoelectric crystals.

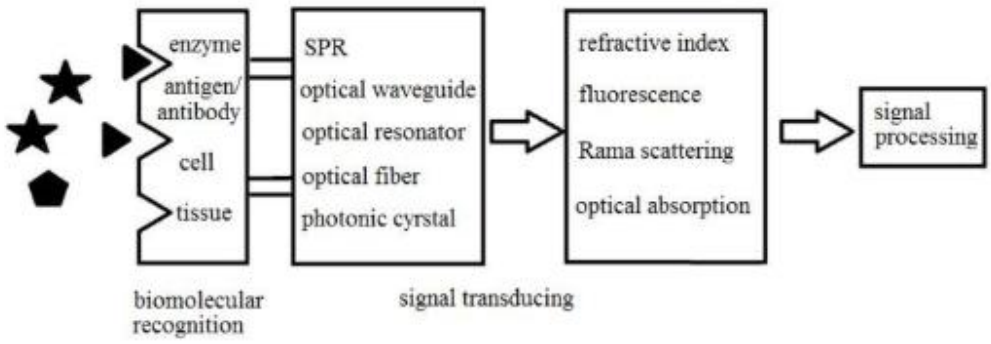

Figure 9. Graphical representation of an optical biosensor: biological components coupled to a transducer, which converts the resulting response into a detectable signal. Reprinted from Ref. (Chen, 2020).

In biosensors, enzymes with important optical properties, such as tyrosinase, peroxidase and laccase, are the most often used as biological elements.

Depending on the type of transducer used, biosensors are divided into piezoelectric, electrochemical and optical. In piezoelectric biosensors, the biological component, which can be an enzyme, an antibody or an antigen, is immobilised on the surface of a piezoelectric crystal. When the target molecule binds to the biological component, the total mass of the crystal increases and consequently, its resonance frequency changes. Biosensors of this type have been used to measure ammonia, nitrogen oxides, carbon monoxide, and methane. Electrochemical biosensors consist of a pair of

electrodes immersed in an electrolytic cell. The system detects the signal generated by bio-interaction, which involves the consumption or production of electrochemically active species (Naresh, 2021; Romero-Arcos, 2016).

Optical biosensors are based on the exploitation of EM radiation (typically in the UV-Vis-IR range) -matter interactions. In these systems, a beam of EM radiation is directed toward the sample containing the analyte. As the radiation interacts with the sample, it may be absorbed, emitted, scattered, or its properties (such as intensity, wavelength, or refractive index) may be changed. The radiation that emerges from this interaction is then collected and analyzed. The resulting signal is directly related to the amount of analyte present, allowing for sensitive and often real-time detection (Naresh, 2021).

The working parameters of sensors (and, thus, also of biosensors) are linear range, sensitivity and LOD (Limit of Detection). For biosensors required to detect analytes, the linear range is the analyte concentration range over which the biosensor provides a linearly varying response; the sensitivity comes from the calibration and it is related to the ability, while the LOD is the amount of analyte that needs to be added to have a signal variation equal to three times the standard deviation obtained when measuring the blank signal (Amine, 2006; Grieshaber, 2008).

Below are some classes of optical biosensors, focusing on those using laccase to detect phenolic compounds (as shown in Table 2).

3.1.1 Optical biosensor based on absorption spectroscopy

The most widely used approach in the design of optical biosensors for phenol detection using laccase is measuring changes in the absorption characteristics of the analyte. The first optical biosensor using this enzyme to detect catechol was developed in 2007 by Abdullah et al. (Abdullah, 2007). The design of the biosensor is based on the immobilisation of 3-methyl-2-benzothiazolinone hydrazone (MBTH) on nafion/sol-gel hybrid films and laccase on chitosan films for phenolic compounds detection (catechol, guaiacol, *o*-cresol and *m*-cresol).

The enzyme laccase catalyses the formation of quinone and/or phenoxy radical products from phenolic compounds. Figure 10 shows the absorption spectra of catechol oxidised by laccase in the presence and absence of the MBTH reagent. When immobilised MBTH is present, these radical products bind to form a stable azo dye compound, monitored with an absorption peak at 505 nm, as shown in Figure 10 (black line) (Abdullah, 2007).

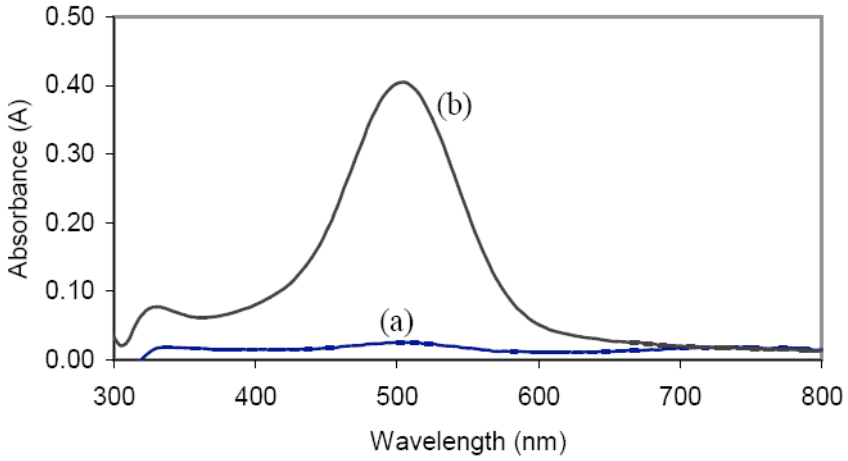

Figure 10. Absorption spectra of catechol oxidation (25 mM) with laccase (0.004 units/μL) in the absence (a) and presence (b) of MBTH (0.2 mM). Reprinted from Ref. (Abdullah, 2007).

The absorption spectra of the biosensor based on the immobilisation of MBTH on nafion/sol-gel hybrid films and laccase on chitosan films, in the presence and absence of catechol, are reported in Figure 11. According to Figure 10, an absorption peak is observed at 505 nm in the presence of catechol (Abdullah, 2007).

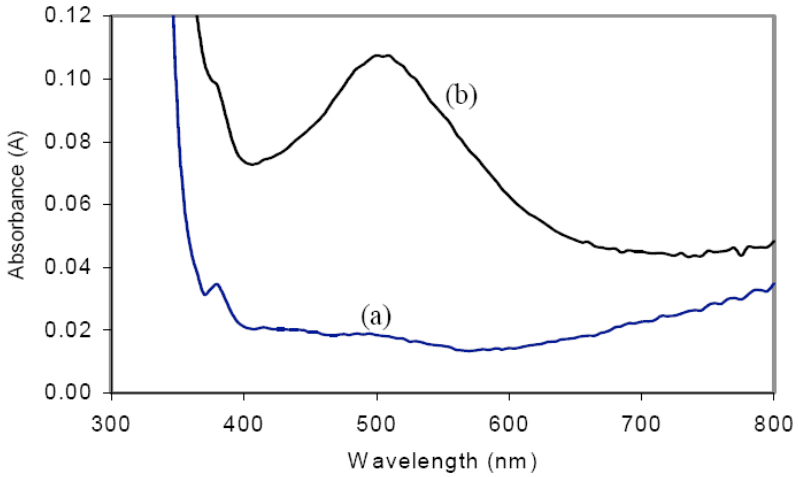

Figure 11. Absorption spectra of biosensor in the absence (a) and presence (b) of catechol (6.5 mM). Reprinted from Ref. (Abdullah, 2007).

The biosensor was studied using different phenolic compounds (catechol, guaiacol, *o*-cresol, and *m*-cresol) but only responded to catechol. The response curve of the biosensor toward increasing concentrations of catechol is shown in Figure 12, with a linear range for catechol of 0.5–8.0 mM and LOD of 0.33 mM.

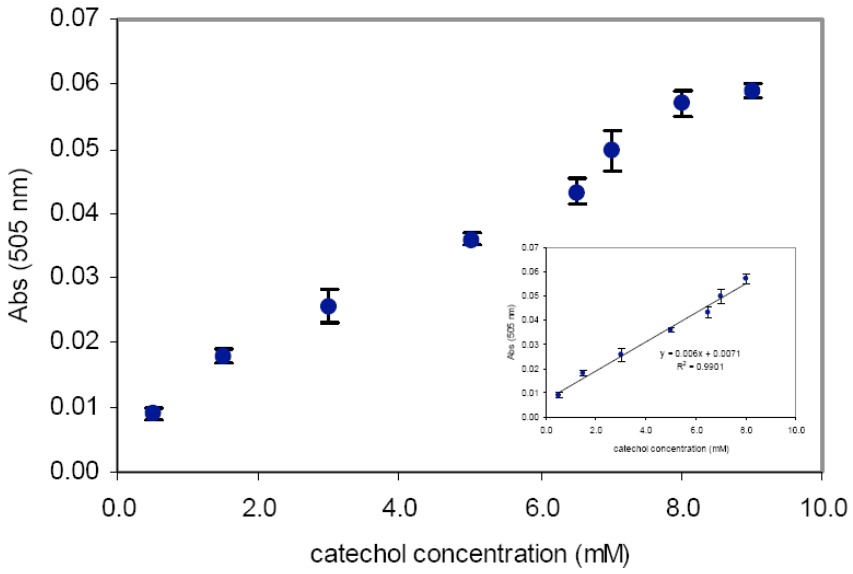

Figure 12. The response range of the biosensor to increasing catechol concentrations (0.5-8.0 mM). Reprinted from Ref. (Abdullah, 2007).

Lepore et al. (Lepore, 2017) studied the possibility of using laccase immobilised in sol-gel, an optically transparent matrix, for the development of biosensors for the detection of phenols in aqueous matrices. The choice of sol-gel allows the enzyme to be immobilised with good chemical stability, optical transparency and porosity (Portaccio, 2011; Simkus, 1996). Laccase and phenol reaction products exhibit significant optical characteristics in the UV and visible range, which are exploited for biosensing applications (Moshtaghioun, 2011). The authors preliminarily studied the absorption of laccase solution (from *Trametes versicolor*) in the presence of three phenolic compounds, such as (A) hydroquinone, (B) resorcinol and (C) catechol, as shown in Figures 13A-C. The visible signals at 425, 375 and 400 nm were used to determine the concentrations of hydroquinone, resorcinol and catechol, respectively. The calibration curves of the biosensors for increasing concentrations of resorcinol and catechol were presented (Figure 13D-E). The hydroquinone-laccase reaction has a slow response time, and therefore, the best results were obtained for resorcinol and catechol, with linear ranges up to 1.4 and 0.2 mM and LODs of 4.5 and 0.6 µM, respectively.

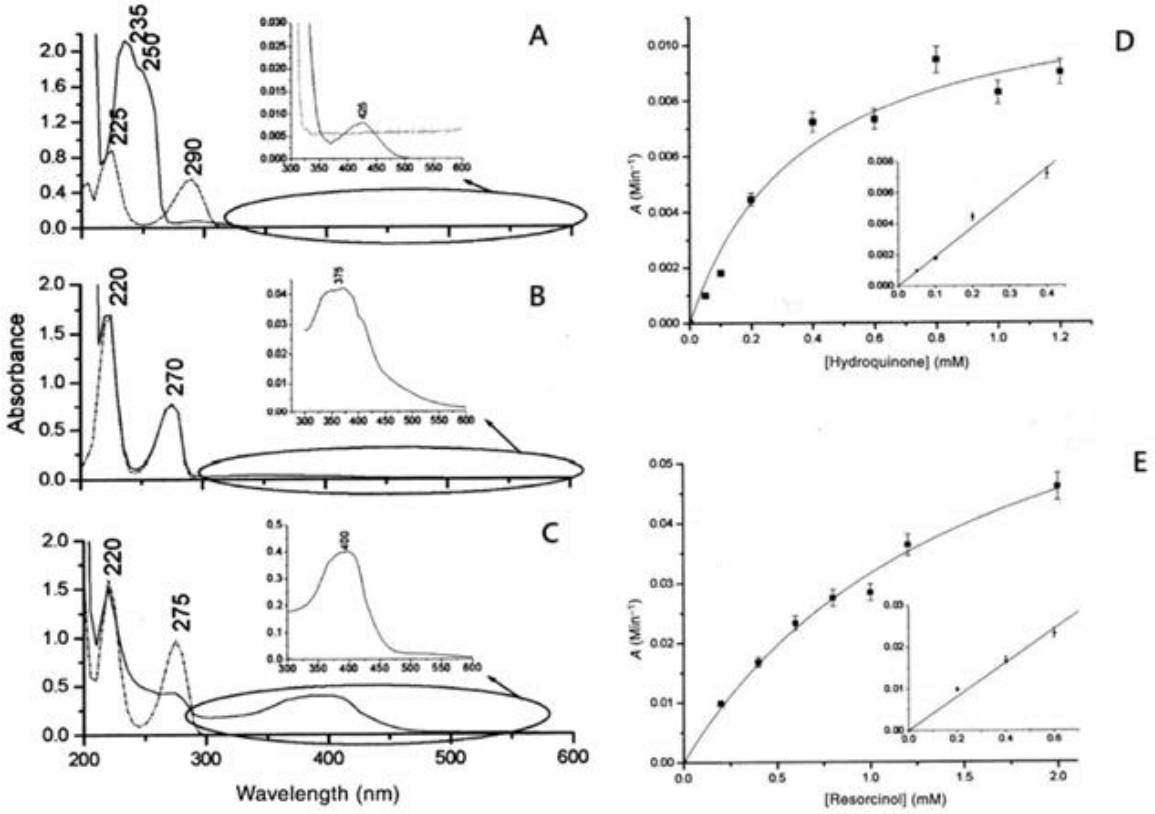

Figure 13. (**A**) Absorption spectra of hydroquinone and a solution of laccase and hydroquinone; (**B**) Absorption spectra of resorcinol and a solution of laccase and resorcinol; (**C**) Absorption spectra of catechol and a solution of laccase and catechol. The calibration curve of the optical biosensors based on sol-gel immobilized laccase at increasing concentrations of resorcinol (**D**) and catechol (**E**). Modified from Ref. (Lepore, 2017).

Cano-Raya et al. in 2020 (Cano-Raya, 2020) presented the first optical biosensor using PA6 microparticles for catechol detection, demonstrating its potential for environmental monitoring. The biosensor employs laccase from *Trametes versicolor*, immobilised on anionic polyamide 6 (PA6) porous microparticles. These particles are integrated into a Pebax MH1657 polymer binder containing MBTH, a chromogenic reagent selected for its ability to react with *o*-benzoquinone, a product of catechol oxidation, via oxidative coupling, forming a stable colored adduct, insoluble in water but soluble in organic solvents, with a maximum absorbance at 500 nm and a molar extinction coefficient of 32,500 $M^{-1}cm^{-1}$ (Figure 14).

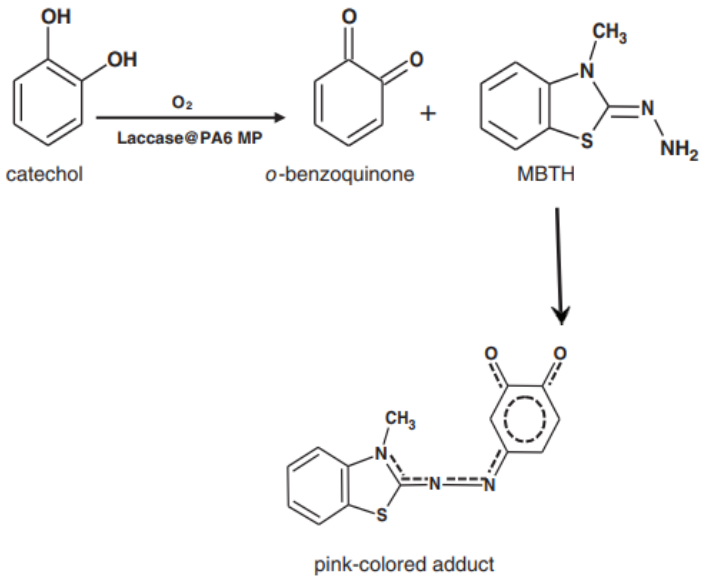

Figure 14. Chemical representation of a biosensor using PA6 microparticles for catechol detection. Reprinted from Ref. (Cano-Raya,2020).

Catechol quantification was based on the increase in absorbance ($\Delta A = A - A_0$), where A is the absorbance of the biosensor after reaction with catechol and A_0 is the initial absorbance after equilibration. The biosensor response was characterized by two sets of catechol concentration standards for a 30-minute reaction time. The first series included catechol concentrations ranging from 5×10^{-6} to 9×10^{-5} M in the maximum slope area (six standards with three replicates), and the second from 2×10^{-4} to 5×10^{-4} M in the minimum slope area (three standards with three replicates). Linearity was confirmed through a lack-of-fit test, establishing a linear calibration function in the maximum slope area (Figure 15 in inset).

The LOD was 11 μM, and the linear range was determined by the intersection point between the linear calibration and the linear function in the minimum slope area, giving a value of up to 118 μM (Figure 15).

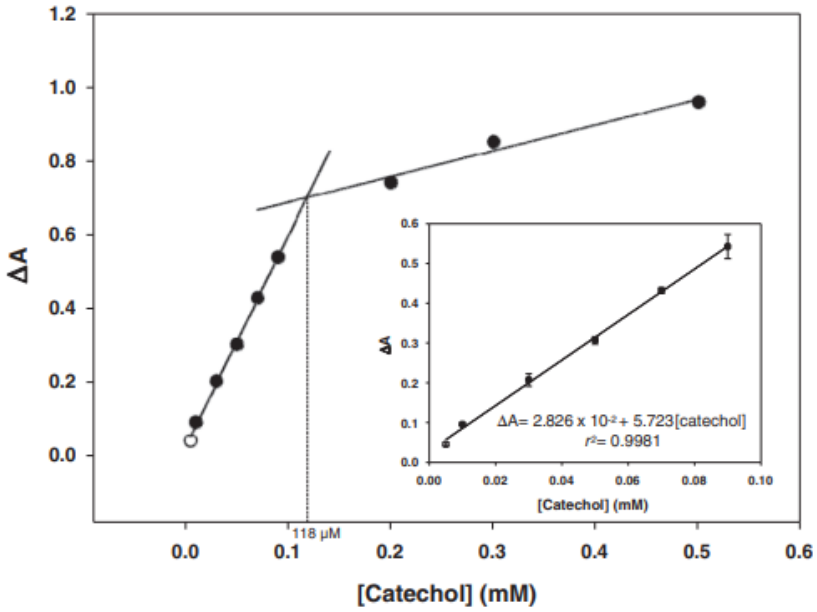

Figure 15. The calibration curve for different catechol concentrations. The linear calibration function in the maximum slope area is reported in the inset. Reprinted from Ref. (Cano-Raya, 2020).

3.1.2 Optical biosensors based on fluorescence spectroscopy

Andreu-Navarro et al. (Andreu-Navarro, 2012) present an enzymatic fluorimetric method for determining polyphenol compounds (including catechol, hydroquinone, hydroxyhydroquinone, and pyrogallol) in beverages based on the inhibition of the oxidation of indocyanine green (ICG), a long-wavelength fluorophor, in the presence of the enzyme laccase and positively charged gold nanoparticles (AuNPs). The method was optimized using gallic acid (GA) as a model. This approach employs a stopped flow mixing device to rapidly mix reactants, which include a solution of laccase, AuNPs, and Tris buffer and another containing the sample and ICG (Figure 16).

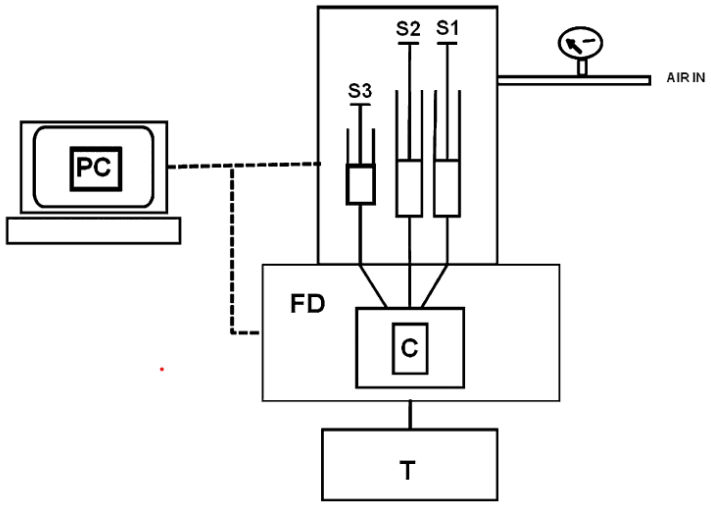

Figure 16. The schematic of the instrumental system includes several key components: S1 and S2 are the driving syringes, where S1 contains laccase and AuNPs, and S2 holds indocyanine green and the polyphenolic compound. S3 is the stopping syringe used to halt the flow. The system also features a spectrofluorometer (FD) for fluorescence measurement, an observation cell (C) for the reactions, a thermostat (T) to maintain optimal temperature, and a computer (PC) for data processing and control. Reprinted from Ref. (Andreu-Navarro, 2012).

The reaction mixture, containing laccase, AuNPs, and buffer, was combined with the sample or standard solution of IGC. The fluorescence signal of IGC was measured at 764 nm excitation and 806 nm emission. The time difference in fluorescence decrease between the presence and absence of polyphenols was used to determine gallic acid concentration based on a calibration graph, as shown in Figure 17. The system showed that polyphenolic compounds delayed IGC oxidation, with a time delay proportional to their concentration. The presence of positively charged AuNPs increased the induction time, likely due to their electrostatic interaction with laccase. With the following biosensor, they obtained different linear ranges and LOD for polyphenols: 0.08-5 μM and 0.01 μM for catechol, 0.13–5 μM and 0.04 μM for gallic acid, 0.05–2 μM and 0.01 μM for hydroquinone, 0.09–5 μM and 0.03 μM for hydroxyhydroquinone, then 0.17–5 μM and 0.04 μM for pyrogallol, respectively.

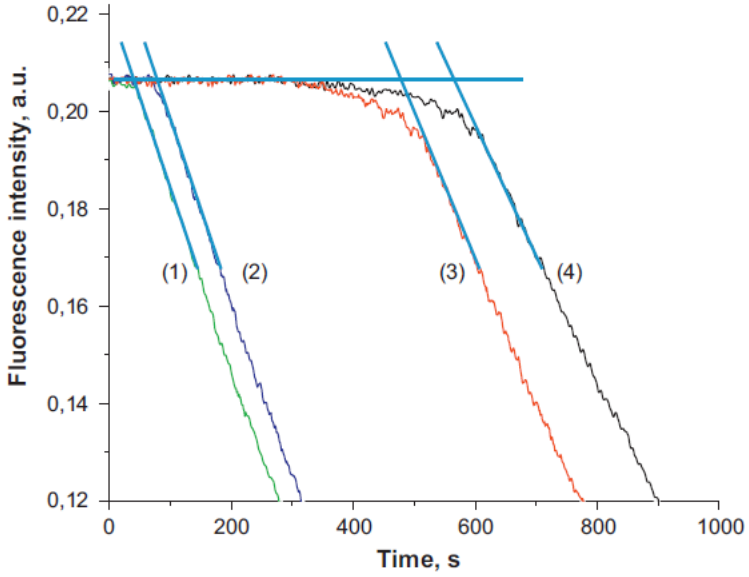

Figure 17. Kinetic curves were recorded for the laccase–indocyanine green system under different conditions: (1) with laccase and indocyanine green alone, (2) with laccase, indocyanine green, and AuNPs, (3) with laccase, indocyanine green, and gallic acid, and (4) with laccase, indocyanine green, AuNPs, and gallic acid. Reprinted from Ref. (Andreu-Navarro, 2012).

Bilir et al. (Bilir, 2016) have designed a fiber optic biosensor using laccase from *Pleurotus ostreatus* to detect polyphenolic compounds. The enzyme was immobilized on fiber optic oxygen sensor spots using 3-aminopropylsilanetriol, glutaraldehyde, and amino-modified carboxycellulose. A diffusion layer containing tetramethyl orthosilicate (TMOS), trimethoxymethylsilane (Tri-MOS), and polyvinyl alcohol (PVA) was added to enhance stability. The sensor monitored oxygen consumption due to laccase activity with catechol as a model substrate. The biosensor was based on luminescence emission from oxygen-sensitive dyes in sensor spots. When the dyes encountered oxygen, the energy was transferred through dynamic quenching, leading to a decrease in light emission intensity, as shown in Figure 18, describing the sensing mechanism.

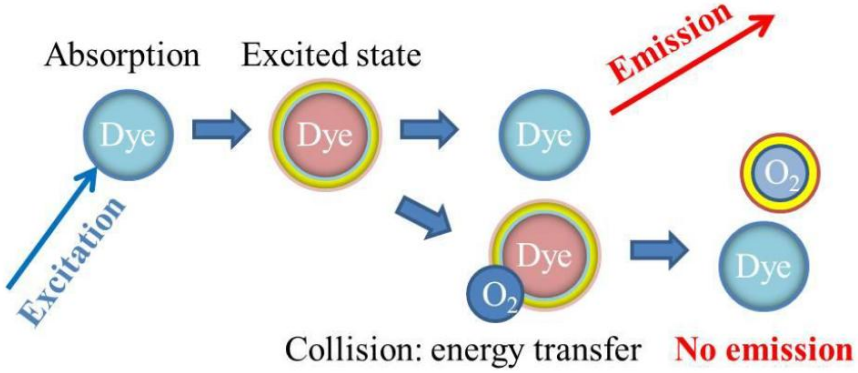

Figure 18. Detection method of the optical system based on oxygen sensing. Reprinted from Ref. (Bilir, 2016).

This system showed high reproducibility, stability and a response time of approximately 25 minutes. It demonstrated a linear range of 40–600 µM and a LOD of 0.04 mM for catechol (Figure 19).

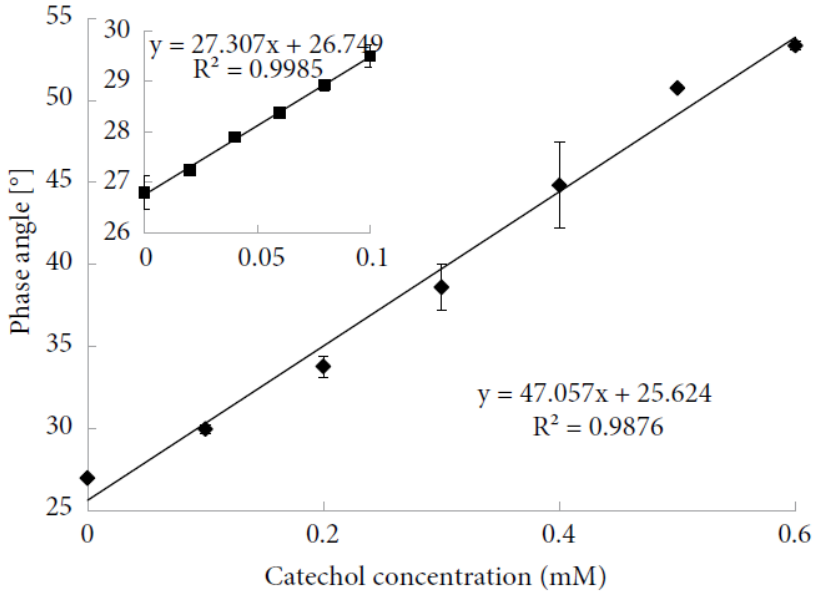

Figure 19. Calibration curve for an increasing catechol concentration. Reprinted from Ref. (Bilir, 2016).

3.1.3 Optical biosensors based on vibrational spectroscopy

Pan et al. in 2018 (Pan, 2018) presented a work aimed at studying Surface-Enhanced Raman Scattering (SERS) spectroscopy to determine PPO (polyphenol oxidase) activity in fruits and vegetables. PPO is an oxidoreductase enzyme responsible for the oxidation of phenolic compounds, producing quinones that lead to the browning of fruits and vegetables. To ensure the validity of the SERS method, the study examined the SERS activity of catechol in silver nanoparticle (AgNps) colloids. In the spectrum A reported in Figure 20, the Raman signal of catechol at a concentration of 10 mM is shown. Still, the characteristic bands of the substance are not visible, as the concentration is too low to be detected. When the catechol solution is combined with the colloidal AgNPs solution, the signal is detected, as it is amplified by several orders of magnitude (spectrum B in Figure 20). Specific vibrational bands, such as the 1258 cm^{-1} peak, assigned to the stretching vibrational mode of C-O, were identified as characteristic of catechol and used for quantitative analysis of PPO activity. Spectrum C shows the Raman signal of the catechol powder; spectrum D reports the Raman signal of the colloidal solution of AgNPs, with weak bands associated with the citrate used as a reagent in the synthesis process. Finally, spectra E and F show the SERS signal of the reaction medium comprising the catechol solution, PBS buffer (Na_2HPO_4-NaH_2PO_4) and PPO solution. A comparison

of spectra E and B in Figure 20 shows that both spectra follow a similar trend, but their SERS intensities differ. The addition of PBS and PPO solutions did not create new Raman peaks, and the slight difference in intensities may be due to variations in the fluorescence backgrounds of the two solutions. Spectrum F shows a reduced SERS signal after 5 minutes of enzymatic reaction, with the SERS intensity of the resulting solution weaker than the original, likely due to catechol degradation during enzymatic oxidation.

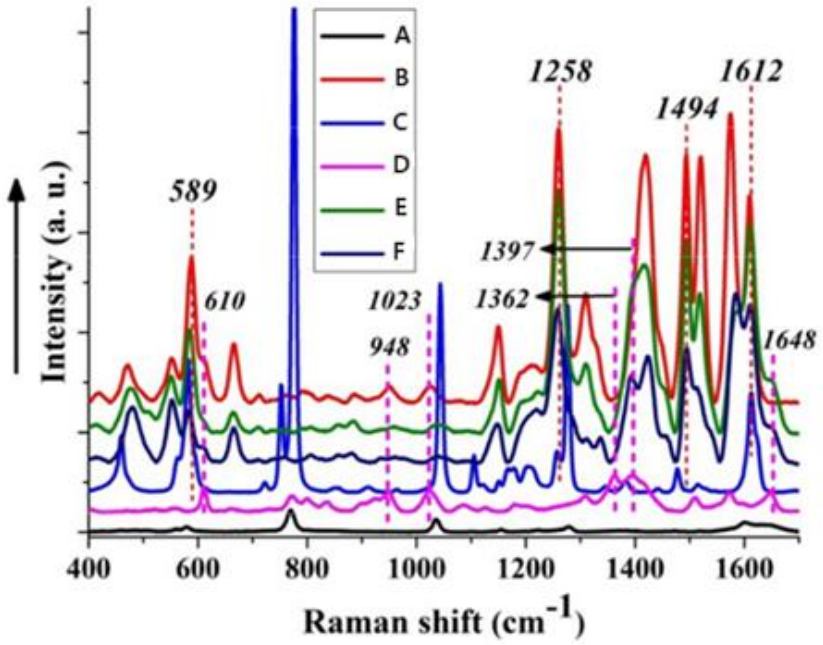

Figure 20. (**A**) Raman spectrum of catechol solution (at a concentration of 10 mM), (**B**) SERS spectrum of catechol solution (at a concentration of 10 mM) with AgNPs colloid; (**C**) Raman spectrum of catechol powder, (**D**) Raman spectrum of AgNPs colloid; then (**E**) and (**F**) SERS spectra of the reaction medium comprising the catechol solution, PBS and PPO solution. Figure modified from Ref. (Pan, 2018).

Next, the study investigated the effect of catechol concentration on SERS intensity. A concentration range from 0.1 mM to 11.0 mM was selected, and the results showed a linear increase in SERS intensity with catechol concentration (spectra A in Figure 21). Spectrum B presents the behaviour of the peak at 1258 cm^{-1} as a function of changing concentrations. The results showed that the optimal concentration range varies from 1 mM to 9 mM, and the relationship between SERS intensity and these concentrations is shown in spectrum C.

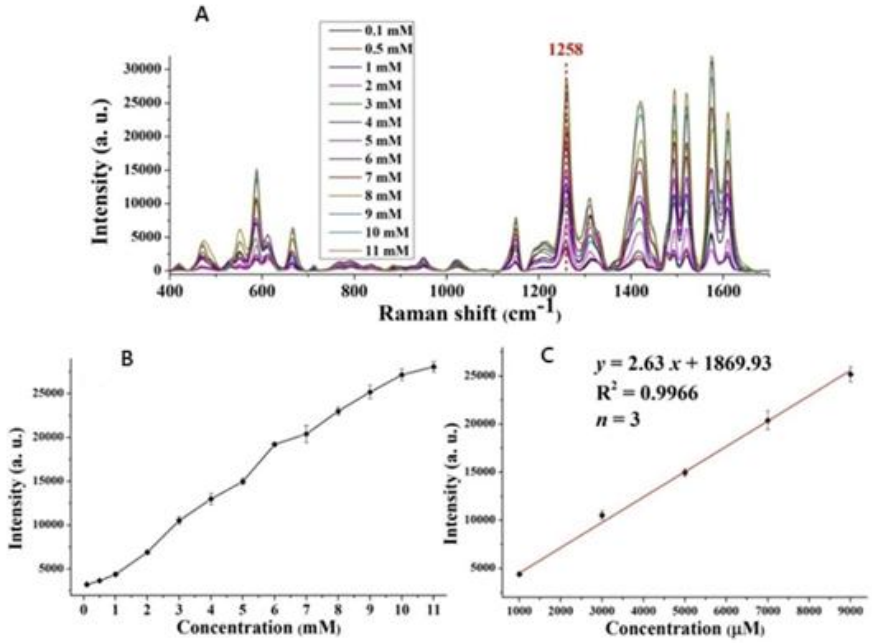

Figure 21. (**A**) SERS spectra of catechol at different concentrations (0.1-11 mM); (**B**) behavior of 1258 cm^{-1} peak as a function of increasing concentrations; and (**C**) the ratio between SERS intensity and concentration (from 1 mM to 9 mM range). Figure modified from Ref. (Pan, 2018).

Phenolic compound	Optical technique	Enzyme	Application	Sensitivity	Linear range	LOD	Response time	Ref.
Catechol	Absorption spectroscopy	Laccase from *Trametes versicolor*	E		0.5–8.0 mM	0.33 mM	10 min.	(Abdullah, 2007)
	Absorption spectroscopy	Laccase from *Trametes versicolor*	E		5-70 µM	2 µM		(Karami, 2019)
	Fluorescence Spectroscopy (Phase angle)	Laccase from *Pleorotus ostreatus*	D, E		40-600 µM	0.04 mM	25 min	(Bilir, 2016)
	Fluorescence spectroscopy	Laccase from *Trametes versicolor*	D		0.08-5 µM	0.01 µM		(Andreu-Navarro, 2012)
	Time course absorption spectroscopy	Laccase from *Trametes versicolor*	E	0.521 ± 0.016 Min^{-1} mM^{-1}	Up to 0.2 mM	0.6 µM	3 min	(Lepore, 2017)
	Absorption spectroscopy	Laccase from *Trametes versicolor*	E		Up to 118 µM	11 µM	30 min	(Cano-Raya, 2020)
	Absorption spectroscopy	Laccase from *Trametes versicolor*	E		9.79- 750 mM	0.109 mM		(Sanz, 2012)
	SERS spectroscopy	PPO (polyphenol oxidase)	D		1-9 mM	0.22 mM		(Pan, 2018)
Resorcinol	Absorption spectroscopy	Laccase from *Trametes versicolor*	E	0.075 ± 0.001 Min^{-1} mM^{-1}	Up to 1.4 mM	4.5 µM	3 min	(Lepore, 2017)
Hydroquinone	Fluorescence	Laccase from *Trametes versicolor*	D		0.05-2 µM	0.01 µM		(Andreu-Navarro, 2012)

Table 2. Examples of parameters of optical biosensors for phenolic compound determination (E and D indicate environmental and dietary applications, respectively).

3.2 Sensor designing based on optical methods

With the development of optical biosensors, particular attention in the literature has been focused on the design of optical sensors to monitor the concentration of phenolic compounds in environments. Optical sensors are among the most versatile sensing devices, capable of measuring various physical and chemical parameters such as temperature, pressure, force, electric and magnetic fields, pH, strain, chemical concentration, displacement, humidity, and many others (Delfino, 2021; Khairy, 2023). These optical technologies enable the development of new schemes and devices characterized by very low detection limits, high specificity and sensitivity (Lepore, 2022). In 2013, Rodionov et al. (Rodionov, 2013) presented an extensive description of various approaches for optical sensing, focusing mainly on spectrophotometric and fluorescent sensors that employ optical fibers for transmitting and detecting light signals. The authors detailed the sensors for measuring phenolic compounds in real samples, such as residential and industrial wastewater and river water. In addition, the development of nanotechnology and the use of vibrational spectroscopies (such as Raman and SERS spectroscopies) have opened new avenues for the design and development of advanced devices for detecting phenolic compounds (examples reported in Table 3) (Ganesan, 2020). These technological advances make it possible to improve the sensitivity and selectivity of optical sensors, expanding their applications in various sectors, including diagnostic medicine. In 2008, Nezhad et al. (Nezhad, 2008) introduced an indirect colorimetric method for the optical detection of phenolic compounds, exploiting the SPR (Surface Plasmon Resonance) band generated by gold nanoparticles (Nezhad, 2008). The authors demonstrated the ability to detect low concentrations of hydroquinone, catechol and pyrogallol through changes in the absorbance signal, which typically occur within seconds. This approach illustrates how the optical properties of gold nanoparticles can be exploited to develop highly sensitive and specific sensors for the detection of phenolic compounds, with potential applications in areas such as food safety and environmental monitoring.

3.2.1 Optical sensors based on absorption spectroscopy

Facure et al. in 2023 (Facure, 2023) present a work on the use of a composite material containing manganese dioxide (MnO_2) and graphene quantum dots (GQD), called MnO_2/GQD, which functions as a sensing platform for the colourimetric detection of phenolic compounds such as catechol (CC) and dopamine (DA), through colour changes of the analyte-containing solution. The enzymatic activity of the MnO_2/GQD composite was studied using a chromogenic reaction with 3,5,3′,5′ -

tetramethylbenzidine (TMB). In the presence of the nanozyme, the chromogenic substrate of TMB undergoes oxidation to form oxTMB, turning the initially colourless solution blue. With the addition of the phenolic compound, the oxTMB is again reduced to TMB, causing a loss of colour. The UV-visible spectra of the TMB solution, recorded after the addition of catechol or dopamine, revealed a linear relationship between the change in absorbance (ΔA) and the concentration of the analytes (Figure 22A and C). This reaction made it possible to monitor the presence of catechol and dopamine through colour changes. The calibration curve was created from the change in absorbance ($\Delta A = A_0 - A_5$), where A_0 and A_5 represent the absorbance at 652 nm at 0 and 5 minutes after adding the analytes, respectively (Figure 22B and D). A linear range from 10 µM to 50 µM was observed for dopamine, while a range from 4 µM to 40 µM was observed for catechol. LOD was 0.95 µM for dopamine and 0.37 µM for catechol.

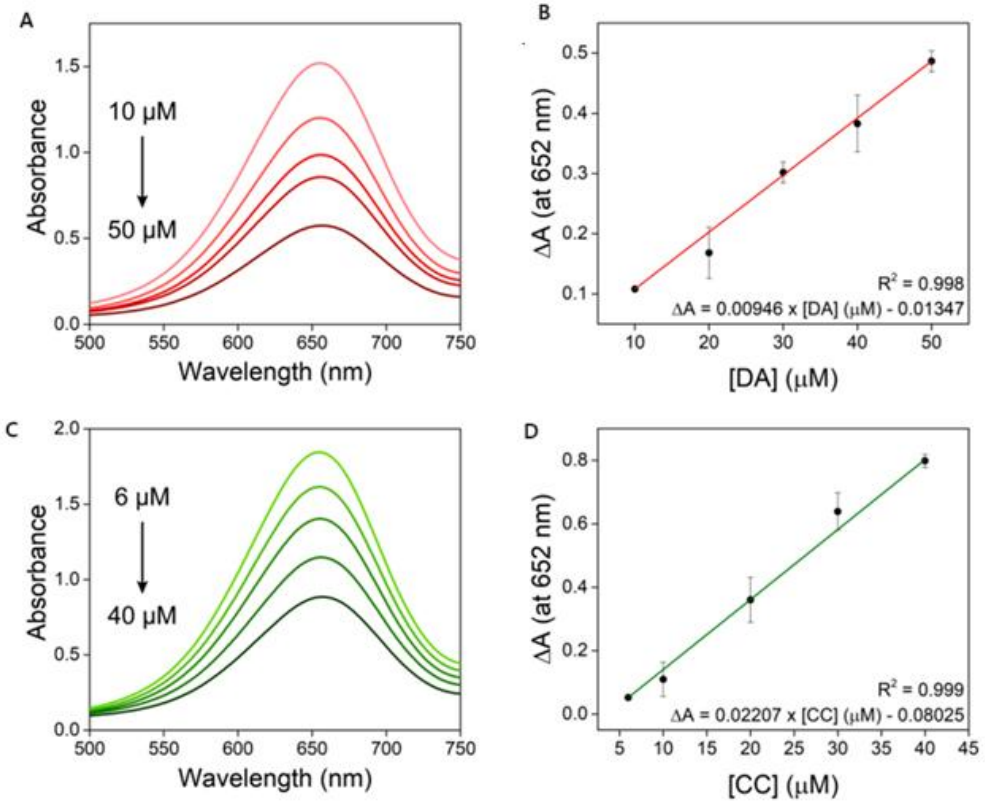

Figure 22. UV-vis spectra of TMB were measured 5 minutes after the addition of dopamine (**A**) and catechol (**C**) at different concentrations, and linear regression curves (**B** and **D**) showed the changes in absorbance (ΔA) at 652 nm. Figure modified from Ref. (Facure, 2023).

3.2.2 Optical sensors based on fluorescence spectroscopy

Xu et al. in 2022 (Xu, 2022) presented a study on the development of a fluorescent nanosensor based on Si QDs (silicon quantum dots), which incorporates an MIP (Molecularly Imprinted Polymer) and a silica coating (Si QD@SiO_2@MIP) for catechol (CT) detection. Among fluorescent nanomaterials, quantum dots (QD) are widely used for high-sensitivity detection (Hoan, 2019). A relevant technology to improve the selectivity of QD-based sensors is the Molecular Imprinted Technique (MIT) (Mehrzad-Samarin, 2017). MIPs produced by polymerising functional monomers with model molecules (target analytes) possess a specific shape and size for each analyte, improving the recognition capability of target analytes (Turiel, 2010). Integrating MIPs with QD allows for highly sensitive and selective sensors to detect analytes. Sensor efficiency was improved by optimising the excitation wavelength of the Si QDs to achieve better analytical performance (Zhou, 2017). The fluorescence emission spectra of Si QDs were measured at different excitation wavelengths (300-400 nm), and they exhibited the optimal emission peak when excited at 360 nm (Figure 23).

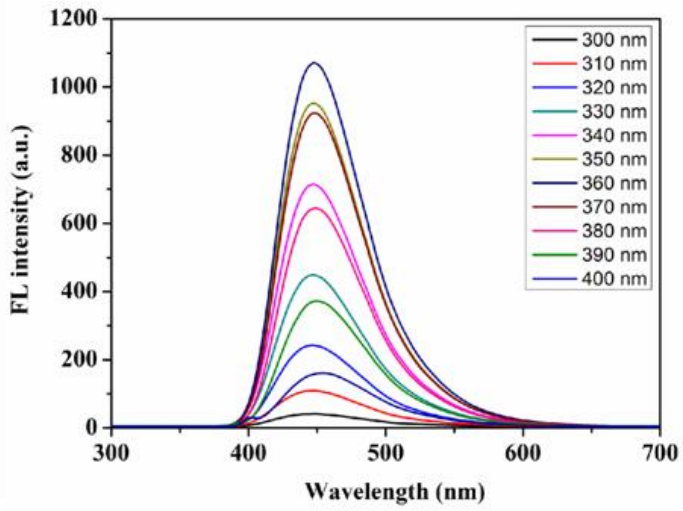

Figure 23. Emission spectra of Si QDs at different excitation wavelengths. Reprinted from Ref. (Xu, 2022).

Additionally, the optical characteristics of the prepared Si QDs were confirmed through fluorescence and UV–vis absorption spectra (Fig. 24). It was evident that the absorption peak at 331 nm corresponded to the n-π* transition (line c) (Yue, 2016). The fluorescence emission peak of the Si QDs appeared at 447 nm (line b) when excited at 360 nm (line a). Furthermore, under UV light, Si QDs emitted a blue fluorescence and showed a clear solution after exposure to sunlight (as seen in the inset of Figure 24).

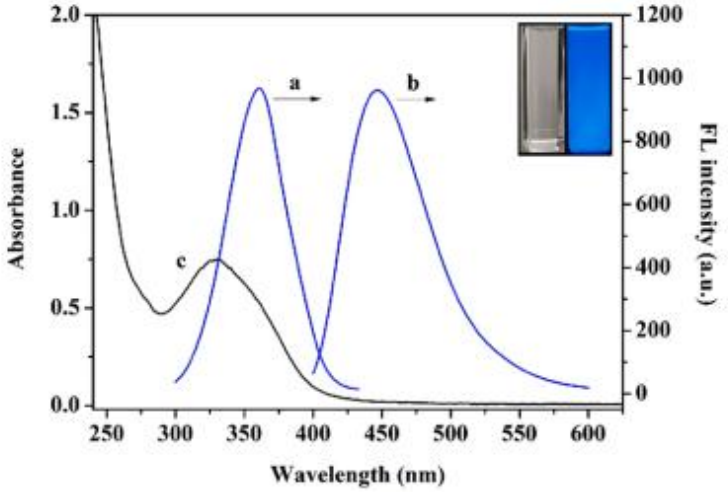

Figure 24. Fluorescence excitation spectrum (**a**), fluorescence emission spectrum (**b**), and UV–vis absorption spectrum of Si QDs (**c**). Reprinted from Ref. (Xu, 2022).

The fluorescence intensity ratio (I_0/I) remained stable over 21 tests conducted within 120 minutes (Figure 25A). In this context, I_0 and I corresponded to the fluorescence intensity of Si QDs@SiO_2@MIPs in the absence and presence of catechol, respectively. The impact of pH on Si QDs@SiO_2@MIPs was evaluated within a range from 3 to 11, both before and after 80 µM catechol exposure, as illustrated in Fig. 25B. The decrease in fluorescence intensity was observed at pH 7.0, so it was selected for this study. The effect of response time on the fluorescence intensity ratio (I_0/I) was examined at various time intervals following the addition of catechol at 80 µM (Figure 25C). It was observed that the fluorescence intensity of Si QDs@SiO_2@MIPs was quenched during the first 10 minutes (the time required for fluorescence quenching) after catechol addition.

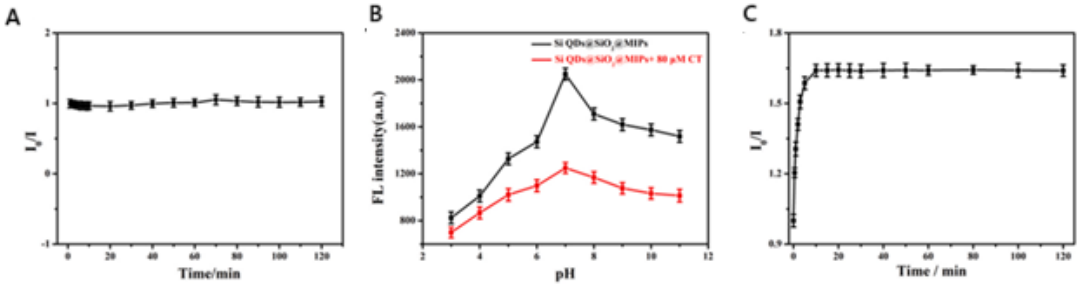

Figure 25. Fluorescence intensity of Si QDs@SiO_2@MIPs over 120 minutes (**A**); fluorescence intensity of Si QDs@SiO_2@MIPs (black line) and Si QDs@SiO_2@MIPs after catechol exposure (red line) (**B**); changes in the fluorescence intensity ratio (I_0/I) with catechol over 120 minutes (**C**). Figure modified from Ref. (Xu, 2022).

Subsequently, the analytical performance of Si QDs@SiO_2@MIPs was studied, with catechol concentrations ranging from 0 to 100 µM (Figure 26). The fluorescence intensity of Si QDs@SiO_2@MIPs decreased as the catechol concentration increased, as shown in Figure 26A. The

results showed a significant linear relationship between fluorescence intensity and catechol concentration, with a LOD of 0.018 µM, demonstrating the sensor's high sensitivity (Figure 26C). Furthermore, the fluorescence intensity of Si QD@SiO_2@MIP was compared to Si QD@SiO_2@NIP (an unimprinted sensor) to assess the effect of molecular imprinting (Figure 26B), following the addition of catechol concentrations from 0 to 100 µM. A linear correlation (Fig. 26D) was observed between relative fluorescence intensity (I_0/I) and catechol concentration. The results showed that the Si QD@SiO_2@MIP has a greater reduction in fluorescence intensity than the unimprinted sensor due to the formation of catechol binding sites during the molecular imprinting process.

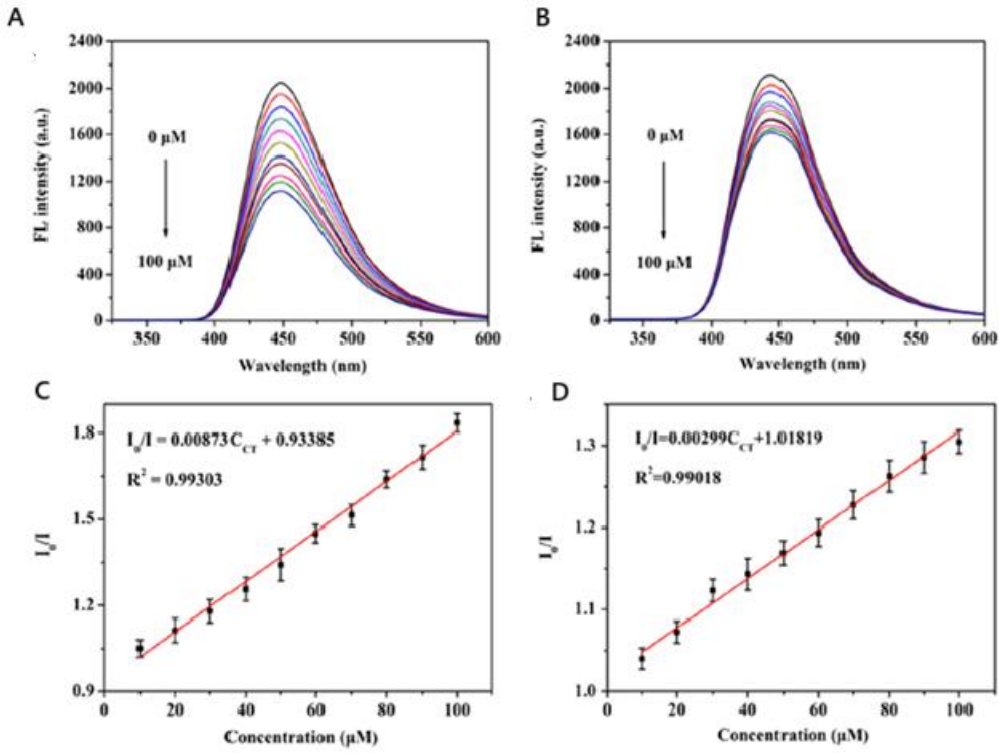

Figure 26. Fluorescence spectra of Si QDs@SiO_2@MIPs (**A**) and Si QDs@SiO_2@NIPs (**B**) with different catechol concentrations; linear regression curve (**C**, **D**). Figure modified from Ref. (Xu, 2022).

3.2.3 Optical sensors based on vibrational spectroscopy

Barveen et al. in 2022 (Barveen, 2022) proposed a novel approach by constructing hybrid nanostructures of noble metals (silver nanoparticles, AgNPs) and semiconductors (tungsten trioxide nanoflakes, WO_3NFs) for SERS applications.

The Ag-NP@WO_3-NF hybrid nanostructure not only exhibits high SERS efficiency for the detection of organic pollutants but also offers significant advantages in terms of reproducibility, uniformity and stability in SERS measurements, offering a cost-effective solution for real-world applications. In my

PhD project, it was complicated to replicate the construction of these hybrid nanostructures of noble metals and semiconductors, so we chose an approach that was easier to apply but still promising in terms of results, as explained in the following chapters.

Catechol, chosen as a model pollutant, serves as a probe molecule to evaluate the SERS performance of the Ag-NP@WO_3-NF nanostructures. Figure 27 shows the comparison between the Raman (10^{-2} M) and SERS (10^{-10} M) spectra of catechol. From the SERS spectrum, obtained using the Ag-NP@WO_3-NF nanostructure, a significantly higher signal intensity of the catechol can be observed compared to the Raman spectrum, with a blue or red shift of the Raman peak around ± 17 cm^{-1}.

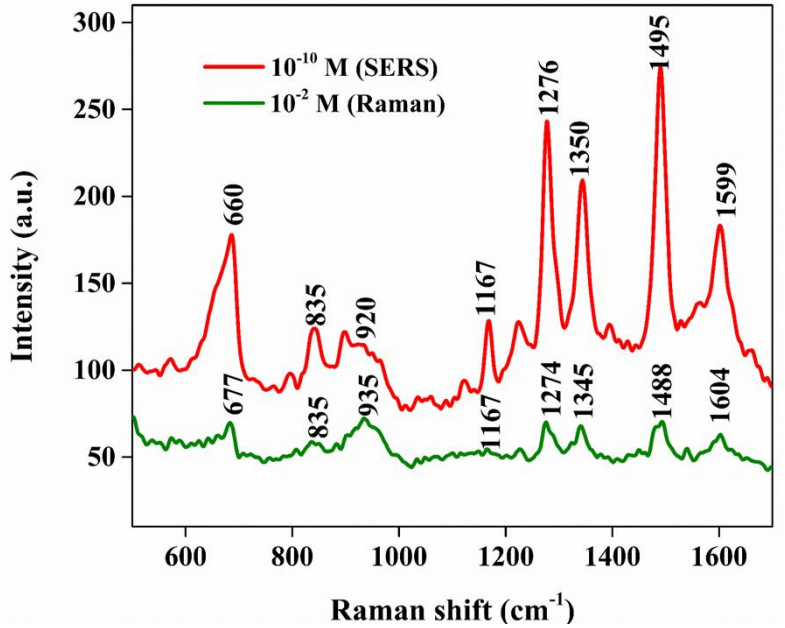

Figure 27. Raman spectrum (10^{-2} M, green line) and SERS spectrum (10^{-10} M, red line) of catechol solution. Reprinted from Ref. (Barveen, 2022).

Figure 28A shows SERS spectra with concentrations ranging from 10^{-1} M to 10^{-10} M, in which the characteristic bands of catechol are visible, and the intensity decreases with decreasing concentration. The most intense Raman peaks of catechol at 1495, 1276, and 1350 cm^{-1} were selected to represent the calibration plot, where a good linear relation is observed between the Raman peak intensity and the negative logarithmic concentration of catechol molecules in the studied concentration range (Figure 28B). LOD for catechol at the intense Raman peaks 1495, 1350, and 1276 cm^{-1} was 2.09×10^{-10} M, 3.62×10^{-10} M and 3.30×10^{-10} M, respectively (Barveen, 2022).

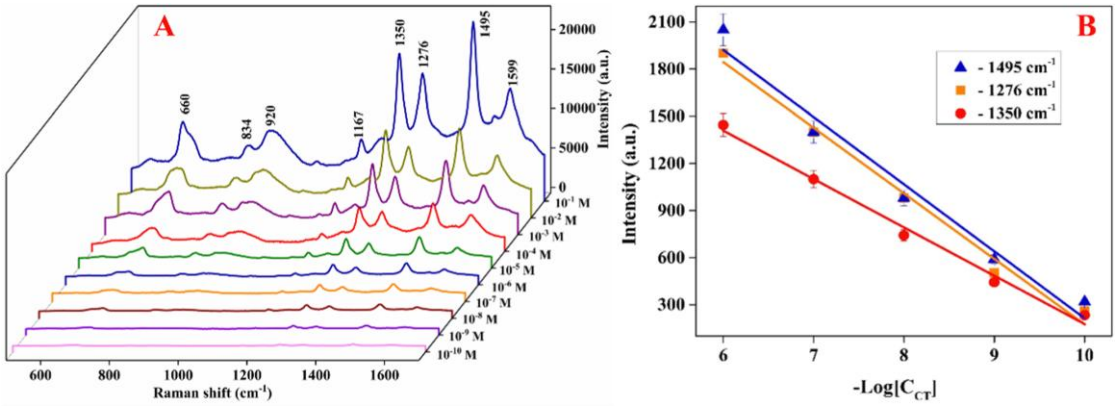

Figure 28. (**A**) SERS spectra with different catechol concentrations (from 10^{-1} M to 10^{-10} M), (**B**) calibration plot between three Raman peak intensities and the negative logarithmic concentration of catechol. Reprinted from Ref. (Barveen, 2022).

MXene, a novel 2D nanomaterial, has attracted significant attention due to its exceptional mechanical strength, thermal conductivity, hydrophilic surface, and adjustable band gap, making it widely applicable in areas such as energy storage, catalysis, electromagnetic shielding, and sensing. MXene's strong plasmon resonance effect in the visible and near-infrared range, particularly when combined with noble metal nanomaterials, enhances its surface-enhanced Raman spectroscopy (SERS) capabilities. This property makes MXene-based SERS substrates ideal for detecting environmental pollutants, including dye molecules, biomolecules, and pesticides.

Liu et al. in 2023 (Liu, 2023) proposed a work that investigated the development of MXene films supported on aluminum (Al) plates, which were then modified with Ag nanoparticles, forming Ag/MS-Al composites. These Ag/MS-Al composites displayed several promising characteristics, including uniformity, good signal repeatability, strong mechanical properties, and stability, making them suitable for large-scale production and use in flexible sensors.

The study systematically examined the SERS effect of Ag/MS-Al on catechol (CAT) molecules in water, demonstrating its sensitivity, high reproducibility, and stability. Raman peaks corresponding to catechol were observed when the phenol was adsorbed on Ag/MS-Al (Figure 29B). The SERS signals were much stronger than those obtained from bare Al plates or Ag-Al (Figure 29A), suggesting a strong chemical enhancement effect from the interaction between MXene and catechol molecules.

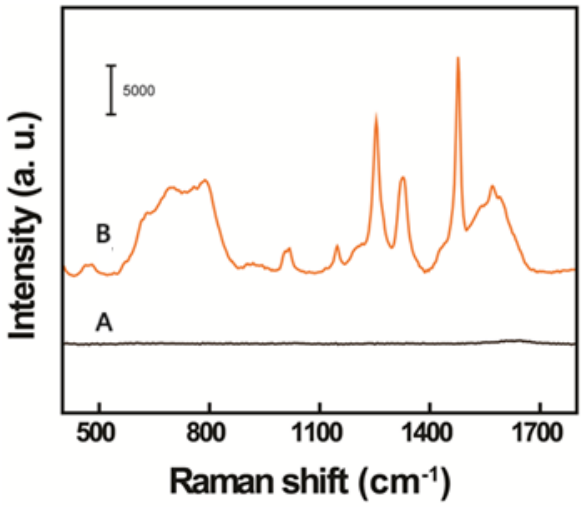

Figure 29. (**A**) Raman spectrum of water with Ag/MS-Al and (**B**) Raman spectrum of catechol (at 10^{-5} mol·L^{-1} concentration) with substrate. Figure modified from Ref. (Liu, 2023).

Additionally, the study found that even at low concentrations (5×10^{-8},1×10^{-7}, 5×10^{-7}, 1×10^{-6}, 5×10^{-6}, and 1×10^{-5} mol·L^{-1}), catechol could be detected using Ag/MS-Al as the SERS substrate (Fig. 30A).

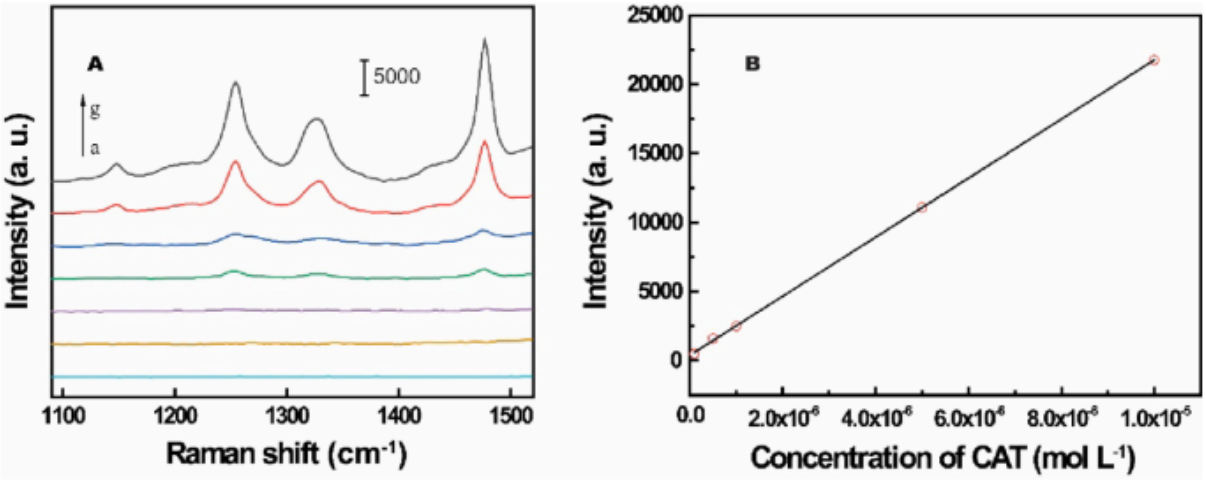

Figure 30. (**A**) Raman spectra of catechol at different concentrations with the presence of Ag/MS-Al: (a) 0, (b) 5×10^{-8}, (c) 1×10^{-7}, (d) 5×10^{-7}, (e) 1×10^{-6}, (f) 5×10^{-6}, (g) 1×10^{-5} mol·L^{-1}; (**B**) linear relationship between the SERS signal intensity at 1476.8 cm^{-1} and the catechol concentrations. Reprinted from Ref. (Liu, 2023).

The Ag/MS-Al composite exhibited a strong linear relationship between the SERS signal intensity at 1476.8 cm^{-1} (corresponding to C=C stretching vibration) and the catechol concentrations, indicating its potential for detecting phenol in water (Figure 30B).

Furthermore, when applied to seawater, Ag/MS-Al demonstrated similar sensitivity, and the Raman signal intensity of catechol was almost the same as in pure water, as shown in Figure 31A. A good

linear relationship between the SERS signal intensity at 1476.8 cm^{-1} and the catechol concentrations is shown in Figure 31B. The LOD was up to 5×10^{-8} $mol\cdot L^{-1}$ in water and $1x10^{-7}$ $mol\cdot L^{-1}$ in seawater.

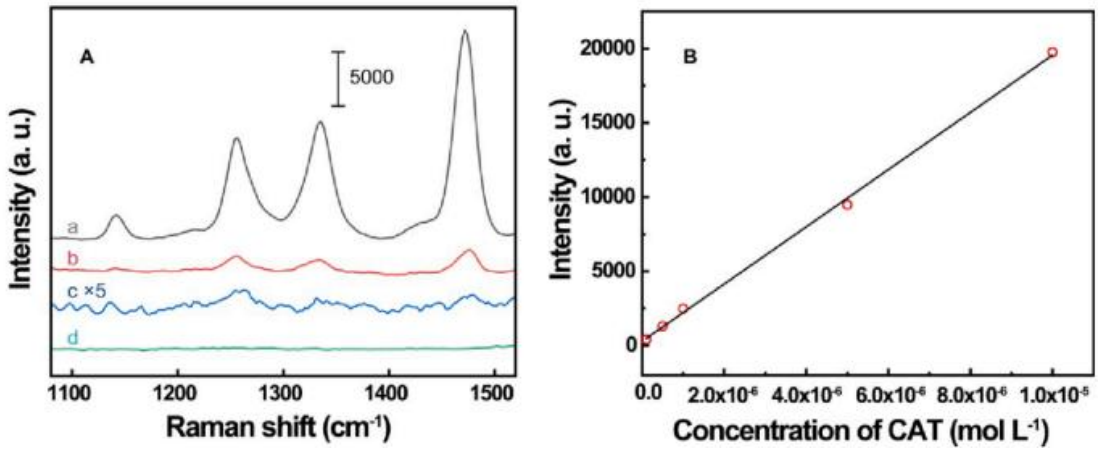

Figure 31. (**A**) Raman spectra of catechol at different concentrations with the presence of Ag/MS-Al in seawater: (a) 1×10^{-5}, (b) 1×10^{-6}, (c) 1×10^{-7}, (d) 0 $mol\cdot L^{-1}$; (**B**) linear relationship between the SERS signal intensity at 1476.8 cm^{-1} and the catechol concentrations. Reprinted from Ref. (Liu, 2023).

Overall, the study highlights the effectiveness of Ag/MS-Al composites as a sensitive, stable, and reproducible SERS platform for detecting trace levels of catechol in both pure water and seawater, offering a promising approach for environmental monitoring.

Phenolic compound	**Optical technique**	**Linear range**	**LOD**	**Ref.**
Catechol	Absorption spectroscopy	4-40 µM	0.37 µM	(Facure, 2023)
	Fluorescence spectroscopy	0.018-100 µM	0.018 µM	(Xu, 2022)
	SERS spectroscopy	0.0001-1x10^5 µM	0.000209 µM	(Barveen, 2022)
	SERS spectroscopy	0.05-10 µM (in water) 0.1-10 µM (in seawater)	Up to 0.05 µM (in water) Up to 0.1 µM (in seawater)	(Liu, 2023)

Table 3. Examples of parameters of optical sensors for catechol detection.

4. Experimental methods for investigating phenol-membrane interactions

4.1 Membrane models

Biological membranes play an essential role in cellular organization by serving as barriers that compartmentalize the cytoplasm into organelles and regulate material exchange between cells and their environment. The "fluid mosaic" model proposed by Singer and Nicolson in 1972 describes membranes as viscous phospholipid bilayers embedded with proteins that can freely diffuse, a concept later refined with the discovery of large membrane domains and microstructures such as lipid rafts and caveolae (Singer, 1972). Membrane lipids can be categorized into three groups based on their chemical structure: glycerol-based lipids (phospholipids), ceramide-based sphingolipids, and cholesterol. Phospholipids, such as phosphatidylcholine (PC), phosphatidylethanolamine (PE), and phosphatidylserine, are the primary lipids in cellular membranes, while phosphatidylinositol and cardiolipin are present in smaller amounts. Sphingolipids, with a sphingoid backbone, increase the hydrophobicity of the bilayer. Cholesterol has a hydroxyl group that interacts with the hydrophilic head groups of phospholipids and a bulky steroid group that interacts with the hydrophobic acyl chains, influencing membrane fluidity and packing (Peetla, 2009; Escriba, 2008). It is well known that membrane constituents are not homogeneously distributed within the bilayer but are organized into complex lateral microdomains (Figure 32i). This polymorphism, along with the wide variety of lipids with distinct physical properties (such as cross-sectional area, fluidity, charge, and molecular weight), makes lipid membranes highly intricate. The covalent attachment of proteins and carbohydrates further adds to the complexity. To overcome this, simplified artificial membrane models that mimic natural lipid bilayers have been developed to study lipid-protein interactions. These models help uncover the physical principles underlying membrane phase behavior and lipid-protein interactions. Biomimetic systems, such as lipid monolayers, lipid vesicles, and supported lipid bilayers (SLBs), are commonly used to explore these interactions (Figure 32ii) (Peetla, 2009).

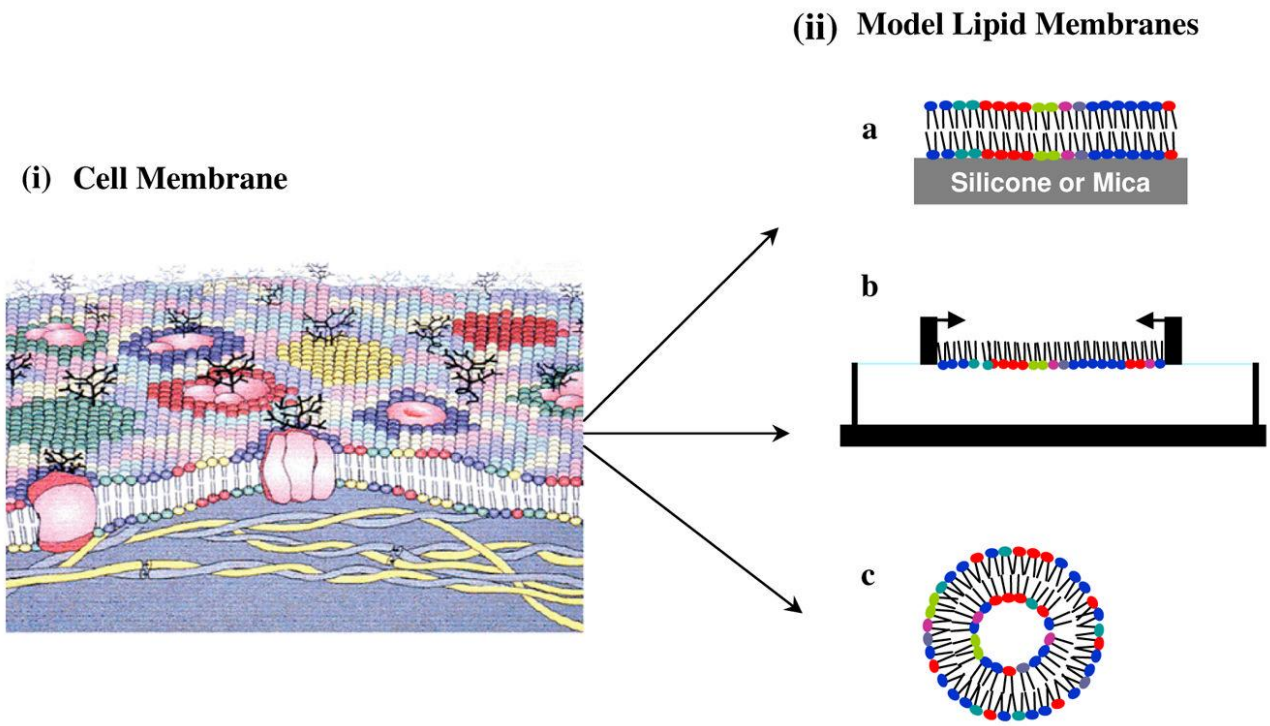

Figure 32. Representation of the cell membrane (i) and membrane models (ii). **a**) lipid bilayers, **b**) lipid monolayers and **c**) lipid vesicles. Reprinted from Ref. (Peetla, 2009).

4.1.1 Lipid Monolayer Models

The study of lipid monolayers dates to the 18th century, beginning with Benjamin Franklin's experiments. The field progressed in the 19th century with contributions from scientists like Rayleigh and Gibbs, leading to important advancements in understanding lipid behavior (Rojewska, 2021). In the 20th century, Irving Langmuir developed methods to control the formation of lipid monolayers and study their thermodynamics. His work played a pivotal role in understanding how lipids form monomolecular films at the liquid/air interface, simulating the leaflets of biological membranes. For example, a mixture of phosphatidylcholine (PC), sphingomyelin (SM), and cholesterol (CHOL) can represent the outer leaflet of a membrane, while phosphatidylserine (PS), an anionic lipid, can simulate the inner leaflet (Rojewska, 2021). The Langmuir technique allows precise control over the monolayer's composition, molecular packing, and physical states, making it an essential tool for studying membrane dynamics. This feature allows researchers to study the energetics of lipid interactions using surface tension measurements. The Langmuir technique also enables the formation of lipid films on the water subphase, allowing the characterization of lipid-lipid, lipid-water, or lipid-drug interactions based on compression isotherms. These isotherms measure surface pressure as a function of the mean molecular area ($Å^2$), with two automated barriers moving along the subphase surface to compress the film at the correct rate. As the monolayer is compressed, surface pressure (π)

is continuously measured while the mean molecular area (A^2) decreases. This compression forces the molecules to reorganize at the interface, resulting in changes to the physical states of the monolayer (Figure 33). These physical states depend on the level of molecular conformational order, indicated by intermolecular interactions within the monolayer (Rojewska, 2021). As surface pressure increases, the monolayer density also increases until the collapse point ($\pi_{collapse}$) is reached, beyond which pressure cannot be further increased. Analysing the $\pi_{collapse}$ values helps determine the stability and miscibility of components in a mixed monolayer (Elderdfi, 2018). The course of the π-A isotherm provides valuable information about molecular interactions at the interface. The phase behavior of the monolayer is primarily determined by the physicochemical properties of the lipid amphiphile, as well as the subphase temperature and composition. Two common monolayer states are the liquid-expanded (LE) and liquid-condensed (LC) states, which are like the liquid-crystalline and gel states in bilayers, respectively (Kaganer, 1999). A lipid monolayer is also characterized by changes in two-dimensional compressibility (C_s), typically expressed as the surface compressional modulus (C_s^{-1}) (Davies, 1961). This parameter is sensitive to small changes in the monolayer's structure during lateral interactions, providing insights into the lateral packing elasticity of the system. A higher compressibility modulus indicates increased rigidity (or decreased compressibility) in the monolayer. Additionally, combining the Langmuir technique with advanced imaging tools, such as a Brewster angle microscope, fluorescence microscope, or atomic force microscope (AFM)—enables high-resolution, real-time visualisation of the monolayer's morphology and molecular organisation during compression, providing insights into phase transitions, domain formation, and structural heterogeneity. This combination of methods offers a comprehensive understanding of lipid monolayer behavior and provides a valuable framework for studying lipid interactions and their role in biological systems.

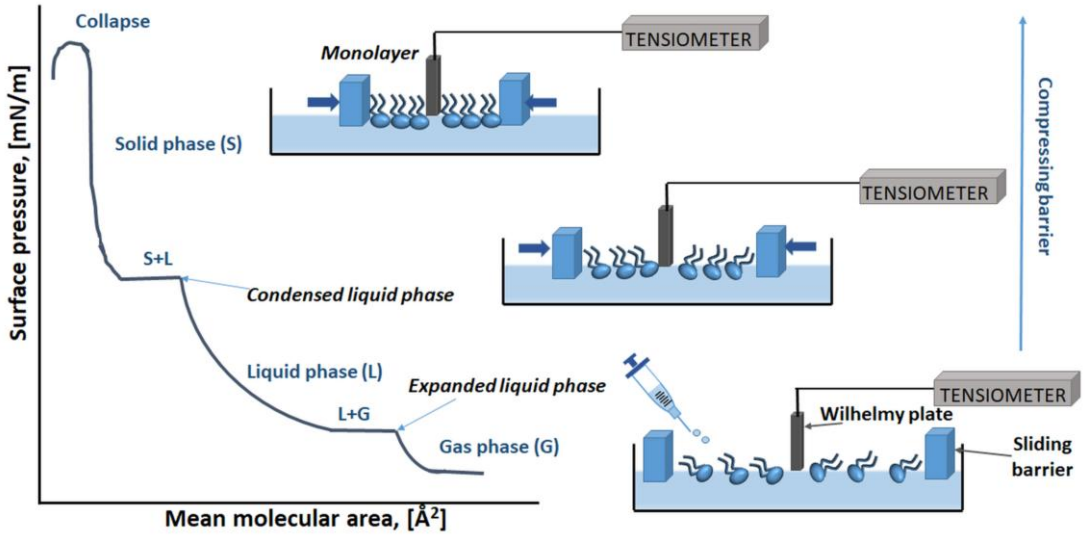

Figure 33. Representation of a compression isotherm as a function of the mean molecular area, with different physical states of the monolayer reported as a function of the surface pressure. Reprinted from Ref. (Rojewska, 2021).

Supported Lipid Bilayers (SLBs)

SLBs are lipid bilayers formed on smooth solid surfaces like silicon or mica. These bilayers can be created by fusing lipid vesicles onto the solid support or through techniques such as the Langmuir-Blodgett (LB) and Langmuir-Schaeffer (LS) methods (Clausell, 2004). The LB technique involves forming a Langmuir monolayer on a subphase, which is then transferred onto a solid substrate by vertically lifting the substrate through the monolayer. In the LS technique, a hydrophobic substrate is placed horizontally in contact with the Langmuir monolayer, allowing the lipid monolayer to transfer onto the substrate. In some cases, a combination of LB and LS techniques is used (Hughes, 2008). SLBs primarily enable the study of interactions with lipid head groups, and structural changes, morphology, and surface chemistry of SLBs following drug interactions can be examined using a variety of techniques, such as X-ray scattering, scanning electron microscopy (SEM), atomic force microscopy (AFM), and Fourier transform infrared (FTIR) spectroscopy (Liu, 2005).

Liposomes

Liposomes are spherical vesicles consisting of lipid bilayers surrounding an internal aqueous compartment. They can be unilamellar (with a single lipid bilayer) and vary in size from small (20–50 nm) to large (50–100 nm) to giant unilamellar liposomes (10–100 µm), with giant liposomes closely resembling the size of actual cells. Liposomes are commonly prepared by dissolving lipids in

organic solvents, evaporating the solvents to form thin lipid films, and then rehydrating the films in a buffer to form liposomes (Peetla, 2009). The resulting suspension is vortexed and sonicated to form multilamellar liposomes (MLVs), which are then subjected to freeze-thaw cycles to achieve uniform size. Giant unilamellar liposomes (GUVs) can be prepared by electroformation, where a lipid film is dried under an oscillating electric field. Liposomes are especially useful for studying the permeability of drugs and drug delivery systems, and various spectroscopic techniques, such as fluorescence and Raman spectroscopy, are employed to investigate biophysical interactions with lipids (Peetla, 2009).

4.2 The effects of the interaction of phenols with membrane models

In a study by Katata et al. in 2022, the effects of bisphenol A (BPA) on a membrane model made of DPPC, a phospholipid from the phosphatidylcholine class, and cholesterol were investigated (Katata, 2022). The research compared BPA's impact on a liquid-ordered phase model (DPPC/cholesterol mixture) and a gel-phase model (pure DPPC), as BPA appears to have a stronger effect on fluid models. The π-A isotherms of DPPC in ultrapure water demonstrated phase transitions from the liquid-expanded phase to the liquid-condensed phase (Figure 34A, black line). When BPA was introduced at a concentration of 1×10^{-5} mol/L, the monolayer shifted to larger areas during almost all the compression, suggesting that BPA stayed at the air-water interface between the lipid molecules (Figure 34A, red line). However, at higher surface pressures, the BPA molecules were partially expelled from the interface, leading to a rearrangement of the lipid molecules (Katata, 2022). The π-A isotherms showed a more compact monolayer for cholesterol in ultrapure water, as the expanded liquid phase was not present (Figure 34B, black line) (Ruiz, 2020). When BPA was introduced, a slight shift to larger areas occurred. This can be attributed to cholesterol's smaller, stiffer molecules, which prevented BPA from remaining at the air-water interface, as shown in Figure 34B (red line).

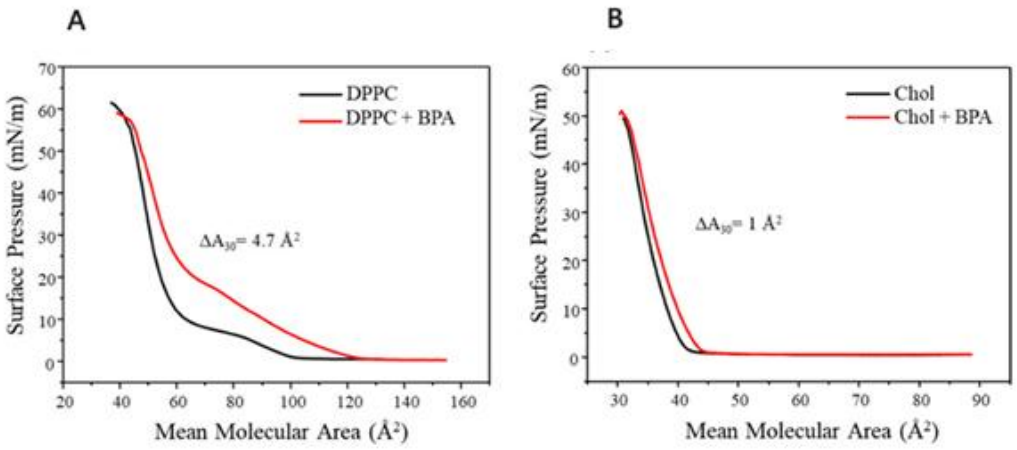

Figure 34. (**A**) Compression isotherms for the pure lipid DPPC (black line) and in the presence of bisphenol at a concentration of $1x10^{-5}$ mol/L (red line); (**B**) compression isotherms for cholesterol (black line) and with bisphenol (red line). Figure modified from Ref. (Katata, 2022).

In the case of the DPPC/cholesterol mixture, cholesterol-induced condensation in the DPPC monolayers causes the plateau in the isotherms to disappear (Figure 35, black line). The presence of BPA caused the isotherm to shift towards larger molecular areas during compression. Still, the overall profile did not change, suggesting that the fluidity of the monolayer remained unaffected (Figure 35, red line) (Katata, 2022).

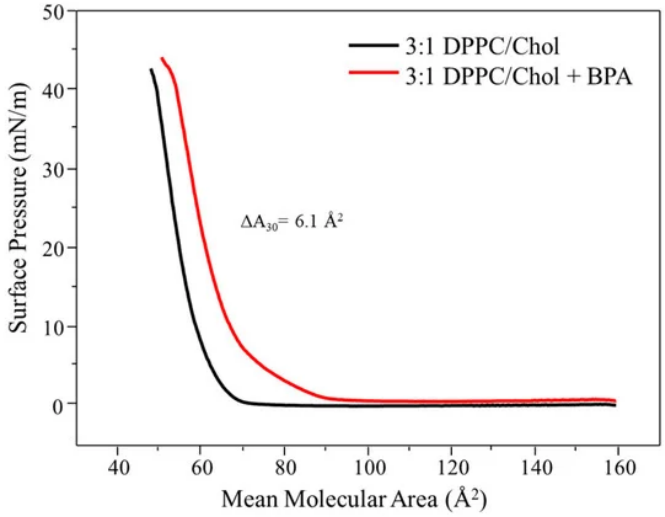

Figure 35. Compression isotherms for the DPPC/Chol mixture (black line) and in the presence of bisphenol at a concentration of $1x10^{-5}$ mol/L (red line). Reprinted from Ref. (Katata, 2022).

Maximino et al. (Maximino, 2021) conducted a similar study, exposing DPPC monolayers to BPA. They observed that BPA induced expansion in the monolayer and altered the isothermal profile. To investigate potential damage to hamster ovary cells (CHO), they combined Langmuir monolayer experiments with giant unilamellar vesicle (GUV) models and *in vitro* cell viability tests. Their results

indicated that higher BPA concentrations led to considerable changes in cell membrane patterns and CHO cells, possibly due to BPA's endocrine-disrupting properties. The effects were concentration-dependent and varied depending on whether BPA was aggregated.

Maximino et al. in 2022 (Maximino, 2022) studied the effects of BPA on a membrane model using the lipid 1,2-dioleoyl-sn-glycero-3-phosphocholine (DOPC). They performed experiments with Langmuir monolayers and GUVs to examine molecular interactions between DOPC and BPA. The data for DOPC monolayers in the aqueous subphase, both in the absence and presence of BPA (1×10^{-5} mol/L), revealed that the presence of BPA caused a shift to larger areas during compression, suggesting that BPA remained at the air-water interface even at high surface pressures (Maximino, 2022). However, this shift did not affect the profile of the π-A isotherms, indicating that BPA did not alter the fluidity of the monolayers (Figure 36A, red line). Further analysis of the DOPC monolayer's compressive modulus confirmed that BPA did not change the monolayer's elasticity (Figure 36B, red line). This could be due to DOPC's structure, which includes two unsaturated alkyl chains that provide greater fluidity compared to other lipids. This fluidity allows BPA to intercalate between DOPC molecules, remaining closer to the air-water interface without disrupting lipid fluidity. Overall, these studies highlight the complex interactions between BPA and lipid membranes, shedding light on BPA's potential effects on cell membranes and its endocrine-disrupting properties.

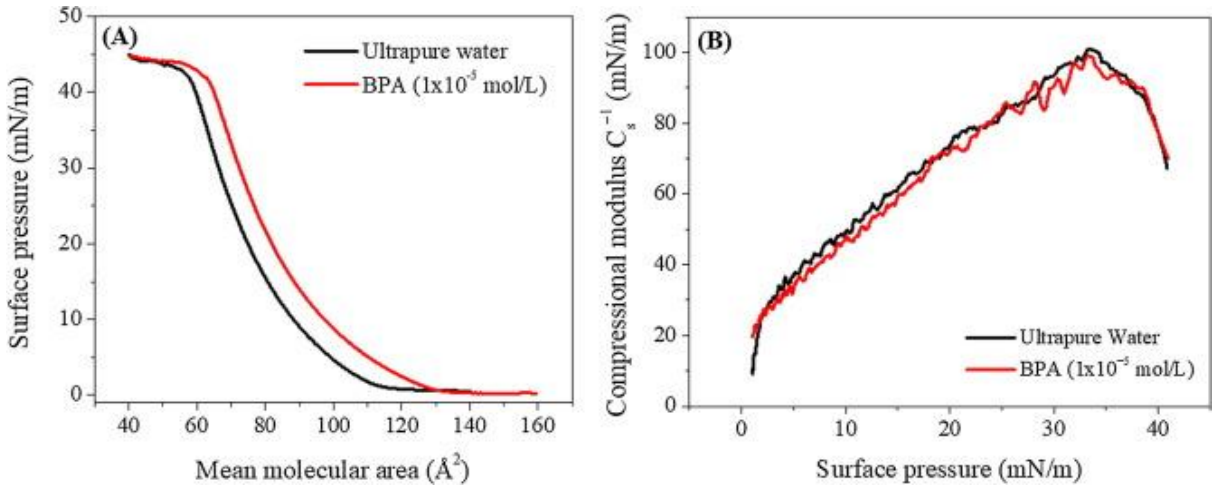

Figure 36. (**A**) Compression isotherms for the bare DOPC (black line) and in the presence of bisphenol at a concentration of 1x10^{-5} mol/L (red line). (**B**) Compressional modulus as a function of surface pressure (mN/m). Reprinted from Ref. (Maximino, 2022).

4.3 Interface measurements

4.3.1 Tensiometry and principle of surface pressure measurement

Tensiometry is a cornerstone methodology in interfacial science, enabling the precise quantification of surface (or interfacial) tension—an emergent phenomenon arising from cohesive forces between molecules at phase boundaries. Among the available techniques, the Wilhelmy plate method, originally described by Ludwig Wilhelmy, remains one of the most widely used. In this method, a clean, wetted plate—typically made of platinum or filter paper—is suspended vertically at the air–liquid interface, and the capillary force acting along its wetted perimeter is measured using a microbalance (Figure 37) (Wu, 1999). The surface pressure (π, in mN/m) is defined as the difference between the surface tension of pure water (γ_0 = 72.8 mN/m at 20 °C) and the surface tension in the presence of an interfacial film (γ), according to equation (3):

$$\pi = \gamma_0 - \gamma \quad (3)$$

Surface pressure is obtained by monitoring the vertical force exerted on the plate, which is oriented perpendicular to the air–water interface. To ensure reproducibility, the filter paper must have well-defined and consistent dimensions. A paper strip with a width (w) of 1 cm, a thickness (t) of 0.5 mm, and a surface area of 2.2 cm² was employed. Assuming complete wetting and constant temperature, the force measured is solely attributed to variations in surface tension.

When surfactant molecules are deposited at the interface, they self-organize to minimize the system's surface energy. As the number of molecules increases or the area per molecule decreases, the difference between γ_0 and γ becomes more pronounced, increasing surface pressure. Therefore, the evolution of surface pressure is directly related to intermolecular interactions: the stronger and denser the interactions, the higher the surface pressure. Conversely, a decrease in pressure indicates weaker interactions, which may reflect molecular desorption or loss from the interface.

The phenomenon of surface tension was first systematically described by Irving Langmuir in 1916 at the American Physical Society meeting in Cleveland. His studies on oil films at the air–water interface led him to propose a theory in which “the structure of the surface layer of atoms is considered to be the main factor determining the surface tension of a liquid” (Langmuir, 1917). According to this theory, amphiphilic molecules self-assemble at the interface such that their high-energy moieties orient toward the aqueous phase. At the same time, the lower-energy groups remain at the surface, forming a stable monolayer that minimises the overall surface energy.

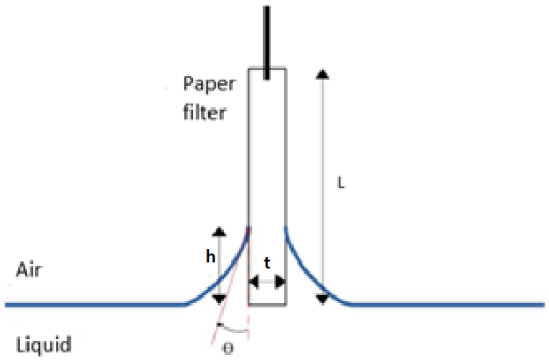

Figure 37. Graphic representation of the Wilhelmy plate method. The variation of the resultant force—acting perpendicular to the air-water interface—is measured on a rectangular sheet of filter paper in contact with the interface.

4.3.2 Ellipsometry measurements

Ellipsometry is a non-destructive optical technique used to investigate interfacial properties by measuring changes in the polarisation state of light upon reflection from a solid or liquid interface. The fundamental output of the method is the *ellipsometric angle* (Δ, in degrees), which quantifies the phase difference between light polarised parallel and perpendicular to the plane of incidence after reflection. This angle is directly related to the optical characteristics of the interface, particularly its refractive index and thickness.

For liquid interfaces, such as those studied using a Langmuir trough, the system is typically calibrated using the pure air/water interface as a reference, where Δ is set to 0°. This allows detection of subtle changes in interfacial properties, such as those induced by the adsorption of lipid molecules or the incorporation of pollutants.

A linearly polarised He-Ne laser (λ = 628 nm) is used, directed onto the liquid surface at an incidence angle of 52.12°, corresponding to approximately 1° below the Brewster angle. Upon reflection, the beam becomes elliptically polarised. It then passes through a quarter-wave plate (λ/4) that converts the elliptically polarised light back to linear polarisation. This beam subsequently passes through an analyser and is detected by a photomultiplier tube (PM). The ellipsometric angle Δ is calculated as twice the analyser angle, providing a measure of the phase shift between the s- and p-polarised components of the reflected light.

Ellipsometry is particularly sensitive to minute variations in interfacial thickness and refractive index, offering a typical measurement uncertainty of ±0.5°. The laser beam illuminates a surface area of approximately 1 mm² and is responsive to structural or compositional changes occurring within approximately 1 μm of the interface.

4.4 Atomic Force Microscopy

4.4.1 Basic principles of Atomic Force Microscopy

Understanding atomic and molecular scale concepts in chemistry and physics is often challenging due to the abstract nature of atoms and molecules (Zhong, 2003). However, state-of-the-art microscopy techniques, such as the Scanning Tunneling Microscope (STM), Atomic Force Microscope (AFM), and other Scanning Probe Microscopes (SPM), offer hands-on ways to visualize these entities. SPM microscopes are characterized by using a probe and surface brought into proximity, scanned with piezoelectric devices, and monitored using specialized circuitry (Leite, 2007). The type of SPM depends on the interaction studied, including ionic, electrostatic, van der Waals, and magnetic forces (Morris, 2003). Since its invention in the late 1980's the Atomic Force Microscope (AFM) has become a staple of nanotechnology (Dufrêne, 2017; Binnig, 1986).

By leveraging forces between a sharp probe and a sample surface, AFM achieved atomic-scale imaging shortly after its introduction (Binnig, 1987). It was later adapted to work across various environments and temperature ranges, including liquid settings (Muller, 2008; Muller, 2011). This adaptability made AFM a versatile tool, advancing discoveries in physics, chemistry, biology, and medicine. AFM's ability to operate in liquid environments and at physiological temperatures opened new possibilities for biological research. With innovations like optical detection systems and fluid chambers, AFM enabled high-resolution imaging of biomolecules and cells in their native states (Radmacher, 1992). The first imaging mode, contact mode, maps sample topography by maintaining constant probe force, achieving sub-nanometer resolution for soft biological surfaces. Early applications included imaging DNA, RNA (Hansma, 1992), cell membranes (Mou, 1995), and lipid films (Zasadzinski, 1994). Over time, AFM evolved with diverse imaging modes to address complex biological systems, ranging from proteins to tissues (Ando, 2013; Dufrene, 2013). These advancements, alongside complementary techniques like super-resolution and cryo-electron microscopy, expanded AFM's utility (Dufrêne, 2017). It now enables dynamic studies of biological processes, such as membrane protein interactions, toxin insertion, and photosynthetic membrane changes, offering insights into structural and functional dynamics in molecular and cellular biology.

The AFM can be used for two primary purposes: imaging (topographical studies) and atomic force spectroscopy (AFS) (Leite, 2005; Mosiewicki, 2006; Sirghi, 2000). Imaging captures structural or dynamic features of surfaces, applicable to semiconductors, biological systems, nanostructures, and polymers, achieving resolutions as fine as the atomic scale (Borato, 2006). AFS, on the other hand,

measures forces as a function of distance and allows manipulation of samples, enabling studies of molecular forces, biological systems, polymers, and interfacial (Evans, 2001).
In this PhD project, AFM is used to investigate the morphological alterations in lipid monolayers induced by catechol exposure. Following compressibility analysis via π-A isotherms, AFM imaging of the films transferred using the Langmuir-Blodgett technique reveals nanoscale changes in surface topography, domain organization, and phase distribution.
Comparing DPPC and DPPC/DOPC monolayers—chosen for their distinct phase behaviour—allows for evaluating catechol's impact on membrane structure and heterogeneity, providing molecular-level insight into its interaction with lipid interfaces.

4.4.2 Experimental aspects of AFM measurements

The AFM system includes key components: a micro-cantilever (Si, SiO_2, or Si_3N_4, with a length on the order of a few hundred micrometers) with a probe, motion detection devices, a feedback loop, a piezoelectric scanner, and a computer for image processing (Krieg, 2019). AFM detects weak interatomic forces between the probe tip and the sample surface to analyze surface structure and properties with nanometer resolution (Deng, 2018). AFM relies on the scanning probe, with silicon micromachining technology being the standard for cantilever production (Wolter, 1991). Figure 38(a) shows a scanning electron microscope image of a silicon nitride cantilever chip used for contact AFM. The cantilever includes a small pyramid-shaped tip, as seen in Figure 38(b). Different cantilevers and tips are utilized depending on the imaging mode. In contact mode, cantilevers require low stiffness (below the interatomic elastic constant of solid atoms). In contrast, the non-contact and tapping modes benefit from higher stiffness to minimize noise and instability. Figure 38(c) depicts a cantilever with a silicon tip for dynamic operation, and Figure 38(d) offers a detailed view of the silicon tip. AFM cantilevers exhibit elastic constants ranging from 0.01 to 100 Nm^{-1}, enabling force sensitivity up to 10^{-11} N, limited by thermal, electrical, and optical noise interactions (Alessandrini, 2005).

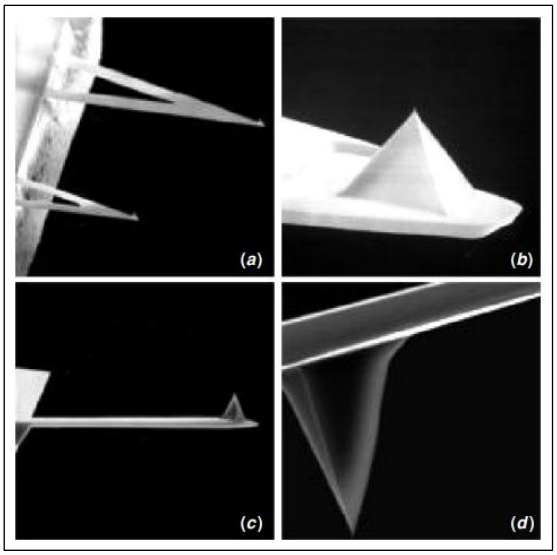

Figure 38. Scanning electron microscope images display microfabricated AFM cantilevers. These include (a) silicon nitride cantilevers and (c) silicon cantilevers, with detailed high-magnification views of their tips, showing (b) an oxide-sharpened apex and (d) a silicon tip for enhanced precision. Reprinted from Ref. (Alessandrini, 2005).

The cantilever, sensitive to these forces, deforms or changes its motion, enabling sensors to record force distribution and surface morphology during scanning. The cantilever bends upward or downward based on attractive or repulsive interactions between the probe and the surface. These deflections are detected by reflecting a laser off the cantilever onto a photodiode detector. The AFM scanner moves in X, Y, and Z directions, with the Z-axis typically limited to a few microns (Figure 39A) (Maver, 2016). By reconstructing the piezoelectric scanner's position, users obtain 3D topographical images. AFM also measures mechanical properties like elastic modulus, adhesion, and stiffness via force-distance curves. Using dedicated software, nano-indentation data enables quantitative material analysis, with lower Young's modulus values indicating higher sample deformability (Fan, 2018; Jalili, 2004).

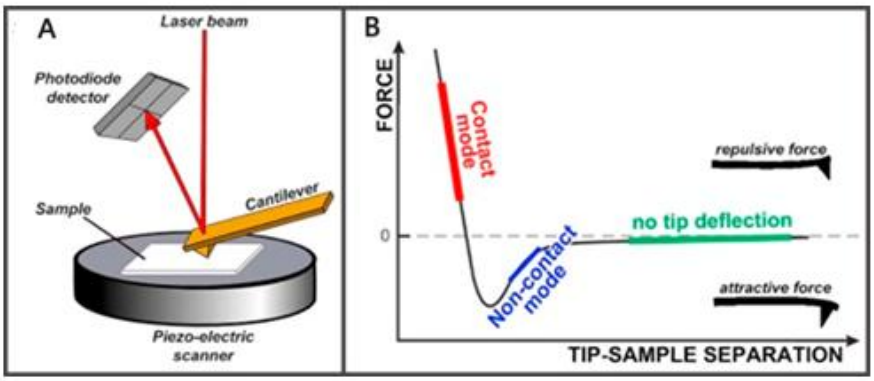

Figure 39. Principles of atomic force microscopy. a) Graphical representation of AFM operation; b) Interaction forces between an AFM tip and a sample through a force-displacement curve. Figure modified from Ref. (Maver, 2016).

The interaction forces between an AFM tip and a sample are depicted in a force-displacement curve, as shown in Figure 39B (Maver, 2016). At large interatomic distances, weak attractive forces increase as atoms approach. When electron clouds overlap, electrostatic repulsion reduces attraction at a distance of a few angstroms, forces balance, becoming fully repulsive when the atoms are in contact, marking the transition from attraction to repulsion. AFM operates through three primary imaging modes: contact mode (or static mode), where the probe maintains contact with the sample; non-contact mode (or dynamic mode), detecting atomic attraction from a distance; and tapping mode (or dynamic mode), where the cantilever oscillates at the resonance frequency, intermittently contacting the sample (Jalili, 2004). Tapping mode minimizes lateral forces and adsorption effects, delivering high-resolution imaging suitable for observing biological samples' ultrastructure. In detail, the contact mode, the earliest AFM mode, involves the tip moving across the surface and deflecting according to its profile. It has two types: constant force mode, which uses a feedback loop to maintain consistent tip deflection and measures surface topography, and constant height mode, which detects rapid structural changes by observing cantilever deflection (Maver, 2016). While contact mode provides high-resolution data, it generates frictional forces that may damage soft samples like polymers or biological macromolecules (Figure 40). It is commonly used for studying solid pharmaceutical formulations and fixed cells (Bhushan, 2010; De, 2010). The non-contact mode employs cantilevers with large spring constants that hover close to the surface (5-10 nm) without direct contact, avoiding frictional forces and preserving sample integrity (Maver, 2016). This mode is ideal for examining biological samples, single polymer chains, and cell surface regions, though its lateral and height resolutions are lower compared to contact mode (Figure 40) (Morita, 2015; Seifert, 2015; Sugihara, 2012). Tapping mode AFM (T-AFM) addresses the limitations of contact mode by oscillating the cantilever near its resonant frequency. The vibrating tip intermittently taps the surface, minimizing friction and adhesion. Changes in vibration amplitude due to surface topography are detected and regulated by a feedback loop, maintaining constant oscillation amplitude and ensuring precise imaging (Jalili, 2004). Tapping mode excels in analyzing soft samples like biological structures and provides high-resolution data with minimal damage (Figure 40).

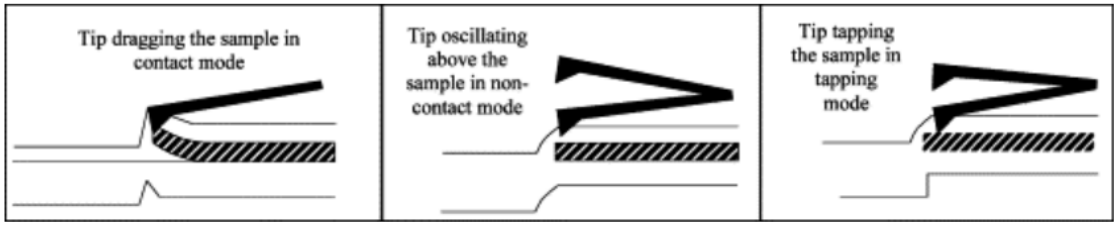

Figure 40. Representation of the mechanism behind contact mode (left), non-contact mode (centre) and tapping mode (right). Reprinted from Ref. (Jalili, 2004).

AFM's versatility and adaptability across contact, non-contact, and tapping modes enable detailed molecular-level imaging and analysis of mechanical and structural properties, making it invaluable in nanotechnology, biomedical research, and pharmaceutical sciences (Deng, 2018).

5. Materials and Methods

5.1 Materials and Experimental Procedures for Absorption and Fluorescence measurements

5.1.1 Materials for Absorption and Fluorescence measurements

All chemicals and commercial laccase were purchased from Sigma (Sigma Italia, Milan, Italy). Solutions of free laccase (from *Trametes versicolor*) at a concentration of 1 mg/mL (in 0.1 M acetate buffer at pH 5; in 0.1 M phosphate buffer at pH 6.5 and in 0.1 M acetate buffer at pH 4.5), 0,5 mg/mL (in 0.1 M acetate buffer) and 8 μg/mL (in 0.1 M acetate buffer at pH 5) were obtained. The catechol was dissolved in 0.1 M acetate buffer pH 5, at different concentrations from 0.0001 to 10 mM.

5.1.2 Experimental Procedures for Absorption and Fluorescence measurements

The absorption spectra were acquired in the 200-900 nm range (using a disposable cuvette) with a JASCO 630 V spectrophotometer, equipped with a UV Winlab software package. This software allows you to select the type of application, scan or concentration, will enable you to enter the parameters to be used by varying the wavelength at which the absorption is to be read, and allows you to modify the data pitch, scan speed and spectral bandwidth. The scan speed was 400 nm/min, the data pitch was 0.5 nm, and the spectral bandwidth was 1.5 nm. For the absorption measurements performed, error bars of approximately 10% were obtained.

The emission fluorescence spectra were collected with a spectrofluorimeter (Perkin-Elmer, model LS55) equipped with a Deuterium and a Xenon discharge lamp with an emission spectrum ranging from 200 to 800 nm. In the UV range, samples were excited at 280 and 320 nm, using a quartz cuvette. Spectra were acquired with excitation and emission slits fixed at 5 and 2.5 nm, respectively; the scan speed was 200 nm/min. Data analysis was performed using Origin Pro 7.5 software (OriginLab, Northampton, MA, USA). The emission spectrum following an excitation at 632 nm was obtained using a Raman microspectroscopy apparatus equipped with a He-Ne laser (632 nm) and a nitrogen-cooled CCD detector. For the fluorescence measurements performed, error bars of approximately 10% were obtained.

5.2 Materials and Experimental Procedures for Raman and SERS measurements

5.2.1 Materials for Raman and SERS measurements

5.2.1.1 Chemicals

Tetrachloroauric acid (III) trihydrate ($HAuCl_4 \cdot 3H_2O$), sodium citrate ($C_6H_5Na_3O_7 \cdot 2H_2O$) and catechol ($C_6H_6O_2$) were purchased from Sigma-Aldrich (Sigma-Aldrich Co., USA). All chemicals were used as received.

The catechol standard solution (180 mM) was obtained using ultrapure water, and different concentrations of catechol solutions were prepared by diluting the standard solution with ultrapure water. A drop of solution was placed on a glass microscope slide to investigate Raman's measurements of catechol.

5.2.1.2 Commercial SERS substrates

Five commercial SERS substrates with different characteristics (described in Table 4) were considered and optimized for use with an excitation wavelength of 532 and 785 nm. The main details about these substrates are summarised in Table 4. As can be seen by inspecting the table, all the substrates are based on the use of gold or silver nanoparticles (AuNPs or AgNPs) and various supports. In the considered commercial substrates, the laser excitation wavelength recommended by the manufacturer was used: when substrates based on the use of only AuNPs are used, a laser emitting at 785 nm was used, while when only AgNPs-based substrates are used, the recommended wavelength is 532 nm. When both AuNPs and AgNPs are used, both wavelengths can be used and were usually used in the present study. In Table 4, some details about the substrates are given.

SERS commercial substrate	Recommended laser excitation wavelength	Substrate material	SERS active area
RAM-SERS-Ag, manufactured by Ocean Insight	532 nm	Polymer fibers are covered inhomogeneously with silver nanoparticles.	5.5 mm diameter circle
RAM-SERS-Au, manufactured by Ocean Insight	785 nm	Polymer fibers are covered inhomogeneously with gold nanoparticles.	5.5 mm diameter circle
Silver-SERStrate manufactured by Silmeco ApS	532 nm	Silicon nanopillars coated with silver nanoparticles.	3 mm x 3 mm
Gold-SERStrate manufactured by Silmeco ApS	785 nm	Silicon nanopillars coated with gold nanoparticles.	3 mm x 3 mm
Premium-Ag-Au manufactured by SERSitive	532 and 785 nm	Silver and gold nanoparticles deposited on ITO glass.	5 mm x 4 mm (width x height)

Table 4. Summary of the commercial SERS substrates evaluated, including details on manufacturer, substrate material, and recommended excitation wavelength.

Among these substrates, RAM-SERS-Au and RAM-SERS-Ag substrates were purchased from Ocean Insight (USA); they consist of polymer fibers (observed from the microscopic images in Figure 41) inhomogeneously covered with gold nanoparticles (in the case of RAM-SERS-Au) or silver nanoparticles (in the case of RAM-SERS-Ag) properly placed on a microscope slide; then they were vacuum-packed and sealed. Images of the microscope slides with the substrates are shown in Figure 42. The substrates produced by Ocean Insight were immersed directly in the catechol solution placed in a container, as evaporation issues arose when the solution was applied directly to the surface of these substrates. However, this evaporation problem was not observed with the other commercial substrates studied.

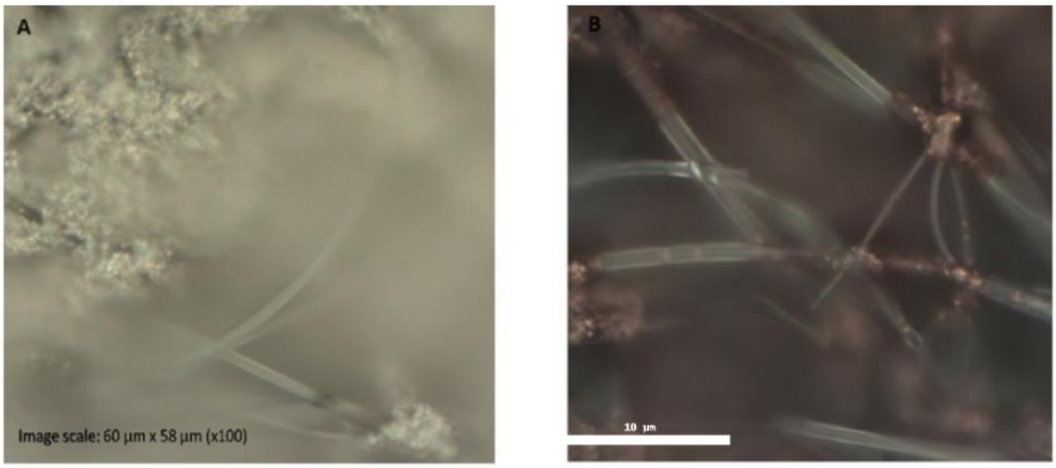

Figure 41. Microscope images of commercial substrates supplied by Ocean Insight. **A**) RAM-SERS-Ag substrate with x100 optical objective. **B**) RAM-SERS-AU substrate with x100 optical objective and 10 µm size bar.

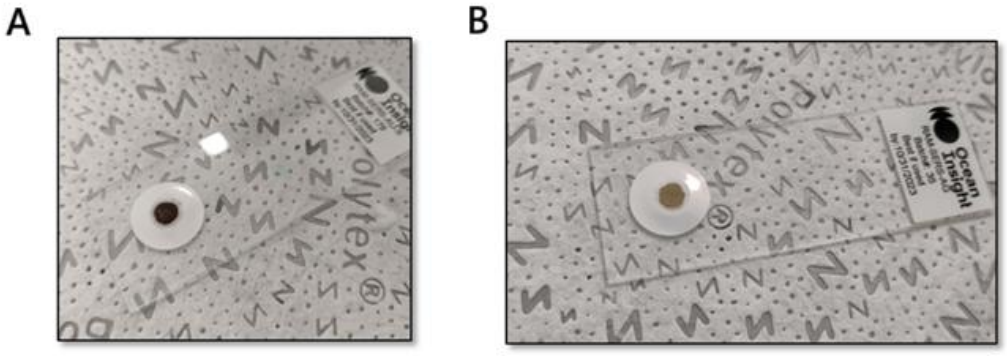

Figure 42. Images of RAM-SERS-Au (A) and RAM-SERS-Ag (B) substrates from Ocean Insight.

Gold-SERStrate and Silver-SERStrate substrates were purchased from Silmeco ApS (Denmark); each substrate consisted of independent silicon nanopillars coated with gold/silver (for Gold- and Silver-SERStrate, respectively) and was vacuum sealed. Images of substrates with a drop of the catechol solution deposited are shown below (Figure 43).

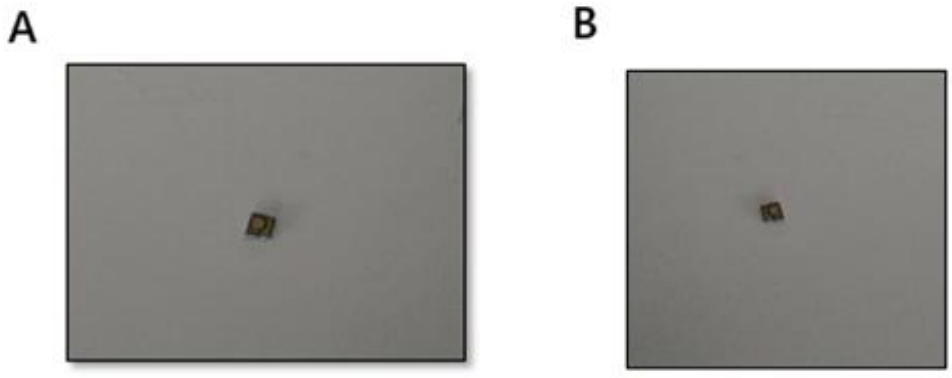

Figure 43. Images of Gold-SERStrate (**A**) and Silver-SERStrate (**B**) substrates from Silmeco ApS. The dimensions of the substrates are 3 mm x 3 mm.

Premium-AgAu substrates purchased from SERSitive (Poland) are made with a mixture of silver and gold nanoparticles deposited randomly and non-uniformly on an indium tin oxide (ITO) glass surface (Figure 44). They were stored in air, packed in small microcentrifuge tubes and placed under a vacuum.

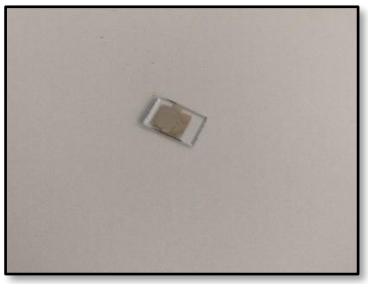

Figure 44. Image of Premium-AgAu substrate from SERSitive. The dimension of the substrate is 9 mm x 7 mm x 0,7 mm (width x height x thickness).

5.2.1.3 Homemade substrates

Besides the above-described commercial substrates, a homemade substrate was prepared according to previous reports and used (Camerlingo, 2019; Delfino, 2014). It is based on the use of a homemade AuNPs solution placed on microscope slides. Accordingly, as the first step, the needed AuNPs solution was prepared, characterized and then used to make the substrate.

AuNPs solution preparation and characterization

AuNPs were obtained by the conventional citrate reduction method (Frens, 1973). It is briefly described in the following.

A 0.01% $HAuCl_4 \cdot 3H_2O$ (tetrachloroauric acid (III) trihydrate) solution was reduced by 1% $C_6H_5Na_3O_7 \cdot 2H_2O$ (sodium citrate) with vigorous stirring near boiling temperature. AuNPs' size was controlled by adjusting the amounts of sodium citrate, according to the literature (Delfino, 2014). Accordingly, the procedure was optimized to obtain a solution of gold nanoparticles with an expected diameter of 20±5 nm. In detail, the following protocol was applied:

1. All glassware was washed with acetic acid and left to soak for over two days.
2. Preparation of the initial stock solution (A): 1g of tetrachloroauric acid (III) trihydrate ($HAuCl_4 \cdot 3H_2O$) to which 250 mL of distilled H_20 was added. The final solution has a 4 mg/mL concentration and is stored in a 500 mL dark bottle.

3. Preparation of initial stock solution (B): 100 mg of sodium citrate ($C_6H_5Na_3O_7 \cdot 2H_2O$) to which 10 mL of distilled H_20 is added in a 25 mL beaker. The final solution has a concentration of 38.8 mM (1% m/v).
4. 10 mL of distilled water is taken, adding 250 µL of HAuCl4·3H2O (stock A). The solution is brought to a boil at 100° (in a 50 mL beaker) and stirred continuously with a magnetic stirrer. Cover the beaker with aluminium, but not hermetically.
5. Once it had come to a boil, 300 µL of $C_6H_5Na_3O_7 \cdot 2H_2O$ (stock B) was added to the solution to control the nanoparticle size.
6. 3 minutes after the addition of the reducing agent, the solution will show a characteristic colouration that is indicative of the population of nanoparticles to which a certain diameter corresponds.
7. After about an hour and a half, a solution of nanoparticles with an expected diameter of 20±5 nm was obtained (red-orange colouration).

Absorption spectroscopy was used to study the stability of the AuNPs solution. The spectrum, reported in Figure 45, shows the presence of a single broad peak in the 350-650 nm range. It represents the surface plasmon resonance absorption (SPR) band of metal nanoparticles, which can provide valuable information on the structure and aggregation of AuNPs, peaking at 524 nm, thus confirming the expected diameter range (Delfino, 2014; Haiss, 2007). The stability of the preparations was studied by acquiring absorption spectra at a fixed time for several days; the analysis of the SPR peak position confirmed the solution's stability for three days. Accordingly, the AuNPs solution was used within the stability time.

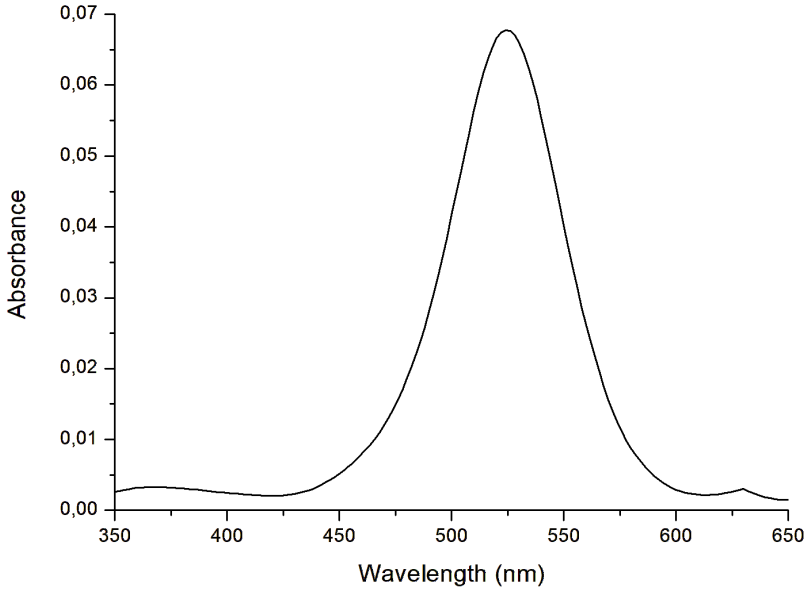

Figure 45. UV–Vis absorption spectrum of gold nanoparticles, exhibiting a distinct surface plasmon resonance (SPR) peak at 524 nm, characteristic of well-dispersed spherical AuNPs. The position of the SPR peak provides insights into particle size, distribution, and aggregation state.

AuNPs-based homemade SERS substrate preparation

According to the literature, homemade substrates were fabricated by placing a drop of the obtained gold nanoparticle solution on a glass slide and leaving it to dry overnight.

5.2.2 Experimental Procedures for Raman and SERS measurements

Two different setups were used to study the Raman spectrum of catechol and perform SERS measurements: a LabRAM HR Evolution microspectrometer (HORIBA Scientific), available at the IPR (Institut de Physique de Rennes, France) and a micro-Raman spectrometer (XploRATM One, HORIBA Scientific) available at the University of Tuscia. For measurements with the LabRAM HR Evolution microspectrometer, the spectra were recorded in the 200-1800 cm^{-1} range, with laser lines of 405, 532, 633 and 785 nm, and a laser power on the sample of 36 mW, 102 mW, 19 mW and 102 mW, respectively. When we used the optical density filter of 1 (10%), the laser power on the sample was 8.6 mW, with a 785 nm laser line. Whereas, with an optical density filter of 3 (0.1%), the laser power on the sample was 0.08 mW, with a 532 nm laser line. Spectra were acquired summing up to 1 accumulation and an acquisition time of up to 2s and 0.5s. The optical objectives used were x100 and x010, and a diffraction grating of 600 grooves/mm.

With the micro-Raman spectrometer (XploRATM One, HORIBA Scientific), data were collected in the 200-1800 cm^{-1} range and using a laser power of 8.5 mW and 28.5 mW (obtained using the available optical density filters) for 532 nm (He-Ne laser) and 785 nm (diode laser), respectively. Spectra were acquired by summing up to 6 and 4 accumulations and an acquisition time of up to 10 s and 2s, respectively. Laser light was focused on the sample using a 50x optical objective and a diffraction grating of 1200 and 1800 grooves/mm.

The LabSpec 6 Software (HORIBA Scientific) was used for instrument control, spectral acquisition and processing. Data analysis was performed using Origin Pro 7.5 software (OriginLab, Northampton, MA, USA). Smoothing was employed to reduce spectral noise, and baseline correction was performed to subtract the baseline shift for all spectra. Information on each peak was obtained using the LabSpec 6 Software. For the SERS measurements performed, error bars of approximately 10% were obtained.

A few microlitres of catechol solutions (70 mM, 7 mM, 1 mM, 0.5 mM and 0.1 mM concentrations) were placed in the SERS active area of commercial and homemade AuNPs substrates and measurements were performed immediately.

5.3 Materials and Experimental Procedures for investigating the interaction between catechol and membrane models.

5.3.1 Materials

The lipids 1,2-dipalmitoyl-sn-glycero-3-phosphocholine (DPPC) with purity >99% and 1,2-dioleoyl-sn-glycero-3-phosphocholine (DOPC) with purity >98% were purchased from Larodan (Monroe, USA). Catechol (purity ≥ 98%) was purchased from CaymanChem (Michigan, USA), and chloroform was purchased from Sigma Aldrich Ltd. (St. Quentin Fallavier, France). The DPPC solution and the DPPC/DOPC mixture (1:1 ratio) with a concentration of 1 mM were prepared in chloroform. The catechol solutions were prepared using ultrapure water at two subphase concentrations of $1x10^{-5}$ mol/L and $1x10^{-2}$ mol/L. The chemical structures of DPPC and DOPC are shown in Figure 46.

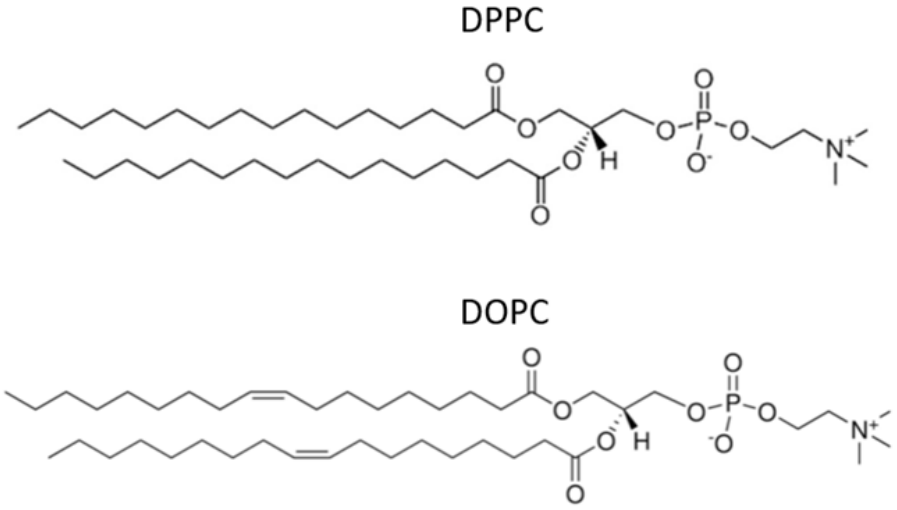

Figure 46. Chemical structures of the lipids 1,2-dipalmitoyl-sn-glycero-3-phosphocholine (DPPC) and 1,2-dioleoyl-sn-glycero-3-phosphocholine (DOPC).

5.3.2 Experimental Procedures

5.3.2.1 Ellipsometry and surface pressure measurements at the air/water interface

A circular Teflon trough, with a subphase volume of 8 mL (and a surface area of 27 cm^2), was used to study the ability of catechol to adsorb at the interface. Before each experiment, the Teflon trough was cleaned with ultrapure water to eliminate any surface-active residual contaminants (Kergomard, 2022). Control ellipsometric and tensiometric measurements were conducted to verify the cleanliness of the surface before the experiments. Surface pressure (π), which reports the lateral interaction of the particles, was measured using the Wilhelmy-plate method, with a filter paper connected to a microelectronic feedback system to monitor the surface pressure (Nima Technology, UK) (Figure 47). π values were recorded every 4 seconds with an accuracy of $\pm$ 0.2 mN/m.

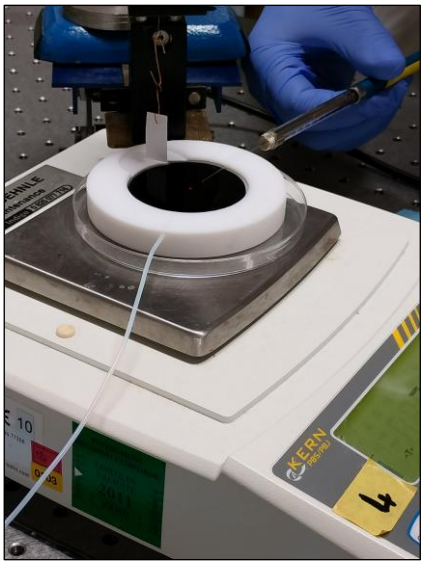

Figure 47. Image of a small circular Teflon trough, on which catechol solutions were introduced into the subphase solution through a hole using a microsyringe. Surface pressure (π) was measured using the Wilhelmy-plate method, with a filter paper in contact with the interface, and connected to a microelectronic feedback system (available at IPR, Rennes, France).

Ellipsometric measurements (ellipsometric angle, Δ°), which study the amount of matter at the interface, were performed using a custom-built automated ellipsometer in a "null ellipsometer" setup. The laser beam interacted with a surface area of 1 mm² and a depth of approximately 1 μm, providing information on the film thickness. Δ values were recorded every 4 seconds with an accuracy of ± 0.5° (Figure 48) (Bourlieu, 2020).

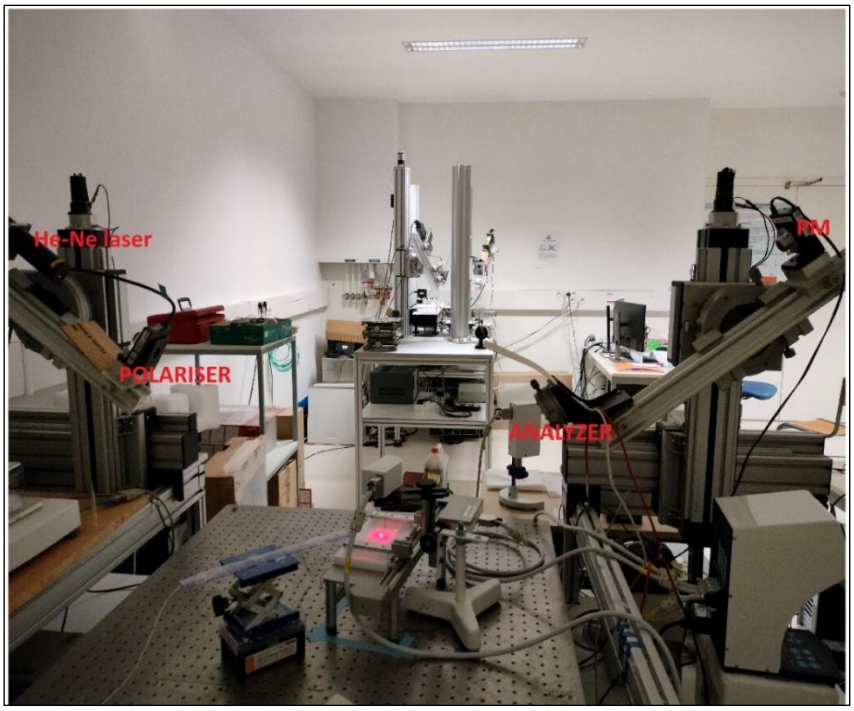

Figure 48. Overview of the experimental ellipsometer setup (available at IPR, Rennes, France): a He-Ne laser (λ = 633 nm) is linearly polarised, reflected by the Langmuir trough surface, and becomes elliptically polarised. A quarter-wave plate and rotating analyzer convert and extinguish the beam, with intensity detected by a photomultiplier (PM).

Catechol solutions at concentrations of $1x10^{-5}$ mol/L and $1x10^{-2}$ mol/L were introduced into the subphase solution through a hole in the trough using a microsyringe. Surface pressure recordings started immediately after the catechol solution was injected into the subphase and continued for 40 minutes following the stabilization of the surface pressure (Figure 47). The kinetics over 40 minutes is crucial for evaluating the adsorption of catechol solutions at the interface, and this is the period necessary to acquire a lipid compression isotherm.

5.3.2.2 Langmuir Films

Langmuir films of DPPC and the DPPC/DOPC mixture (1:1) (1 mM in chloroform) were spread on ultrapure water, and a subphase containing 1×10^{-5} and 1×10^{-2} mol/L catechol in a Langmuir trough (KSV Nima, Helsinki, Finland) with a surface area of 76 cm², controlled by two movable barriers (Figure 49A). After allowing 10 minutes for the solvent to evaporate, the lipid films were compressed by moving the barriers at a speed of 5 mm/min and analyzed using surface pressure vs. mean molecular area (π-A) isotherms (Figure 49B). All experiments were conducted in duplicate at 23±1 °C.

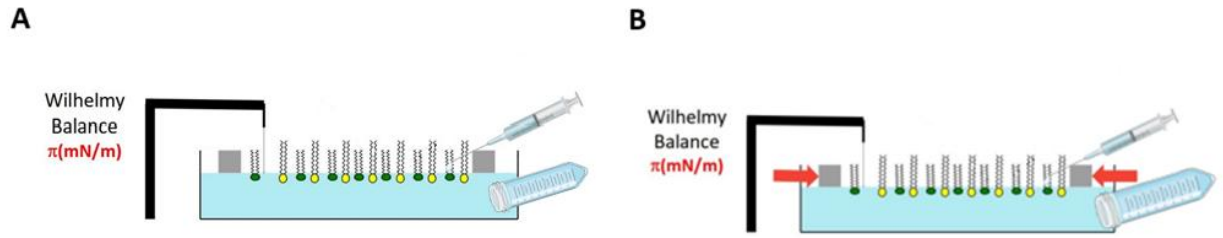

Figure 49. Explanatory images of **A**) lipid films injection at the interface, in the presence and absence of a catechol solution at 1×10^{-5} and 1×10^{-2} mol/L concentrations in the subphase. **B**) isotherms compression in the presence and absence of a catechol solution at 1×10^{-5} and 1×10^{-2} mol/L subphase concentrations.

5.3.2.3 Atomic force microscopy

AFM imaging of Langmuir-Blodgett films was carried out in contact mode QNM (Quantitative Nanomechanics Measurements) in air using a Multimode Nanoscope 8, Bruker (France). The interfacial films were transferred onto a mica substrate using the Langmuir-Blodgett technique at a controlled speed and surface pressure (5 mm/min at 20 mN/m) (Figure 50A-B).

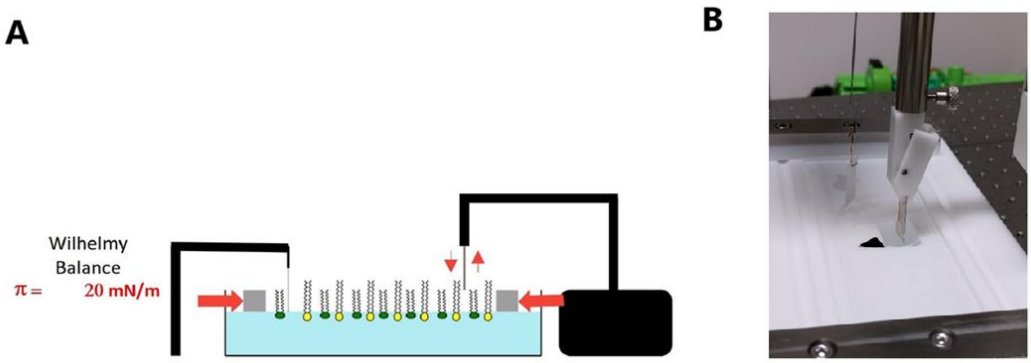

Figure 50. (**A**) Graphic representation of sampling using the Langmuir-Blodgett technique. (**B**) Image of interfacial film transferred onto a mica substrate.

A silicon cantilever (0.06 N/m, SNL-10, Bruker, France) and a scan rate of 1 Hz were employed for the topographic imaging. Images were captured in two distinct areas of each sample with scanner sizes of 20×20 µm², 10×10 µm², and 5×5 µm². The images were processed using Gwyddion software (version 2.62) and analyzed with KaleidaGraph software.

The height of the lipid films was measured using the "Profile tool" in Gwyddion software, which extracts profiles along arbitrary lines drawn. The analysis was conducted by selecting six profiles from a 2.5×2.5 µm² area.

The fractured morphology of the DPPC monolayer (expressed as a percentage) was analyzed on the 10×10 μm² images in terms of the relative area covered by the branches using *ImageJ* software by setting a threshold level.

Means comparisons were made using a Student t-test ($p < 0.05$).

6. Results and Discussion

This chapter reports the experimental results obtained during the PhD activity. The results focusing on testing the possibility of realizing an optical biosensing approach for catechol detection based on the use of commercial laccases are reported in the first subsection. In the second one, the outcomes of the research activity for testing a detection method for catechol based on SERS are discussed. The last subsection includes the results of the study of the interaction of catechol with model membranes, representing the first step for designing future innovative sensing approaches, potentially enabling the investigation of catechol quantity in cells by profiting from its effects on membranes.

6.1 Laccase-based optical biosensing schemes for catechol detection

Although optical biosensors have been less frequently reported in the literature despite the notable optical properties of laccases, experimental data show that optical biosensors generally exhibit high sensitivity (Shleev, 2004; Rodríguez-Delgado, 2015). Laccases and the reaction products of phenols display significant optical properties in the UV and visible spectra, which have primarily been used to develop spectrophotometric methods for assessing laccase activity. These methods can be adapted for biosensing, considering that laccase interacts with different phenols to produce absorption spectra with varying characteristics (Lepore, 2017).
In this framework, we report the results of research activity aiming to study optical biosensing schemes useful for catechol detection using laccase from *Trametes versicolor* as a biotic element, profiting from the peculiar properties of laccase (paragraph *1.4*). Once the proper conditions for the most promising detection schemes were identified and selected, the first step was to study the UV-VIS absorption and fluorescence emission of laccase and catechol in solution, investigating their interaction.

6.1.1 Absorption measurements

6.1.1.1 Characterization of Laccase and catechol in solution

In Figure 51, representative absorption spectra of laccase from *Trametes versicolor* dissolved in two different buffers (1 mg/mL in 0.1 M acetate buffer at pH 4.5 and 1 mg/mL in 0.1 M phosphate buffer at pH 6.5) are shown in the 250-900 nm range. In all cases, the contributions of tyrosine and tryptophan at 280 nm are noticeable, along with a weak shoulder located around 320 nm due to the

T3-type copper site. The contribution of the T1-type copper site (at 610 nm) is also observed (see the inset), even if it is reduced compared to results reported in another study (Shleev, 2004), where enzyme purification procedures were used (Lepore, 2017; Shleev, 2004; Delfino, 2015). The same results were also obtained by dissolving laccase from *Trametes versicolor* at a concentration of 1 mg/mL in 0.1 M acetate buffer at pH 5.

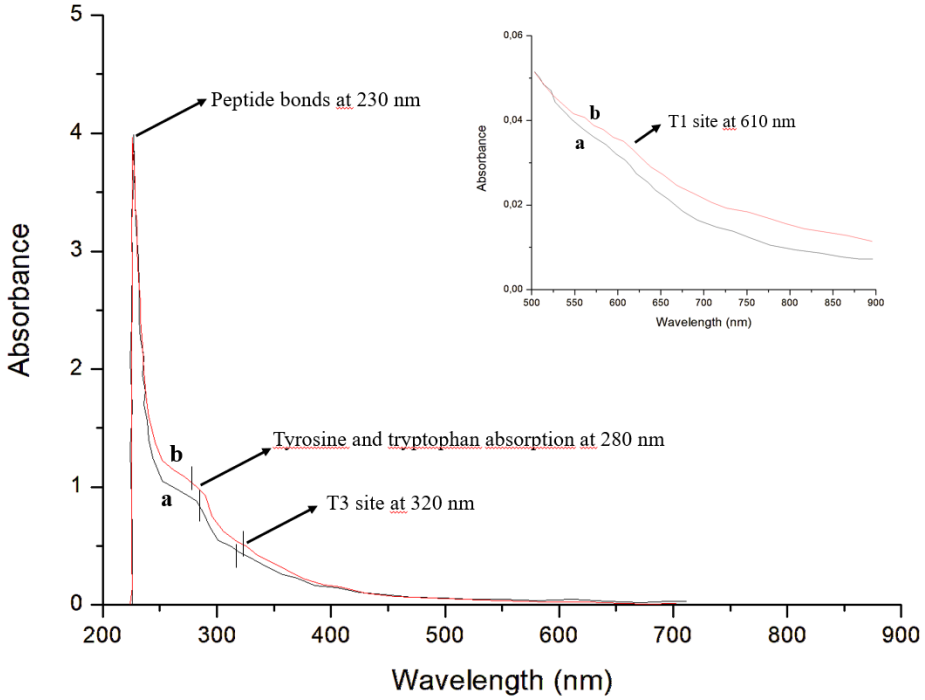

Figure 51. Absorption spectra of the laccase solution from *Trametes versicolor* at a concentration of 1 mg/mL solution in 0.1 M phosphate buffer at pH 6.5 (**a**) and in 0.1 M acetate buffer at pH 4.5 (**b**). In detail the spectra in the 500-900 nm region.

In Figure 52, a representative absorption spectrum of catechol solution (0.4 mM in 0.1 M acetate buffer at pH 5) is reported, showing a band peaking at 275 nm (Lepore, 2017). The attribution of the peak is still under study.

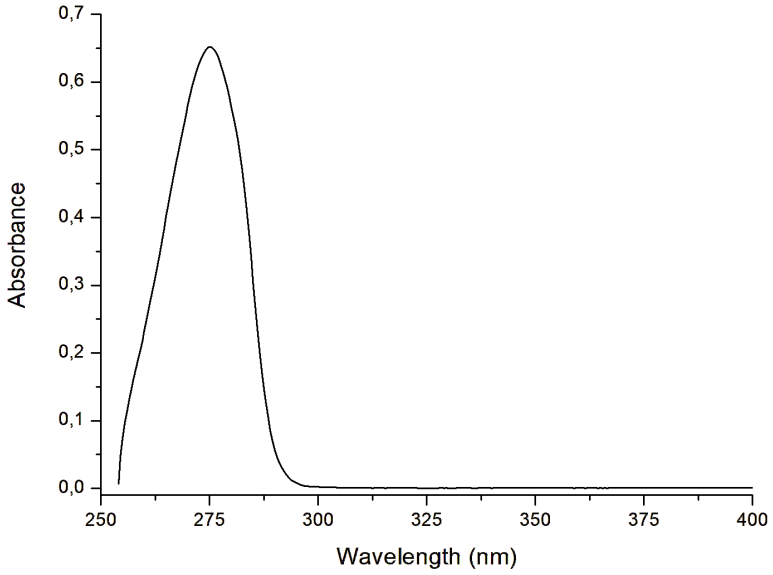

Figure 52. Absorption spectrum of catechol solution (concentration 0.4 mM in 0.1 M acetate buffer at pH 5).

6.1.1.2 Absorption measurements of solutions of laccase and catechol

As reported in paragraph *1.4*, laccase can catalyze the oxidation of phenols by oxygen in a solution, leading to the formation of water and quinones. These reactions can be monitored by following the evolution of the absorption spectra of the solution for obtaining absorption changes at an appropriate wavelength (depending on the phenol compound) since the products feature specific absorption spectra (Lepore 2017). To obtain information about the characteristics of the reaction, the absorbance values at the maximum absorbance can be analysed. It is well-known that a new absorbance peak at around 400 nm is observed in laccase solutions with catechol, the peak being typical of the *o*-quinone, the product of the oxidation reaction (Lepore, 2017; Dencheva, 2021). Accordingly, as a first step of the characterization of laccase-catechol interaction, the absorbance at 400 nm of 1 mg/ml laccase solutions with catechol at different concentrations in the range of 0.1-10 mM was detected; the experimental values as a function of catechol concentration are reported in Figure 53. The data confirms that the absorbance increases with concentration, with non-linear behaviour.

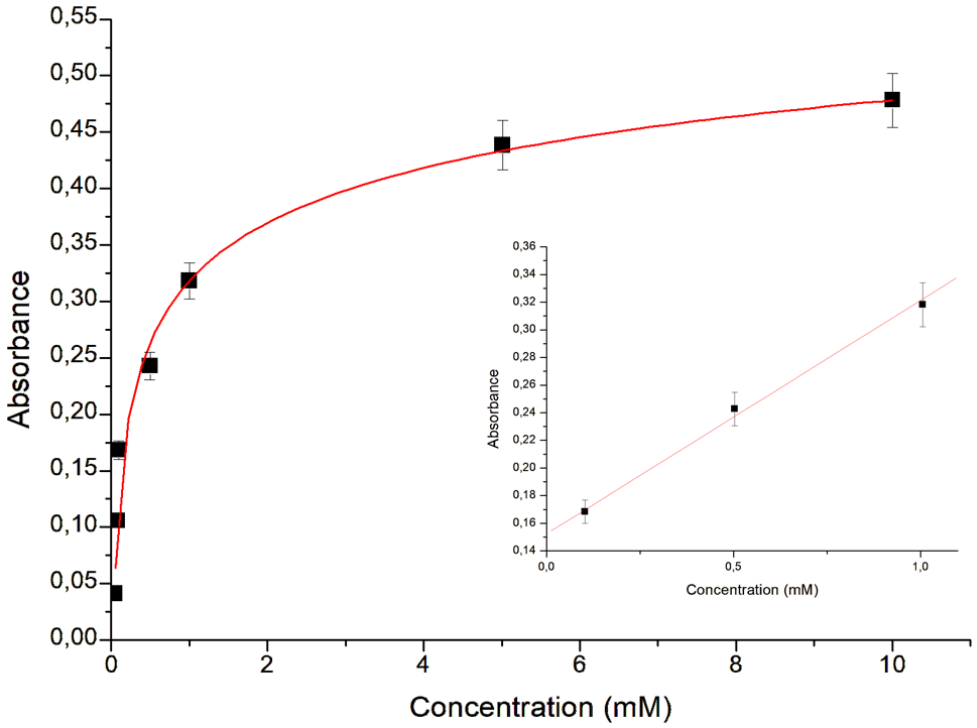

Figure 53. Values of absorption measurements at 400 nm obtained from a laccase solution (1 mg/mL in 0.1 M acetate buffer at pH 5) in the presence of different catechol concentrations and linearity range (inset).

According to the literature (Lepore, 2017), the data were described using the Michaelis and Menten kinetic model, i.e.,

$$v = \frac{v_{max}[S]}{K_M + [S]} \quad (4)$$

where v is the speed of the reaction (the speed of catechol oxidation catalysed by laccase), v_{max} is the maximum speed of the reaction, which is reached when all the enzyme is saturated with the substrate; [S] is the substrate concentration (in this case, the catechol) and K_m is the Michaelis Menten constant, which represents the substrate concentration at which the reaction speed is half the maximum speed (v_{max}).

The model assumes that, initially, the reaction speed increases with increasing substrate concentration, but subsequently, the speed stabilises and all active sites of the enzyme are occupied. By performing a non-linear fit, the following values of the parameters were obtained: V_{max} = 0.43 ± 0.03 Min^{-1}, K_m = 0.3 ± 0.1 mM. A value of V_{max}= 0.43 ± 0.03 Min^{-1} suggests that, at the saturation point of the reaction (i.e. when all the laccase is occupied by catechol), a certain absorbance maximum is reached, reflecting a certain amount of product (*o*-quinone).

K_m provides information on the affinity of the enzyme for the substrate; a low K_m value, as in our case, which equals 0.3 ± 0.1 mM, indicates that the enzyme has a good affinity for the substrate. The linearity range was found to be in the range of 0.1–1 mM, with a sensitivity of 0.16 ± 0.01 Min^{-1} mM^{-1}. These results agree with the previous report and boost the application of this approach by using solutions with a lower content of laccases, as also made by Lepore and Portaccio (Lepore 2017), which is crucial for realizing low-cost sensing approaches. Accordingly, time-course absorption measurements were carried out for an 8 µg/mL-laccase solution following the addition of catechol (at different concentrations). Absorption spectra of a laccase solution (8 µg/mL in 0.1 M acetate buffer pH 5) with added catechol at various concentrations (0.05 mM, 0.1 mM, 0.2 mM, and 0.4 mM) recorded at different times after the addition of catechol (0 min=t0, 3 min, 6 min, 9 min, 12 min, 18 min, 24 min and 30 min after the addition) are shown in Figure 54.

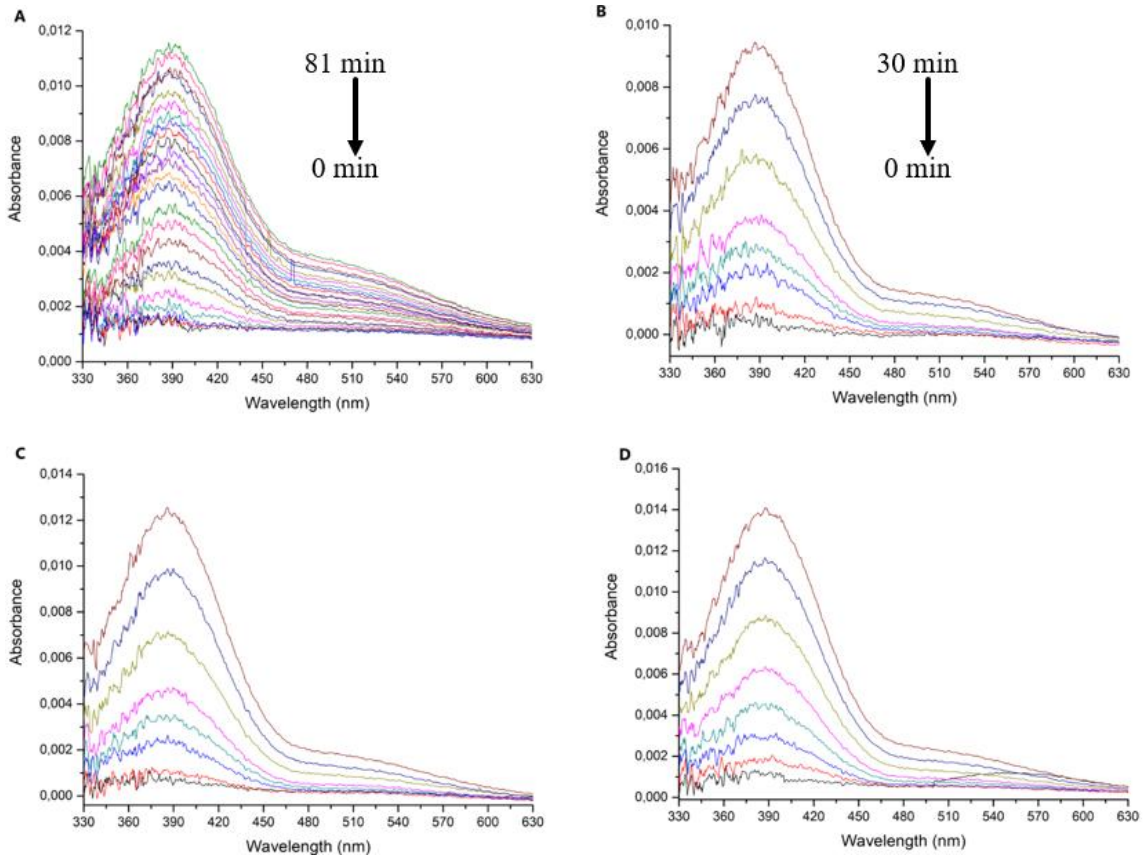

Figure 54. Absorption spectra of a solution of laccase and catechol ([laccase] = 8 µg/mL and [catechol] = 0.05 mM (**A**), 0.1 mM (**B**), 0.2 mM (**C**) and 0.4 mM (**D**)). Measurements were performed at various times: 0 min, 3 min, 6 min, 9 min, 12 min, 18 min, 24 min and 30 min after catechol addition.

For a catechol concentration of 0.05 mM, spectra were acquired up to 81 min after catechol addition since the absorbance intensity increased much more slowly than at higher concentrations (Figure 54A). Also in this case, the absorption spectra show an absorbance peak at around 400 nm, which is

typical of the *o*-quinone, the product of the oxidation reaction, as expected (Lepore, 2017; Dencheva, 2021).

The absorbance values at a fixed wavelength, as extracted from the spectra, are shown in Figure 55 as a function of catechol concentration, confirming the previously discussed results, including the linearity range.

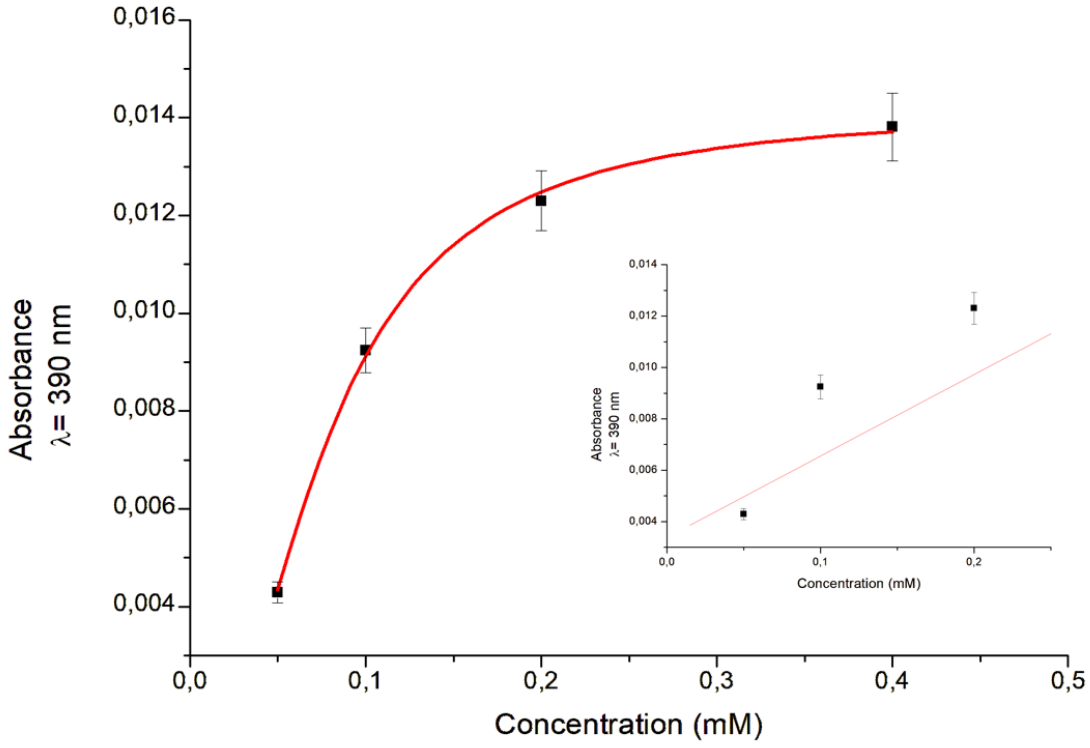

Figure 55. Absorbance values at a fixed wavelength (390 nm) of laccase solution (8 µg/mL in 0.1 M acetate buffer pH 5) after the addition of catechol as a function of catechol concentration, for a 30 min incubation time, and linearity range (inset).

The data were described using the Michaelis and Menten kinetic model, with a non-linear fit. The parameter values were obtained: V_{max} = 0.014 ± 0.003 Min^{-1}, K_m = 0.075 ± 0.003 mM. A low K_m value, resulting in 0.075 ± 0.003 mM, indicates that the enzyme has a good affinity for the substrate. The observed linearity range was 0.05–0.2mM, the slope of the line resulting in 0.0317 ± 0.0019 Min^{-1} mM^{-1}.

This confirms, on the one hand, that the proposed approach is applicable even when using a commercial laccase from *Trametes versicolor*. On the other hand, these findings are particularly relevant as they suggest the possibility of working with solutions containing a low concentration of laccase (8 µg/mL). These are crucial aspects for the potential large-scale implementation of this approach in sensing applications.

By absorbance measurements, a detectable catechol signal was obtained at 0.05 mM, which represents the minimum concentration recorded for this phenol in our study. Furthermore, the experimental investigation allowed us to better characterize the properties of the enzyme under study. These results are promising for broadening the range of applications of this enzyme in the detection of phenolic pollutants, particularly by exploiting the unique fluorescence emission properties of laccase.

6.1.2 Fluorescence measurements

6.1.2.1 Characterization of Laccase and catechol in solution

The fluorescence spectra of a solution of laccase from *Trametes versicolor* (1 mg/mL concentration in 0.1 M acetate buffer pH 5) as obtained in the UV region are shown in Figure 56 for two excitation wavelengths, one falling in the region of tyrosine and tryptophan excitation (excitation at 280 nm; Fig.56A) and in the other correspondence with the absorption due to the copper site T3 (320 nm; Fig. 56B). The emission spectra are characterized by broad bands featuring an emission maximum near 354 nm being observed when the shortest excitation wavelength is used. An emission maximum at around 420 nm is observed in the spectrum following an excitation at 320 nm, which is supposed to excite the T3 copper site (Cacciari, 2020). These results agree with the literature, where it is reported that the protein's fluorescence emission at the excitation wavelength of 280 nm is largely due to Trp residues being excited directly or by energy transfer from the excited state of Tyr (Lakowicz, 2006; Saoudi, 2017).

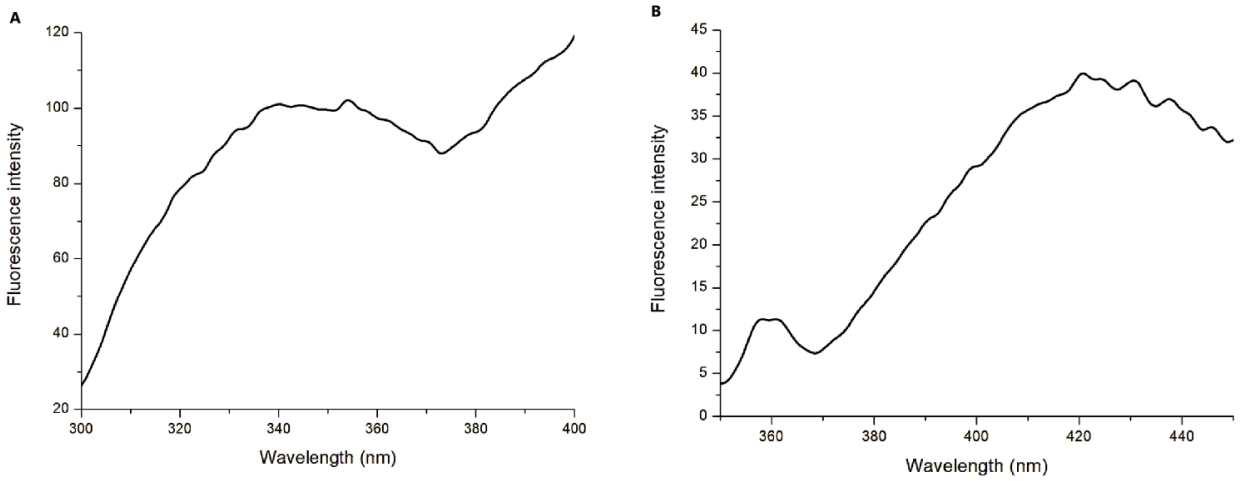

Figure 56. Emission spectra of a solution of laccase (concentration 1 mg/mL in 0.1 M acetate buffer at pH 5) following excitation at λexc= 280 nm (**A**) and λexc= 320 nm (**B**).

The possible fluorescence signal following the excitation of the T1-site absorption band at around 600 nm was also studied. Noteworthy, no fluorescence signal was obtained with a traditional spectrofluorometer, even with more concentrated laccase solutions, compared with those employed in UV fluorescence emission studies. A fluorescence spectrum (Figure 57) with excitation in the copper T1 region was obtained only when using a different experimental apparatus equipped with a He-Ne laser (632 nm) and a nitrogen-cooled CCD detector. This spectrum shows a maximum located at 697 nm. This result is particularly interesting because it is not present in the literature. The need to use a laser and a highly sensitive detector like the one used here (a liquid nitrogen-cooled CCD) confirms the low level of purity of the enzyme used. Still, it is encouraging since the T1 copper site is, as previously mentioned, the one most involved in the oxidation of the substrate. Therefore, this could be of interest for the development of laccase-based biosensors working in the visible range.

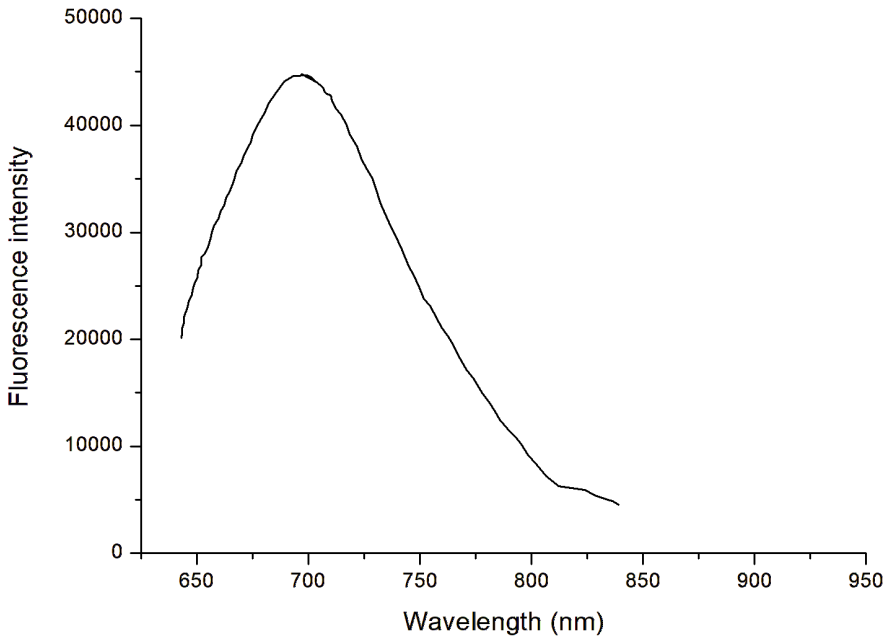

Figure 57. Emission spectrum of laccase from *Trametes versicolor* (0.5 mg/mL solution) in 0.1 M acetate buffer solution following excitation at 632 nm.

Figure 58 shows the fluorescence spectra for the catechol solution (0.4 mM in 0.1 M acetate buffer, pH 5) obtained by exciting the sample at 280 and 320 nm. Both spectra feature a clear band whose maximum is located at around 312 and 360 nm, respectively.

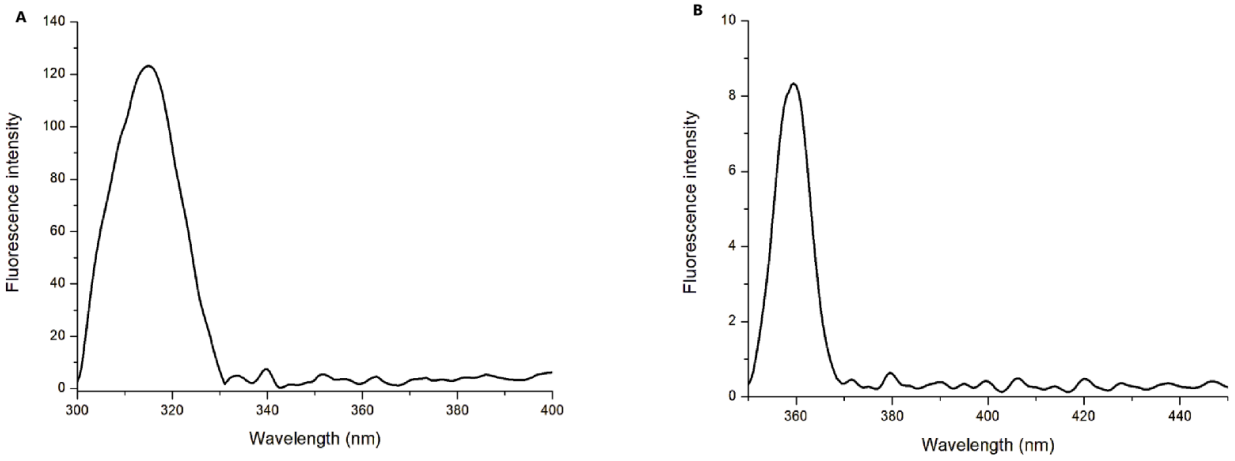

Figure 58. Emission spectra of catechol in solution (concentration of catechol 0.4 mM in 0.1 M acetate buffer at pH 5) following an excitation at λexc= 280 nm (panel A) and λexc= 320 nm (panel B).

6.1.2.2 Fluorescence emission measurements of solutions of laccase and catechol

According to the results of the absorption study and the preliminary characterization of the fluorescence emission of solutions of laccase and of catechol, an approach based on detecting changes in fluorescence emission of laccase in aqueous solution after interaction with catechol can be realized. Particular attention is here paid to the emission after excitation at 320 nm and 630 nm since the corresponding emission spectra are quite specific to laccase (we avoid using laccase fluorescence emission following an excitation around 280 nm that would excite fluorescence also of other molecules eventually present in real aqueous matrices of interest for on-site detection). As a starting system for analysing fluorescence, we used the laccase solution with the lowest content of the enzyme used for absorption measurements (i.e., 8 μg/mL concentration in 0.1 M acetate buffer pH 5). Accordingly, the fluorescence emission of laccase solutions in the presence of catechol was investigated. As the first step, the solution emission spectra at a fixed concentration of catechol (0.4 mM) following 320 nm excitation were measured at different times after phenol addition (incubation time), to analyze the characteristic time of the process. Representative spectra are shown in Figure 59 for different incubation times: 0 min, 5 min, 10 min, 50 min, and 80 min. All the spectra show a broad feature peaked at around 360 nm with a shoulder at 380 nm. A weak feature, peaked at 440 nm, is also present. The intensity of the observed features is dependent on the incubation time (time after catechol addition): an increase in the fluorescence signal with incubation time is evident, especially in the 350-420 nm range.

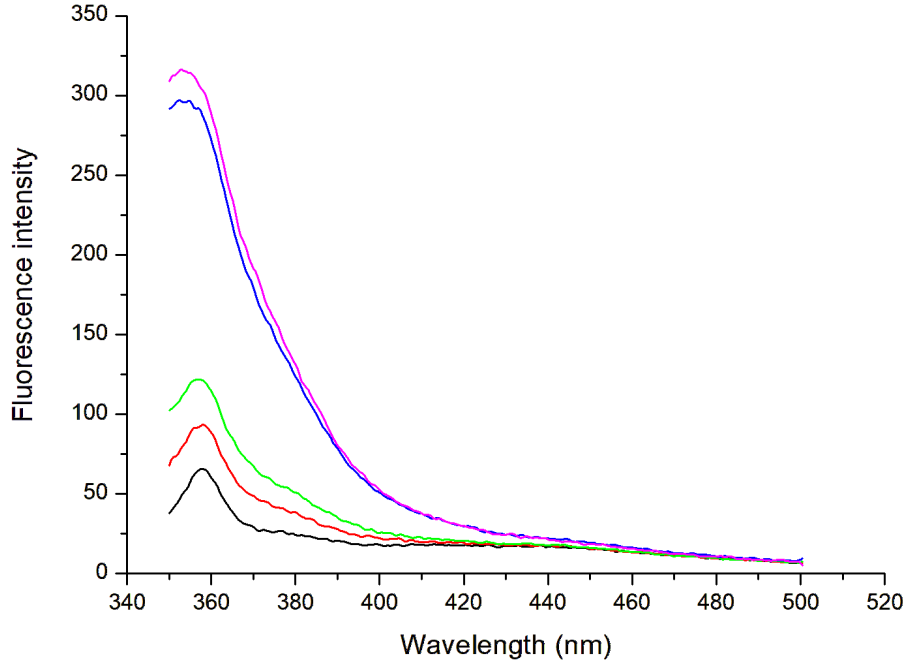

Figure 59. Emission spectrum of laccase solution (8 µg/mL concentration in 0.1 M acetate buffer pH 5) and fixed catechol concentration (0.4 mM in 0.1 M acetate buffer pH 5). Measurements were performed at various times: 0 min (black line), 5 min (red line), 10 min (green line), 50 min (blue line) and 80 min (purple line) after catechol addition. Experimental conditions: spectra were acquired with excitation and emission slits fixed at 5 nm.

To study the characteristics of this behaviour, related to the characteristics of the oxidation reaction between laccase and catechol, the change in fluorescence intensity of the peak at 360 nm (associated with the reaction product, the corresponding *o*-quinone) was analysed for an observation time interval lasting up to 60 min, following the addition of increasing catechol concentrations, in the range of interest (0.05 mM, 0.1 mM, 0.2 mM and 0.4 mM in 0.1 M acetate buffer at pH 5). The results are shown in Figs. 60A-D, which confirms that the emission increases with time, reaching a constant value over the time interval studied, only for the highest concentration of catechol.

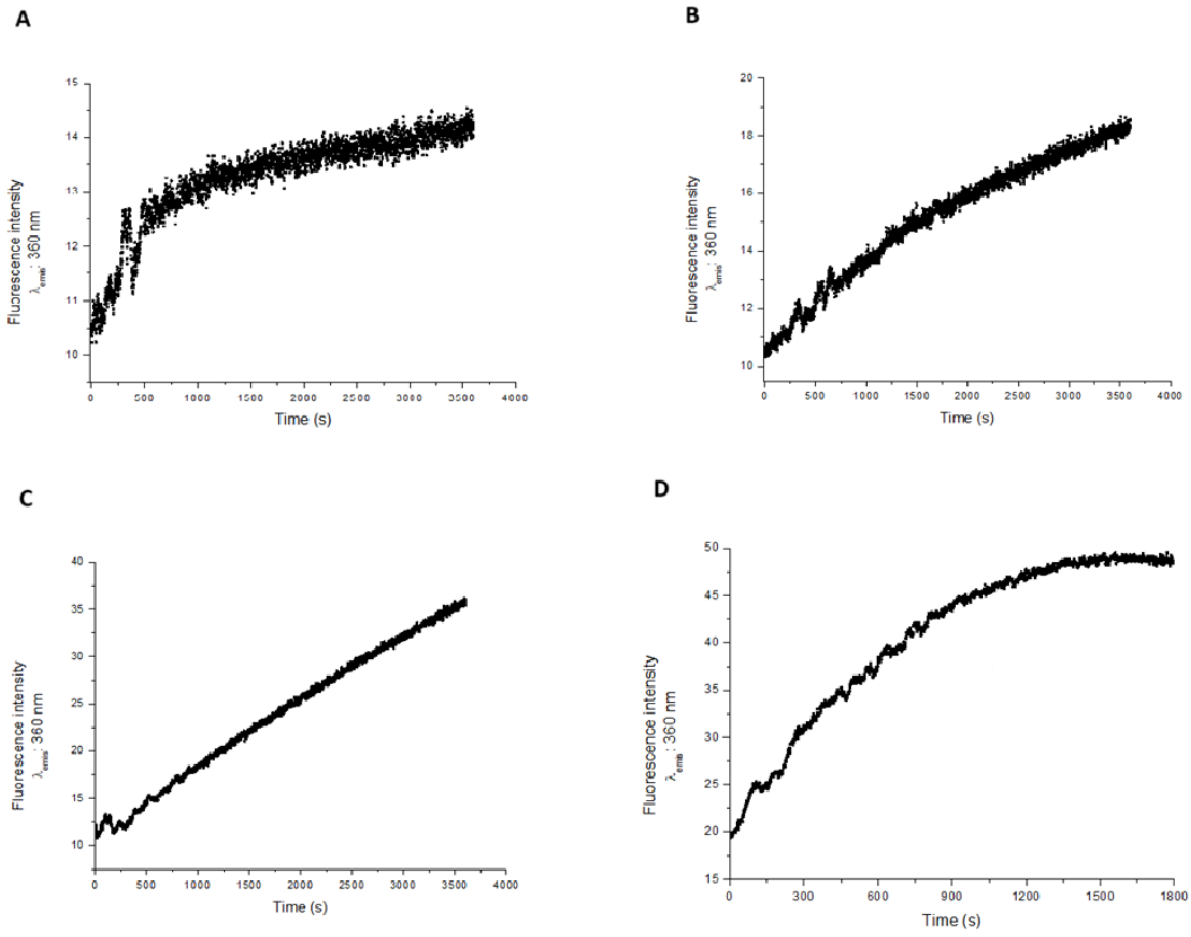

Figure 60. Emission spectra of a solution of laccase and catechol ([laccase] = 8 µg/mL and [catechol] = 0.05 mM (**A**), 0.1 mM (**B**), 0.2 mM (**C**) and 0.4 mM (**D**)). Measurements were performed at different times, up to 60 min after catechol addition, with λexc= 320 nm.

The analysis of the emission vs time curves allows one to consider that a proper incubation time for a catechol-detection system is 30 minutes. By using the results of the time course measurements, an analytical parameter defined as the changes per unit of time in the fluorescence emission at 360 nm (F_{360nm}) can be obtained by using the following expression

$$\Delta Ft = \frac{F_{360nm}\,(t) - F_{360nm}\,(t0)}{t - t0} \qquad (5)$$

where $F_{360nm}\,(t)$ is the fluorescence emission detected at λ=360 nm at the time t=30min, $F_{360nm}\,(t0)$ is the same calculated at the time t0, i.e., the initial time of the time course measurement. The so obtained values of the ΔFt parameter are reported in Figure 61 as a function of the catechol concentration; they show a clear linear dependence of the selected

parameter on the catechol concentration in the investigated range.

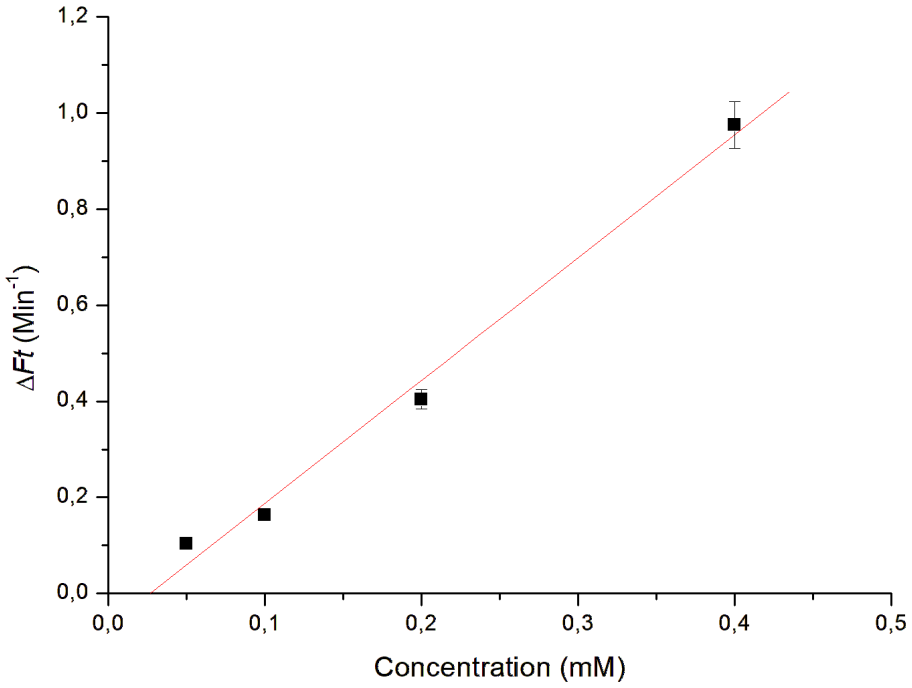

Figure 61. Values of the ΔFt parameter as a function of catechol concentration with the resulting linear fitted curve (red line). Parameter of the linear fit ΔFt =a+b*[Catechol]: a=-0.07±0.04 min^{-1}, b=2.56±0.18 min^{-1} mM^{-1}, r=Pearson's linear correlation coefficient=0.995.

The fluorescence emission of the laccase solution, following excitation resonant with the T1 site (λexc = 632 nm using a laser beam), has also been used to study the potential of this fluorescence-based catechol detection scheme.

The fluorescence emission detected at 700 nm as a function of the catechol concentration is shown in Figure 62, witnessing variations sensitive in response to varying concentrations of catechol.

The data were described using the Michaelis and Menten kinetic model, with a non-linear fit. The following parameter values were obtained: $V_{max} = (249 \pm 11) \cdot 10$ Min^{-1}, $K_m = 31 \pm 2$ µM. K_m provides information about the affinity of the enzyme for the substrate; in our case, a high value of K_m suggests that the enzyme does not have a good affinity for the substrate. This result appears to contrast with absorption measurements, which indicated a favourable interaction between laccase and catechol. However, this discrepancy can be attributed to differences in experimental conditions: the absorption experiments were conducted at higher enzyme and substrate concentrations compared to fluorescence-based kinetic assays. The higher concentrations used in the absorbance setup may have

enhanced apparent binding signals, while the fluorescence-based kinetic analysis, performed at lower substrate concentrations, more accurately reflects the enzyme's catalytic efficiency and affinity under dilute conditions. This highlights how the observed interaction strength can vary depending on the technique and concentration regime applied.

The linearity range was 0.1–50 μM, with a sensitivity of 49 ± 10 Min^{-1} μM^{-1}.

Due to the difficulty in reproducibility of the measurements, further efforts must therefore be made to improve the acquisition conditions by exploiting the emission of the T1 Cu site of laccase, but it appears possible to design a fluorescence-based sensing scheme for detecting catechol.

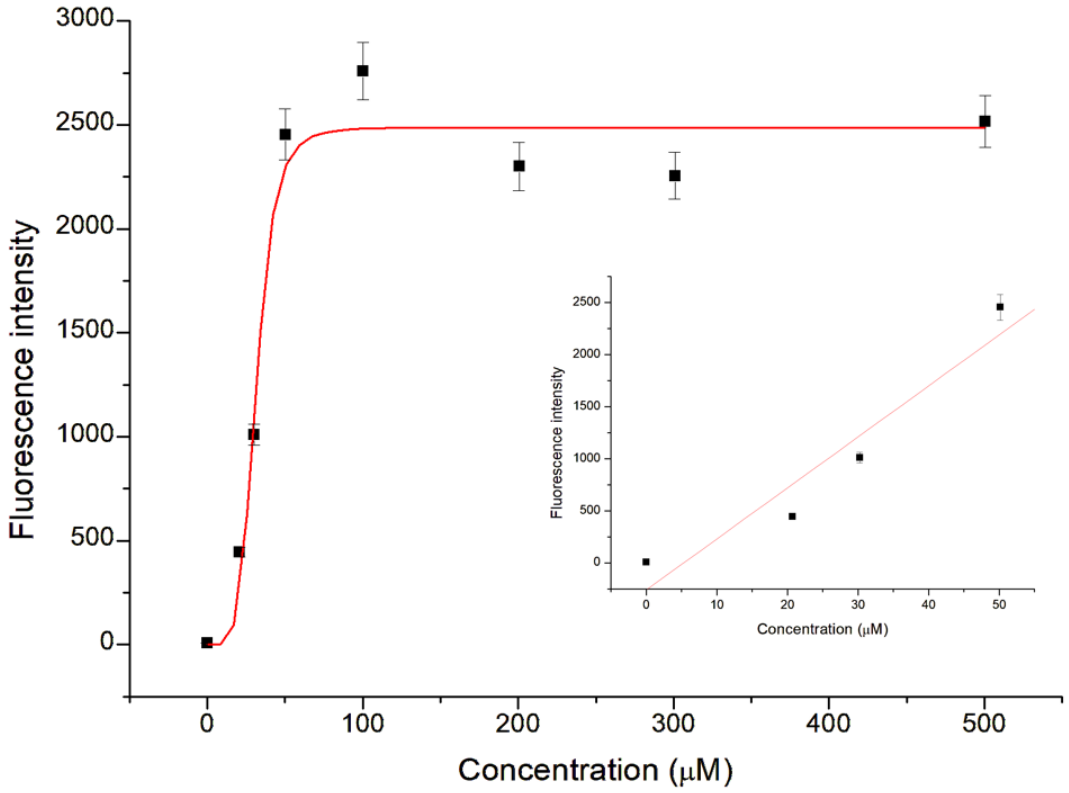

Figure 62. Fluorescence emission at 700 nm as detected from a solution of laccase from *Trametes versicolor* (0.5 mg/mL solution in 0.1 M acetate buffer) following excitation at 632 nm in the presence of different concentrations of catechol, and linearity range (inset).

The results highlight the potential of fluorescence spectroscopy for the development of optical biosensors for catechol detection, using laccase as the biological element. Fluorescence measurements performed with an excitation wavelength of 320 nm enabled the detection of a catechol signal at a concentration of 0.05 mM, which currently represents the lowest concentration achieved for this phenol under the studied conditions. Alternatively, by exploiting the intrinsic fluorescence emission of the laccase solution upon resonant excitation of the T1 copper site (λexc= 632 nm), it was possible to detect the catechol signal at concentrations as low as 0.1 μM. A key aspect of

fluorescence-based systems is the optimisation of incubation time, which plays a critical role in enhancing detection performance and ensuring reproducibility. These optical biosensors also have the potential to be low-cost and user-friendly, making them attractive for practical applications.

6.2 SERS-based sensing approach for catechol detection

The effectiveness of a SERS-based detection system is strongly influenced by the nature of the substrate, which governs both the enhancement factor and the reproducibility of the measurements. Numerous commercial SERS substrates are currently available, incorporating customised nanostructures and surface patterns designed to maximise signal enhancement. These products have different characteristics, leading to a wide range of analytical performance (Liu, 2020; Rahmani, 2023). Recently, SERS has also been employed in the development of detection strategies for phenolic compounds, as discussed in section *3.2.3*.

In this framework, we aimed to understand the potential of an easily made and cost-effective SERS-based sensing system for catechol detection in aqueous matrices. The goal was to obtain a cost advantage, being compatible in concentration with that already present in the literature (Barveen, 2022; Pan, 2018). At this aim, we evaluated and examined the properties of some commercial SERS substrates (described in paragraph *5.2.1.2*, with characteristics summarized in Table 4), a home-made substrate (details in paragraph *5.2.1.3*) and tested their performance for detecting catechol, whose Raman spectral features were preliminarily identified.

6.2.1 Characterization of Raman features of catechol

As a first step, Raman measurements of catechol in an aqueous solution (at a concentration of 180 mM in distilled water) were performed at different laser excitation wavelengths (405 nm, 532 nm, 633 nm and 785 nm) to investigate the best experimental conditions for Raman signal detection. Representative spectra are shown in Figure 63. Clear peaks are observed in all cases, even if a lower number of features is observed when the 785-nm laser is used (Fig. 63D). The most evident bands observed when 405, 532, and 633-nm lasers are used are those located at 775 and 1032 cm^{-1} and assigned to the in-plane and out-of-plane C-H deformations, bands at 1167 cm^{-1} associated with the phenolic C-C stretching mode, at 1274 cm^{-1}, attributed to the phenolic C-O stretching mode, and at 1603 cm^{-1}, attributed to C=C stretching mode. The observed peaks are summarized in Table 5 along with their assignment. These results confirm that catechol has well-defined Raman bands, consistent with those reported in the literature (Sanchez-Cortes, 2000; Barveen, 2022; Pan, 2018).

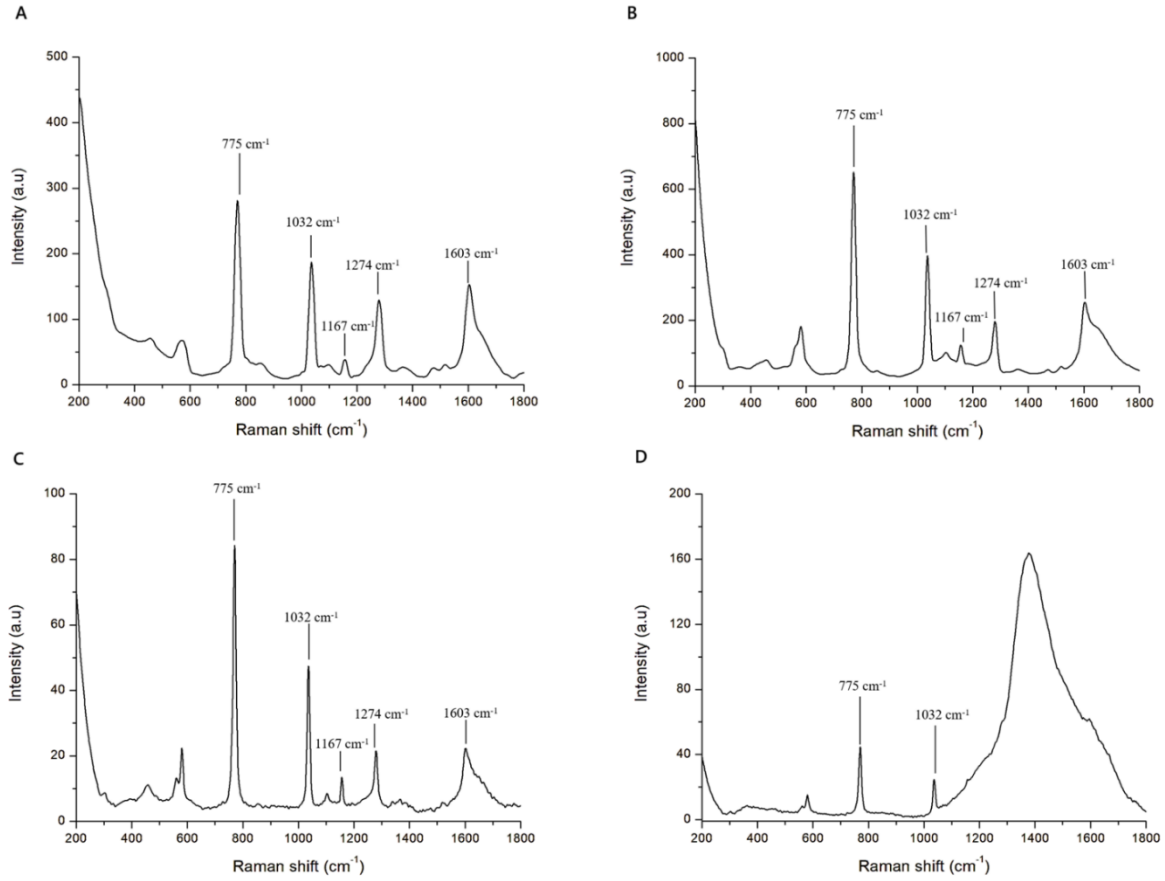

Figure 63. Raman spectra of catechol solution (concentration = 180 mM) were acquired with the 405 (**A**), 532 (**B**), 633 (**C**) and 785 nm (**D**) laser lines; optical objective employed during measurements: x50 (for 532 and 785 nm excitation wavelengths) and x100 (for 405 and 633 nm excitation wavelengths).

Raman peaks (cm^{-1})	**Assignment**
775	Out-of-plane C–H deformations
1032	In-plane C–H deformations
1167	C-C stretching mode
1274	C–O stretching mode
1603	C=C stretching mode

Table 5. Characteristic Raman bands of catechol with their tentative assignment (Sanchez-Cortes, 2000).

Raman spectra were also recorded from catechol solutions with concentrations lower than 180 mM to understand the concentration limit for observing the Raman signal in aqueous catechol solutions. A catechol concentration of around a few mM was the lowest for observing the Raman signal from an aqueous solution, as discussed in the following.

The results confirm that catechol has clear features that cannot be easily observed under some mM that can be usefully employed in SERS-based detection schemes.

6.2.2 Evaluation of commercial substrate potential for detecting catechol

Aiming at finding the best substrate for realizing the SERS-based detection scheme for catechol, we compared the detection performance of five commercial SERS substrates: RAM-SERS-Au and RAM-SERS-Ag manufactured by Ocean Insight, Gold SERStrate and Silver SERStrate supplied by Silmeco ApS and Premium-AgAu SERS substrates manufactured by SERSitive; the substrates were described in paragraph *5.2.1.2*, and their characteristics are summarized in Table 4.

All substrates were initially tested by first acquiring the spectrum of the bare substrate and then the spectrum of catechol solutions at relatively high concentrations (tenths of mM). This preliminary data was used to establish the experimental conditions for further tests aimed at evaluating the substrate's performance. Specifically, we assessed the lowest catechol concentration at which a clear SERS signal could be detected, the repeatability of the measurements, and the background noise level.

The first substrates we tested were those produced by Ocean Insight® (RAM SERS-Au and RAM SERS-Ag), with polymer fibers covered inhomogeneously with gold or silver nanoparticles. To characterize the observable spectral features of catechol, a higher phenol concentration (70 mM) was used as the starting point. The signal was recorded immediately after immersing the substrates in the catechol solution (to avoid evaporation of the solution), with laser power and acquisition time carefully adjusted to prevent damage to the substrate surface while maximizing the signal-to-noise ratio (Rahmani, 2023). A representative SERS spectrum of the 70 mM catechol solution on the RAM-SERS-Au substrate is shown in Figure 64.

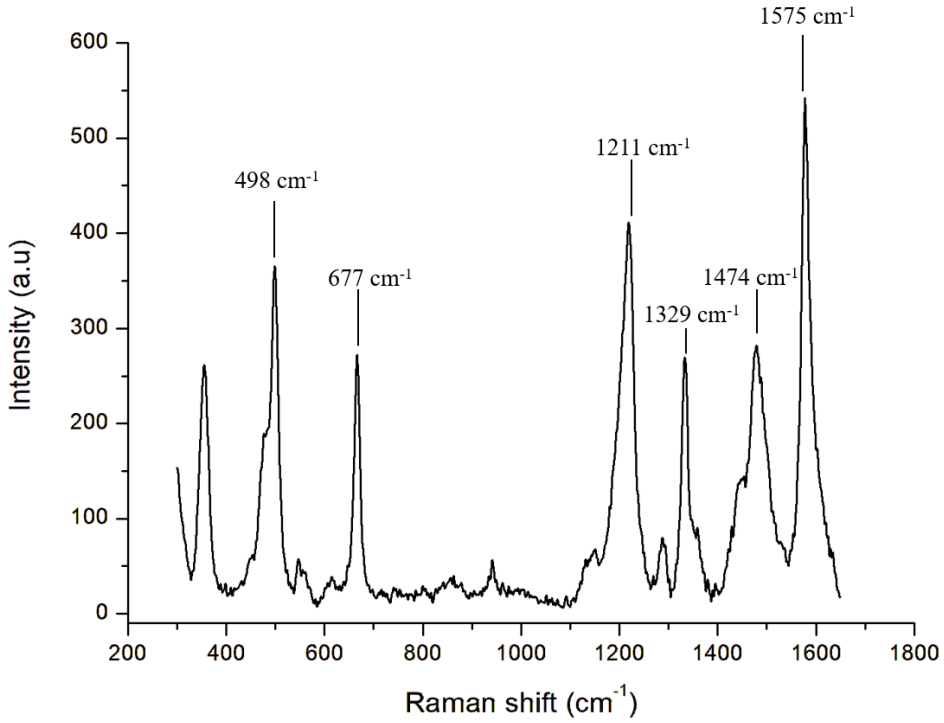

Figure 64. SERS spectrum of a catechol solution (concentration = 70 mM) on RAM-SERS-Au substrate. Experimental conditions: 785 nm excitation wavelength, 10x optical objective, OD equal to 1 (reduces the light intensity by a factor of 10), so the laser power on the sample is 8.6 mW, and 0.5 s acquisition time.

Clear peaks can be observed in the spectrum, with the disappearance of the out-of-plane and in-plane C–H deformations (at 775 cm^{-1} and 1032 cm^{-1}, respectively) along with a shift of the C=C stretching mode observed from 1603 cm^{-1} in the Raman spectrum to 1575 cm^{-1} in the SERS spectra. The appearance of the above-discussed bands at 498 cm^{-1}, 677 cm^{-1}, 1211 cm^{-1}, 1329 cm^{-1} and 1474 cm^{-1} agrees with previous reports (Barveen, 2022; Pan, 2018), and are summarised in Table 6, with their respective assignments. Shifts in vibrational frequencies and the disappearance of certain Raman-active modes suggest molecular reorientation or specific interactions with the metallic SERS substrate. SERS-specific peaks such as those at 498 and 677 cm^{-1} provide additional fingerprints useful for sensitive detection.

Raman peaks (cm^{-1})	Assignment
498	skeletal mode
677	C-O bending mode
1211	C-O stretching mode
1329	C-H bending mode
1474	C-O stretching mode
1575	C=C stretching mode

Table 6. Characteristic Raman peaks of catechol with their tentative assignment (Barveen, 2022; Sanchez-Cortes, 2000).

The same analysis was carried out on the other substrate selected by Ocean Optics, namely, RAM-SERS-Ag, optimised for use with the 532 nm laser (Figure 65). Also, in this case, we analysed the spectra collected immediately after immersing the substrate in the container with the catechol solution (70 mM). It is possible to observe the presence of the bands at 498 cm^{-1}, 1211 cm^{-1}, 1329 cm^{-1}, 1474 cm^{-1} and 1575 cm^{-1}, in agreement with the SERS spectrum obtained using the RAM-SERS-Au substrate (peak assignments are reported in Table 6). The most visible difference from the spectra obtained using the RAM-SERS-Au substrate is the absence of the signal at 677 cm^{-1}, which is associated with the C-O bending mode.

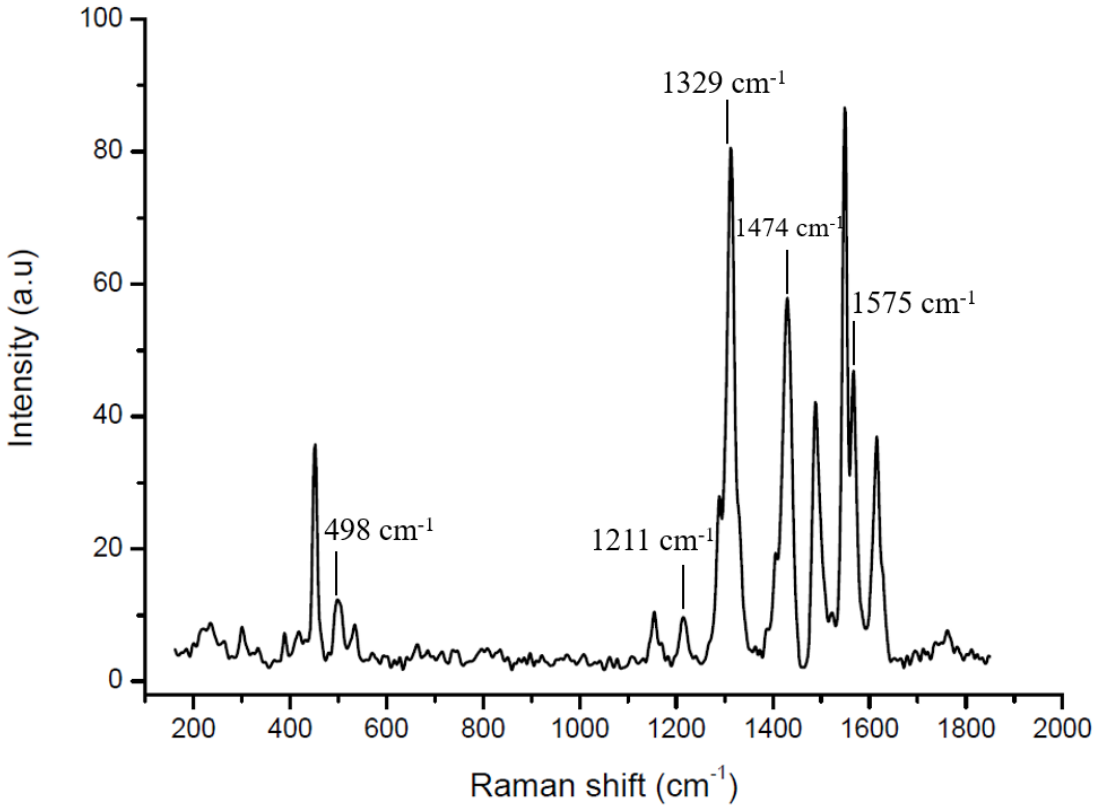

Figure 65. SERS spectrum of catechol solution (concentration =70 mM) on RAM-SERS-Ag substrate. Experimental conditions: 532 nm excitation wavelength, 10x optical objective, OD equal to 3 (reduces the light intensity by a factor of 1000), so the laser power on the sample is 0.08 mW, and 2s acquisition time.

In conclusion, these substrates supplied by Ocean Insight do not appear to be effective for enhancing the Raman signal of catechol at lower concentrations.

We analysed three other commercial SERS substrates: Gold SERStrate and Silver SERStrate supplied by Silmeco ApS, and Premium-AgAu SERS substrates produced by SERSitive (with characteristics summarised in the table). The Gold-SERStrate and Silver-SERStrate substrates consist of gold/silver-coated silicon nanopillars, and the Premium-AgAu substrates are made with a mixture of silver and gold nanoparticles deposited on an indium tin oxide (ITO) glass surface.

Initially, to characterize the background Raman signal provided by each substrate, some spectra were acquired from randomly distributed points on each substrate surface, using two lasers providing different excitation wavelengths, namely 532 and 785 nm.

With both laser excitations, all spectra present some clear features that can be observed in the 200-1800 cm^{-1} range, as shown in Figure 66.

For the Silver SERStrate substrate, the intense band around 520 cm^{-1} can be assigned to the Si substrate, to support the SERS active layer, with a 532 nm laser line (Figure 66A, red line). For the

Premium AgAu substrates, at both excitation wavelengths, a strong band at 236 cm^{-1} was observed, which is hypothesized to be associated with the binding of the nanoparticles to the indium tin oxide (ITO) glass surface (Figure 66, black line). For all substrates, such blank spectra may limit the observation of the molecules, as their Raman signal should be well above the blank intensity to be detectable. To compare the performance of different substrates, we performed systematic studies to detect the presence of catechol by changing the excitation laser wavelength (Liu, 2020).

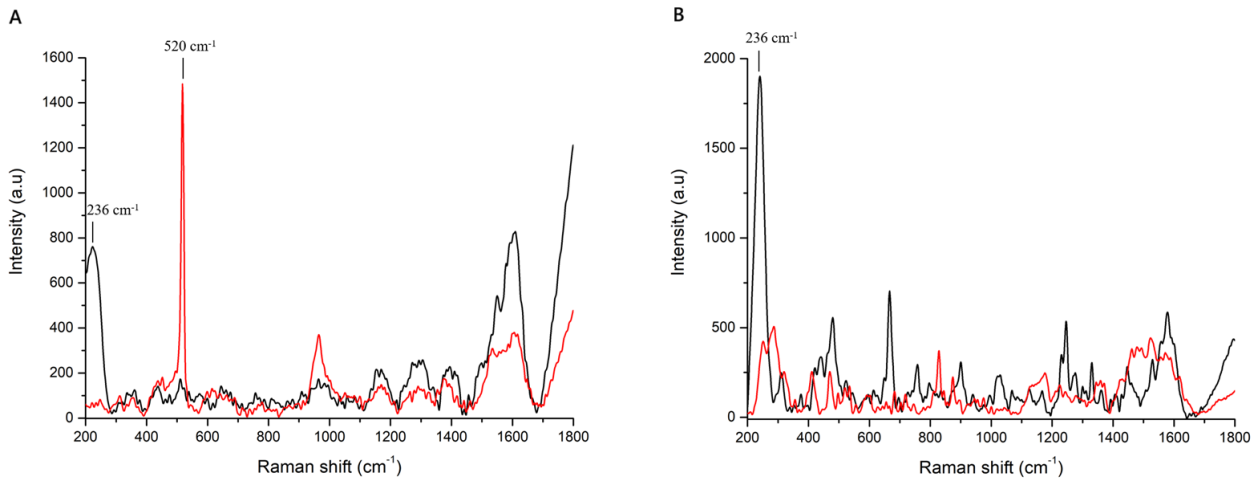

Figure 66. A) Raman spectra of Premium AgAu (black line) and Silver-SERStrate (red line) substrates for 532 nm excitation laser; (**B**) Raman spectra of Premium AgAu (black line) and Gold-SERStrate (red line) substrates for 785 nm excitation laser. Experimental conditions: 50x optical objective, OD equal to 0.3 (reduces the light intensity by 50%), so the laser power on the sample is 8.5 mW, with a 532 nm laser line, and 28.5 mW with a 785 nm laser line; 2s acquisition time and 4 accumulations.

We then studied the SERS signal of the Gold SERStrate, Silver SERStrate and Premium-AgAu substrates after depositing a few microliters of a catechol solution at a concentration of 7 mM (Figure 67). The acquisition time was adjusted to avoid damaging the sample surface and to maximise the signal-to-noise ratio (Liu, 2020; Rahmani, 2023). Distinct Raman bands corresponding to the signature of the catechol molecules can be observed.

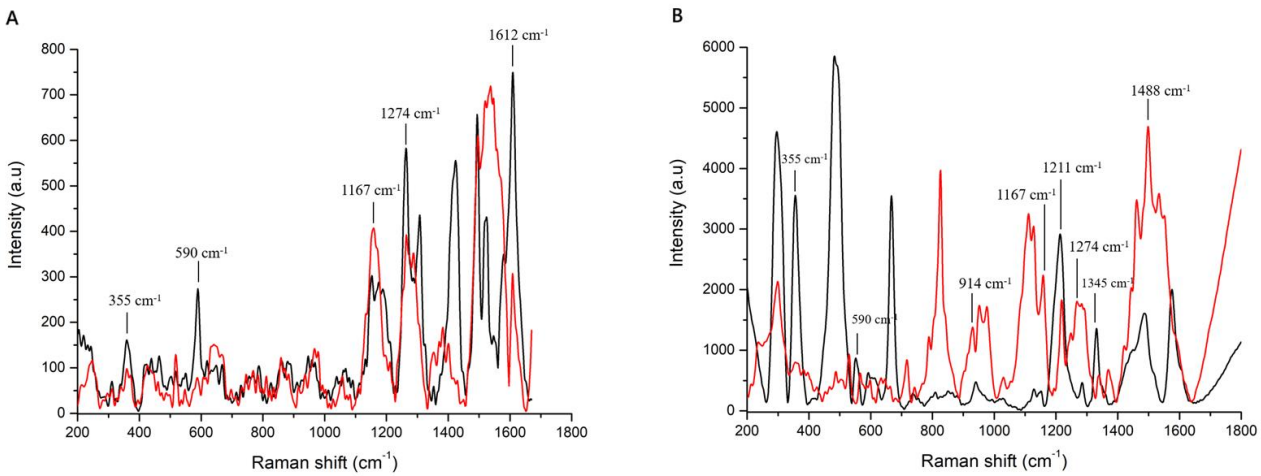

Figure 67. SERS spectra of catechol solution at 7 mM with **A**) Premium AgAu (black line) and Silver-SERStrate (red line) substrates (excitation wavelength at 532 nm); **B**) Premium AgAu (black line) and Gold-SERStrate (red line) substrates (excitation wavelength at 785 nm). Experimental conditions: 2s acquisition time, 4 accumulations, 50x optical objective, and OD equal to 0.3 (reduces the light intensity by 50%), so the laser power on the sample is 8.5 mW, with a 532 nm laser line, and 28.5 mW with a 785 nm laser line.

For the 532 nm laser with Silver SERStrate and Premium-AgAu substrates, it is possible to observe the catechol signal at 355 cm^{-1}, 1167 cm^{-1}, 1274 cm^{-1} and 1612 cm^{-1}, attributed to C-O bending mode, C-C stretching mode, C-O stretching mode and C=C stretching mode, respectively (Figure 67A). In the case of the Premium AgAu substrate, a band at 590 cm^{-1}, associated with the C-O bending mode, is visible (Fig. 67A, black line).

With Gold-SERStrate and Premium-AgAu, at an excitation wavelength of 785 nm, peaks appear at 355 cm^{-1}, 914 cm^{-1}, 1211, 1274 cm^{-1}, 1345 cm^{-1} and 1488 cm^{-1} (which with the Gold-SERStrate substrate seems to be shifted by a few Raman to ~1494 cm^{-1}), assigned to the C-O bending mode, to the radial vibration of the ring skeleton, to the C-O stretching mode, to the C-H bending mode and C-O stretching between two hydroxyl carbon atoms, respectively (Fig. 67B). The difference between the substrates produced by Silmeco and SERSitive, at an excitation wavelength of 785 nm, is the presence of distinct catechol-related peaks at 590 cm^{-1} for the Premium AgAu substrate (Fig. 67B, black line). With the Gold-SERStrate substrate, the band at 1167 cm^{-1}, associated with the C-C stretching mode of phenol, is evident (Figure 67B, red line).

The peaks observed using both laser lines and their tentative assignment are shown in Table 7.

Raman peaks (cm^{-1})	Assignment
355	C-O bending mode
590	C-O bending mode
914	radial vibration of the ring skeleton
1167	C-C stretching mode
1211	C-O stretching mode
1274	C-O stretching mode
1345	C-H bending mode
1488	C-O stretching mode
1612	C=C stretching mode

Table 7. Characteristic Raman peaks of catechol (7 mM) observed by using commercial substrates (Silver-SERStrate, Gold-SERStrate and Premium- AgAu), optimised at 532 and 785 excitation wavelengths, and their tentative assignment (Barveen, 2022; Sanchez-Cortes, 2000).

Since the main characteristic catechol peaks are detected at 7 mM for all substrates, we studied the SERS signal using various catechol concentrations lower than 7 mM (0.1, 0.5 and 1 mM) to assess the best substrate for catechol detection (Figure 68). For the 532 nm laser with Silver-SERStrate and Premium-AgAu substrates, the visible signal for both commercial substrates at low catechol concentrations is at 1274 cm^{-1}, assigned to the C-O stretching mode (Fig. 68). By analysing the intensity of this peak as a function of catechol concentration for both substrates (shown as an inset in the corresponding panel of Fig.68), a linearity range between 0.1 and 7 mM is observed, with a sensitivity of 80±14 mM^{-1}, and 120±20 mM^{-1} for Silver-SERStrate and Premium-AgAu, respectively.

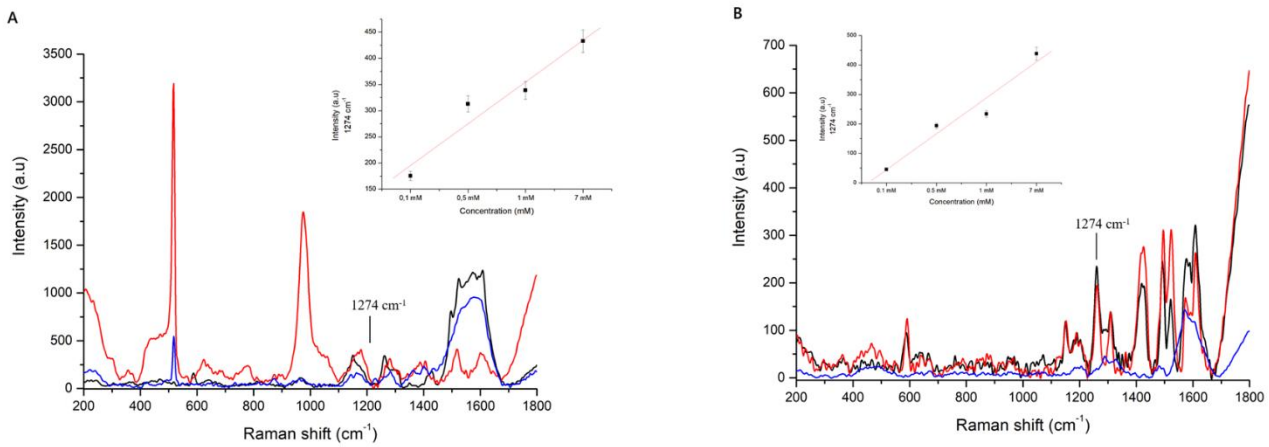

Figure 68. SERS spectra of catechol solution at 0.1 mM (blue line), 0.5 mM (red line) and 1 mM (black line) concentrations with Silver-SERStrate (**A**) and Premium-AgAu (**B**) substrates at 532 nm excitation wavelength. Linearity range for the intensity of the peak at 1274 cm^{-1} (inset). Experimental conditions: 2s acquisition time, 4 accumulations, 50x optical objective, and OD equal to 0.3 (reduces the light intensity by 50%), so the laser power on the sample is 8.5 mW, with a 532 nm laser line. For Silver-SERStrate substrate (**A**), linearity range for the intensity of the peak at 1274 cm^{-1} (linear fitting parameters: a= [11 ± 4] ·10 a.u., b= 80 ± 14 a.u./mM; r= 0.968). For Premium-AgAu substrate (**B**), linearity range for the intensity of the peak at 1274 cm^{-1} (linear fitting parameters: a= [-8 ± 6] ·10 a.u., b= [12 ± 2] ·10 a.u./mM; r= 0.971).

As witnessed in the spectra shown in Figure 69, when the 785 nm laser is used with Gold-SERStrate substrate, the visible signals at low catechol concentrations are at 914 cm^{-1} and 1274 cm^{-1}, attributed to the radial vibration of the ring skeleton and the C-O stretching mode, respectively. By analysing the intensity of these peaks as a function of catechol concentration (shown as inset in the corresponding panel of Fig.69), a linearity range between 0.1 and 7 mM is observed, with a sensitivity of (33 ± 7) 10 mM^{-1} and (48 ± 13) 10 mM^{-1} for 914-cm^{-1} and 1274-cm^{-1} peak intensity, respectively.

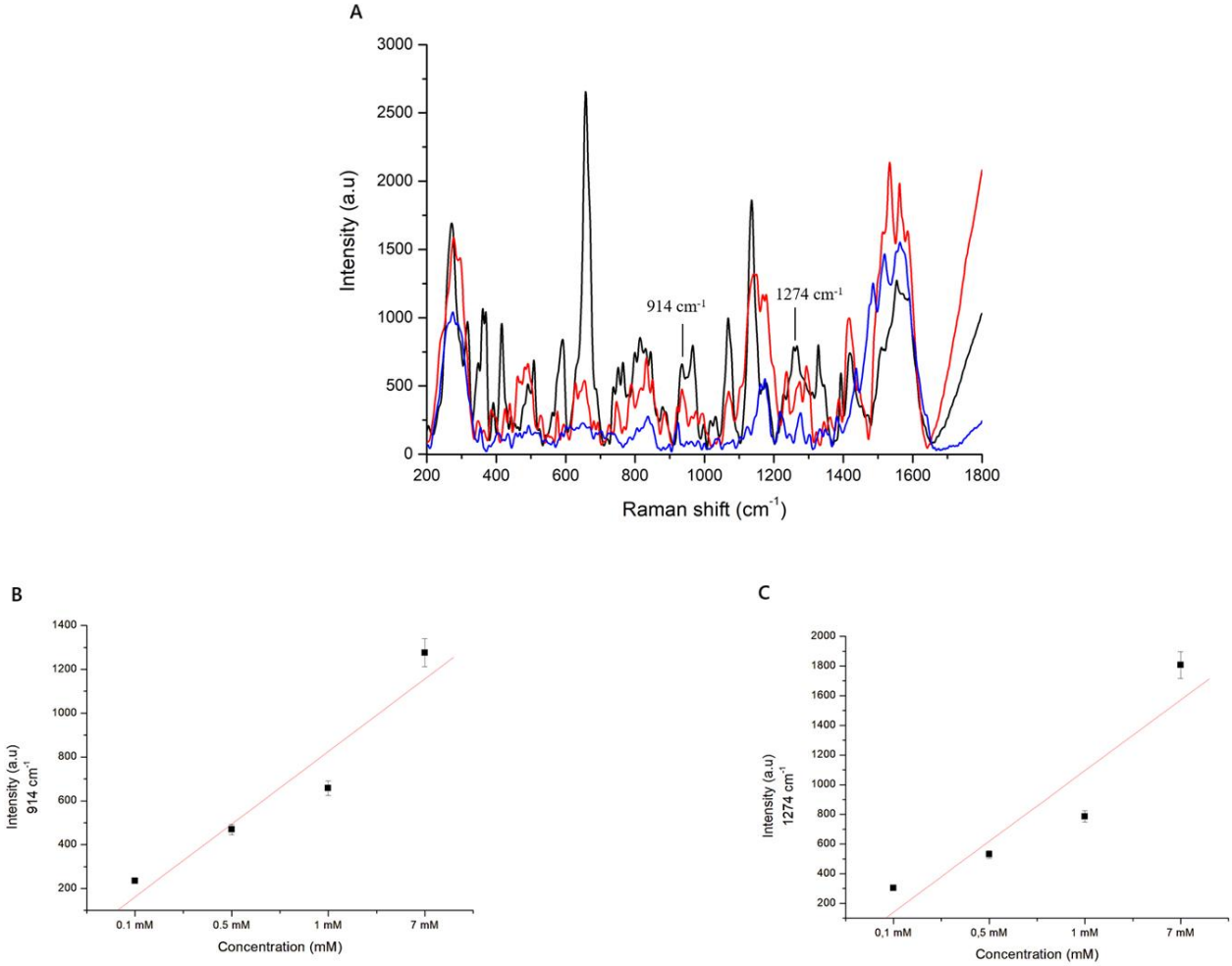

Figure 69. A) SERS spectrum of catechol solution at 0.1 mM (blue line), 0.5 mM (red line) and 1 mM (black line) concentrations with Gold-SERStrate substrate at 785 nm excitation wavelength. Experimental conditions: 2s acquisition time, 4 accumulations, 50x optical objective, and OD equal to 0.3 (reduces the light intensity by 50%), so the laser power on the sample is 28.5 mW, with a 785 nm laser line. **B**) linearity range for the intensity of the peak at 914 cm^{-1} (linear fitting parameters: a= [-2 ± 2] ·10^2 a.u., b= [33 ± 7] ·10 a.u./mM; r= 0.958), and **C**) at 1274 cm^{-1} (a= [-3 ± 4] ·10^2 a.u., b= [5 ± 1] ·10^2 a.u./mM; r= 0.927).

SERS catechol spectra obtained using excitation with the 785 nm laser and Premium-AgAu substrate are shown in Figure 70 for the three low phenol concentrations (0.1, 0.5 and 1 mM). In these spectra, the visible signals are observed at 355 cm^{-1} and 1488 cm^{-1}, assigned to the C-O bending mode and C-O stretching mode, respectively. By analysing the intensity of these peaks as a function of catechol concentration (shown as inset in the corresponding panel of Fig.70), a linearity range for catechol concentrations between 0.1 and 7 mM was observed, with a sensitivity of (55 ± 8) 10 mM^{-1} and 420 ± 30 mM^{-1} for 355 cm^{-1} and 1488 cm^{-1} peak intensity, respectively.

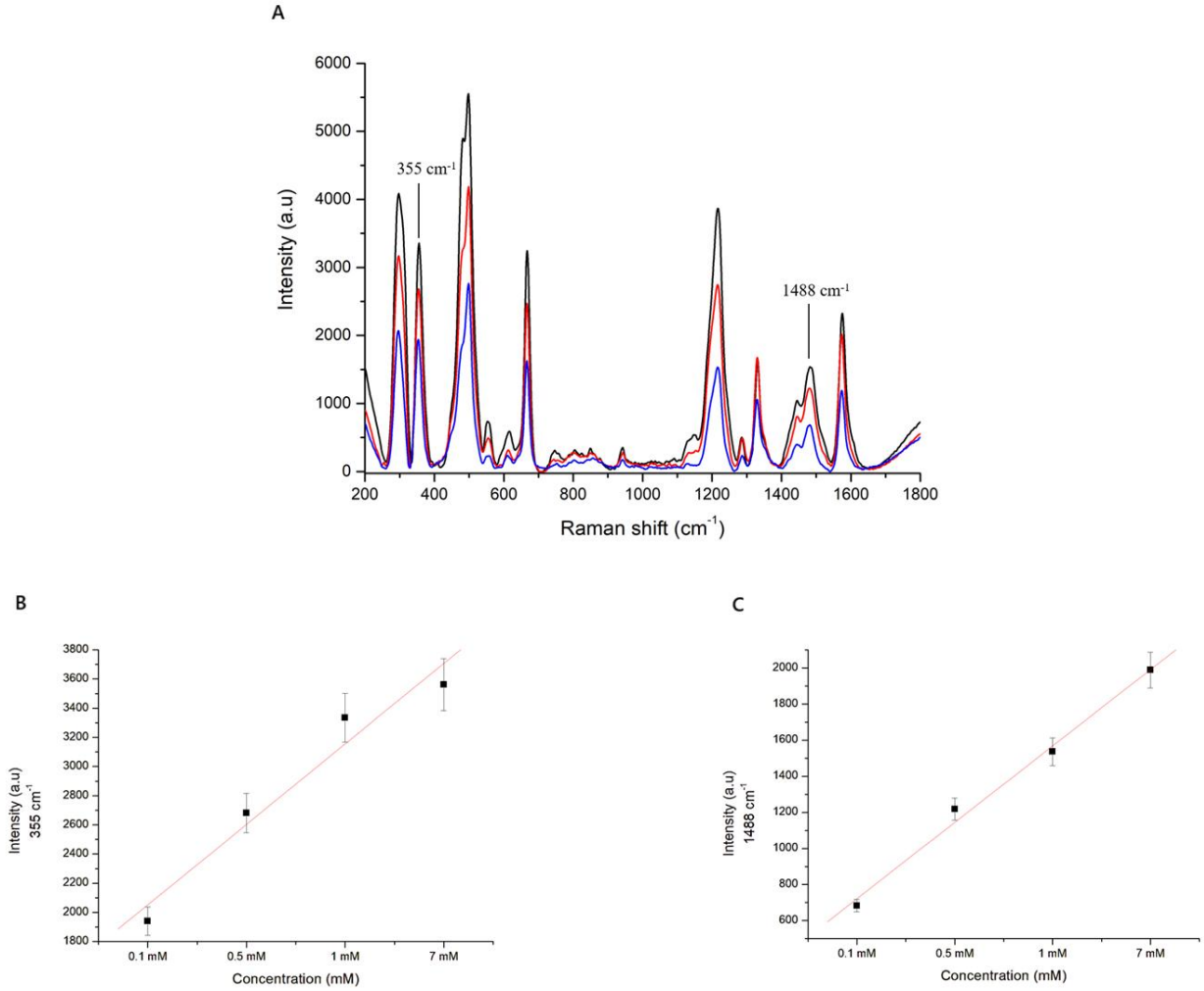

Figure 70. A) SERS spectrum of catechol solution at 0.1 mM (blue line), 0.5 mM (red line) and 1 mM (black line) concentrations with Premium AgAu substrate at 785 nm excitation wavelength. Experimental conditions: 2s acquisition time, 4 accumulations and 50x optical objective, and OD equal to 0.3 (reduces the light intensity by 50%), so the laser power on the sample is 28.5 mW, with a 785 nm laser line. **B**) linearity range for the intensity of the peak at 355 cm^{-1} (linear fitting parameters: a= [15± 2] $\cdot 10^2$ a.u, b= [55 ±8] ·10 a.u-/mM; r= 0.977) and **C**) at 1488 cm^{-1} (a= [30± 8] ·10 a.u, b= [42 ± 2]·10 a.u./mM; r= 0.995).

With Silmeco substrates for both excitation wavelengths, it is difficult to identify the characteristic Raman signature of catechol molecules, as the bare substrate shows a background signal that does not allow the phenol signals to be clearly distinguished. The SERSitive substrate is, in our study, the best substrate to use as it allows some characteristic bands of the target molecule to be recorded more clearly with a relatively good signal-to-noise ratio. These commercial SERS substrates, with different surface morphologies, can increase the Raman signal of the analyte depending on the type of SERS-active surface in contact with the sample. The choice of a suitable substrate is therefore an important factor to consider before starting measurements.

6.2.3 Performance of the homemade SERS substrate

As a first step, a solution of catechol at a concentration of 7 mM is placed on a glass slide, and the Raman spectrum is performed, as shown in Figure 71. No signal of the analyte is observed, while features due to glass are visible between 500 and 1200 cm^{-1}, particularly a strong signal at 560 cm^{-1}, 790 cm^{-1} and 1100 cm^{-1} is observed. The reason could be that the concentration of the catechol solution was too low to be detected.

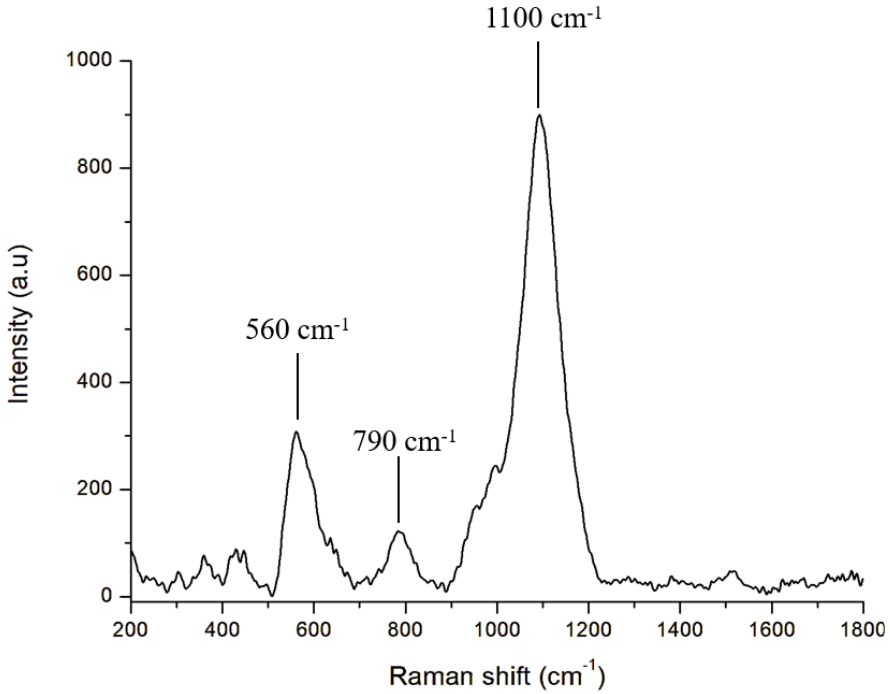

Figure 71. Raman spectrum of catechol solution (7 mM) acquired with a 532 nm excitation wavelength. Experimental conditions: 50x optical objective, 10s acquisition time, and 6 accumulations.

As described in paragraph *5.2.1.3*, homemade substrates were fabricated by placing a drop of gold nanoparticle solution (AuNPs) on a glass slide and leaving it to dry overnight. To assess the SERS performance of the homemade substrate for catechol detection, a few microlitres of phenol solution at different concentrations (0.1 mM, 0.5 mM, 1 mM and 7 mM) were deposited directly on the same glass slide where the drop of AuNPs had been placed and the measurement was performed immediately and spectra acquired. Representative spectra are shown in Figure 72, showing a signal due to the presence of catechol. The SERS spectrum of the catechol solution at a concentration of 7 mM (Figure 72, black line) presented many characteristic bands, particularly those at 775, 1032 and 1274 cm^{-1}, with the assignments reported in Table 5. The dominant SERS band at all considered concentrations was at 914 cm^{-1}, attributed to ring skeletal radial vibration. It could be used specifically to identify the presence of catechol. The linearity range for catechol concentrations was between 0.1

and 7 mM, with a sensitivity of 100 ± 40 mM^{-1}. These results agree with those reported in the literature (Barveen, 2022), which analysed the efficiency of SERS spectroscopy for catechol detection using complex nanostructures.

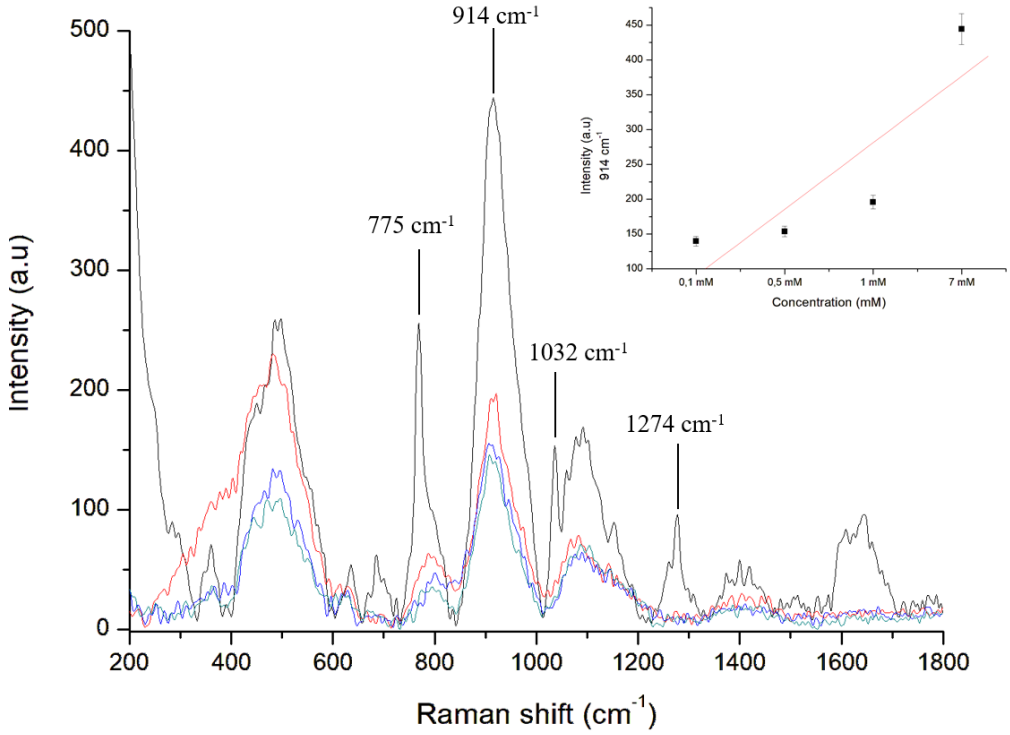

Figure 72. SERS spectra of catechol solution at different concentrations: 7 mM (black line), 1 mM (red line), 0.5 mM (blue line) and 0.1 mM (green line) on a drop of AuNPs, and linearity range for the intensity of the peak at 914 cm^{-1} (linear fitting parameters: a= -5 ± 10 a.u., b= [10 ± 4] ·10 a.u,/mM; r= 0.865) (inset). Experimental conditions: 532 nm excitation wavelength, 50x optical objective, and OD equal to 0.3 (reduces the light intensity by 50%), so the laser power on the sample is 8.5 mW, with a 532 nm laser line; 10s acquisition time and 6 accumulations.

SERS measurements performed using both commercial and home-made substrates enabled the detection of catechol at a concentration of 0.1 mM, which, in our case, represents the lowest detectable concentration for this compound.

Although the use of commercial substrates, particularly the Premium-AgAu substrate, appears to be the best, in our case, to obtain a good signal-to-noise ratio and to record characteristic bands of the target molecule, it is important to emphasize that the reliability and reproducibility of the signals proved to be an issue. This substrate allows a good result in terms of band clarity, but it does not guarantee constant reproducibility of the signal over time, which could compromise the validity and precision of the measurements. On the other hand, the homemade substrate, while exhibiting lower signal intensities than commercial substrates, appears to excel in spectral quality and reproducibility. This suggests that it may be more suitable for applications where accuracy and repeatability are critical for reliable analysis.

6.3 Investigation of the interaction between phenols and membrane models

Although the toxic properties of catechol for human health are known, research on how it interacts with cells and its effects on cell membranes is limited. The use of membrane models, designed to replicate the lipid arrangement of natural cell membranes, has stimulated interest in studying targeted interactions with external agents and effects at the molecular level. In the present study, two membrane models (DPPC and DOPC) were used to test the impact of phase heterogeneity: one in a pure liquid-condensed phase and another with coexisting liquid-condensed and expanded phases. The membrane changes induced by catechol exposure were assessed by compressibility (π-A isotherms) and atomic force microscopy (AFM) imaging.

6.3.1 Effects of catechol on membrane models and monolayer characterization with Atomic Force Microscopy

6.3.1.1 Characterization of catechol adsorption at the interface

To investigate the effect of catechol on the membrane model, the ability of catechol to adsorb at the interface was studied. Successive injections of catechol solution were conducted for this purpose, with each injection occurring every 40 minutes. This time interval was determined by the need to obtain a complete lipid compression isotherm. Additionally, it was important to ensure that the catechol concentration was sufficiently low to prevent aggregation or interfacial saturation (Vié, 2010). In Figure 73A, the surface pressure and ellipsometric angle, measured 40 minutes after injection, are plotted as a function of the catechol subphase concentration, which ranges from $1x10^{-7}$ mol/L to $1x10^{-2}$ mol/L. Figures 73B and 73C show the adsorption kinetics for two concentrations, $1x10^{-5}$ mol/L and $1x10^{-2}$ mol/L, over 40 minutes. Regarding surface pressure, from $1x10^{-7}$ to $1x10^{-4}$ mol/L, the variation is negligible, as shown in Figure 73B, where the surface pressure remained constant during the time considered. This suggests that the catechol solution injection initially changes the surface pressure, which then stabilizes. In the same concentration range, the ellipsometric angle increased from 0.3° to 1°. At higher subphase concentrations, up to $1x10^{-2}$ mol/L, the surface pressure and the ellipsometric angle increased similarly (Figure 73A), reaching 1 mN/m and 1.5°, respectively. In Figure 73C, the surface pressure increased immediately after injection due to the rapid absorption at the higher concentration, then stabilized after 40 minutes. In summary, these catechol concentrations injection induces a rapid but modest increase in subphase concentration near the interface and a slight increase in surface pressure up to $1x10^{-4}$ mol/L, with a $1x10^{-2}$ mol/L concentration surface pressure increase reaching 1 mN/m. For the subsequent experiments, it was important to confirm that the surface pressure did not increase during the 40 minutes.

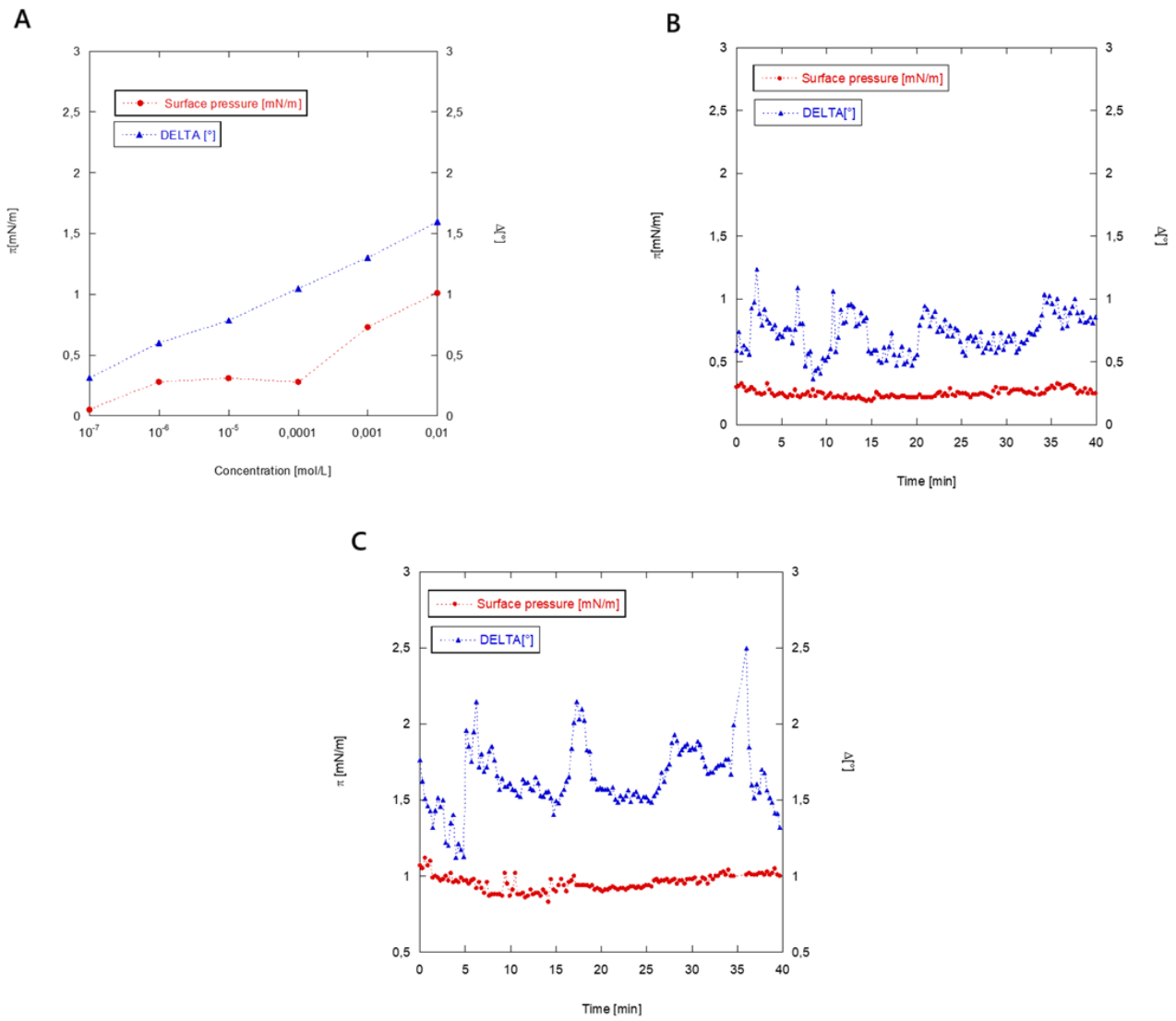

Figure 73. Catechol absorption at the air/liquid interface. (**A**) Surface pressure and ellipsometric angle as a function of six catechol subphase concentrations ranging from $1x10^{-7}$ mol/L to $1x10^{-2}$ mol/L. (**B**) Kinetics of surface pressure and ellipsometric angle over 40 minutes for a $1x10^{-5}$ mol/L catechol subphase concentration, and (**C**) for a $1x10^{-2}$ mol/L catechol subphase concentration.

6.3.1.2 Effects of catechol on π-A isotherms

Figure 74A presents the π–A isotherms for DPPC monolayers spread on ultrapure water, both in the absence and presence of catechol in the subphase at concentrations of 1×10^{-5} mol/L and 1×10^{-2} mol/L. These isotherms provide insight into the physical states adopted by the monolayer during compression and thus illustrate how catechol influences the molecular organization of the lipid film at the air-water interface. In pure water (red signs in Fig. 74A), the π–A isotherm of DPPC displays an initial rise in surface pressure beginning around 120 Å²/molecule, known as the lift-off point, indicating the

monolayer enters the liquid-expanded (LE) phase. The surface pressure then levels around 6 mN/m, marking the transition from LE to liquid-condensed (LC) phases. Following this plateau, the pressure increases steadily until it reaches 37 mN/m, signifying the point of minimum area per molecule. These surface pressure characteristics are consistent with values previously reported, though slight variations may arise depending on the subphase composition (Vié, 1998; Ruiz, 2017). When catechol is introduced into the subphase at 1×10^{-2} mol/L (green signs in Fig. 74A), significant changes are observed in the isotherm. The entire curve shifts towards larger mean molecular areas, indicating an interaction between catechol and the lipid monolayer. The lift-off point occurs at a larger molecular area-approximately 170 Å²/molecule compared to 120 Å²/molecule for the control-suggesting that molecular interactions are now taking place at greater spacing between DPPC molecules (an increase of ~4.5%). At this concentration, catechol is likely adsorbing to the interface and intercalating between the lipid molecules. Moreover, the LE–LC phase transition occurs at a higher surface pressure than in the catechol-free condition, indicating that the disorder of the monolayer (LE phase) is sustained up to 20 mN/m. The phase transition plateau also becomes less distinct, a behaviour commonly seen in mixed monolayers. This finding aligns with previous work by Katata et al., who studied the interaction between DPPC and bisphenol A at a lower concentration (1×10^{-5} mol/L) (Katata, 2022). Bisphenol A, with its bolaamphiphilic nature, exhibits surfactant-like properties that influence surface activity. In contrast, catechol at the same concentration does not display significant surface activity yet still appears to interact with DPPC molecules. At a catechol concentration of 1×10^{-5} mol/L (blue signs in Fig. 74A), the π-A isotherm is virtually identical to that of pure DPPC, suggesting minimal or no impact at this lower concentration. However, further structural insights can be gained by analyzing the monolayer compressibility. The monolayer compressibility (C_s) is calculated using the equation (6) (Bourlieu, 2020):

$$C_s^{-1} = -\frac{1}{A} \times \frac{dA}{d\pi} \tag{6}$$

Here, A denotes the molecular area at a given surface pressure π. Often, the inverse of compressibility, C_s^{-1}, referred to as the surface compressional modulus or monolayer elasticity, is used instead. The C_s^{-1} curves for pure DPPC and DPPC with catechol at both tested concentrations are depicted in Figure 74B. Originally defined in the 1960s, values of C_s^{-1} help classify monolayer states such as gaseous, LE, LC, or solid; higher values reflect more condensed and rigid monolayers (Davies, 1961). For pure DPPC (Fig. 74B, red signs), and DPPC with 1×10^{-5} mol/L catechol (Fig. 74B, blue signs), the modulus increases and then dips to a minimum at around 5 mN/m—this minimum corresponds to the LE–LC phase transition. When the subphase contains 1×10^{-2} mol/L catechol (Figure 74B, green

signs), this minimum shifts to 20 mN/m, indicating a delayed transition due to the presence of catechol. Beyond the transition, the compressional modulus increases again. This behaviour is consistent with the results of Maximino et al. (Maximino, 2021), who observed a similar trend with bisphenol A at 1×10^{-5} mol/L, suggesting the lipids remain less condensed and the monolayer is more flexible. Interestingly, at low catechol concentrations (1×10^{-5} mol/L), the compressional modulus increases more rapidly than in the pure DPPC monolayer, indicating that catechol slightly condenses the film even though this effect is not visible in the π–A isotherm alone. This subtle interaction, revealed by compressibility data, highlights molecular interactions at low concentrations. A comparable phenomenon has been reported by Guzman et al., with the incorporation of cholesterol into DPPC monolayers (Guzman, 2013), where the high hydrophobicity of cholesterol promotes ordering among DPPC molecules, thereby condensing the lipid film. On the other hand, at higher catechol concentrations (1×10^{-2} mol/L), the compressional modulus increases more slowly and remains lower than that of pure DPPC, reaching only about 32 mN/m. This suggests a more fluid monolayer structure, likely due to catechol's presence within the lipid film. After 32 mN/m, the modulus increases once again and even surpasses that of the pure DPPC monolayer. This surface pressure is comparable to lateral pressures found in biological membranes, implying that catechol may influence membrane fluidity at the cellular level.

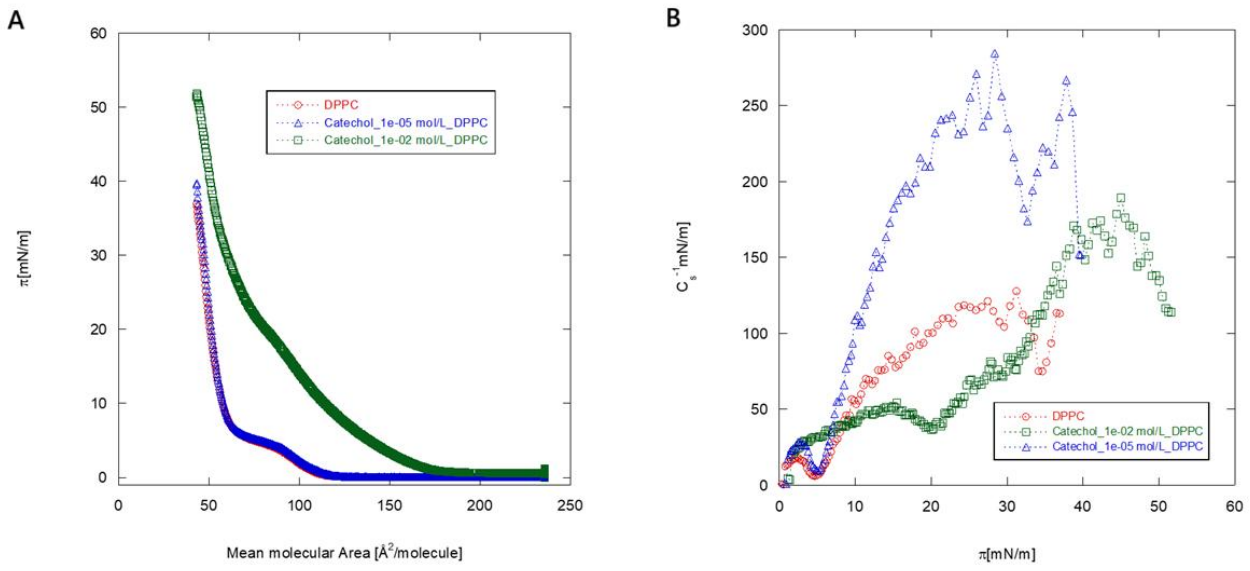

Figure 74. A) π-A isotherms of DPPC in ultrapure water and with catechol subphase concentrations of $1x10^{-5}$ mol/L and $1x10^{-2}$ mol/L. **B**) Monolayer compressional moduli (C_s^{-1}) of pure DPPC (red sign), with $1x10^{-5}$ mol/L and $1x10^{-2}$ mol/L catechol subphase concentrations (blue and green signs, respectively), as a function of surface pressure.

The interaction effects of catechol with the lipid monolayer were also examined using the DPPC/DOPC membrane model. The unsaturation present in the fatty acid chains of DOPC molecules

induces disorder in the lipid interfacial monolayer at ambient temperature. As a result, DOPC remains in a liquid-expanded state throughout the compression process. Consequently, the lipid monolayer exhibits a phase separation between LC and LE phases, occurring at a surface pressure higher than the LE/LC phase transition observed for DPPC. This transition is not visible in the π–A isotherm for the DPPC/DOPC mixture in ultrapure water, as shown in Figure 75A (red signs), due to the large molecular area occupied by DOPC (Guzman, 2012). Previous studies have directly observed the formation of phase-separated domains in the DPPC/DOPC mixture under the influence of both lipids using atomic force microscopy (Vié, 1998). The presence of catechol in the subphase at concentrations of 1×10^{-5} mol/L and 1×10^{-2} mol/L affects the isotherms by shifting the curves towards higher mean molecular areas. Even at low catechol concentrations in the subphase, the surface pressure shows a notable change, with a stronger effect than in the DPPC monolayer. The profiles of the curves are similar, but at higher surface pressures (around 35 mN/m), the curves overlap. This could be explained by the presence of two unsaturated alkyl chains in the DOPC molecules, which remain in the liquid-expanded phase, allowing the phenol to intercalate more effectively between the lipid molecules at this phase and to stay at the air/water interface during compression. This is consistent with Maximino's findings, which suggest that the presence of pollutants increases the fluidity of membranes (Maximino, 2021).

However, at higher surface pressures, some catechol molecules seem to be pushed out into the subphase, as evidenced by the superposition of the curves. These observations are further supported by the monolayer compressional moduli (C_s-^{1}) analysis as a function of surface pressure, shown in Figure 75B. Specifically, the values of C_s^{-1} for the three experiments (DPPC/DOPC with and without catechol at two concentrations) are similar and fall within the same range as those for DPPC alone, except for the case with low catechol concentration, which remains an exception. At high surface pressures, catechol molecules are partially expelled from the air-water interface, facilitating a rearrangement of the lipid molecules.

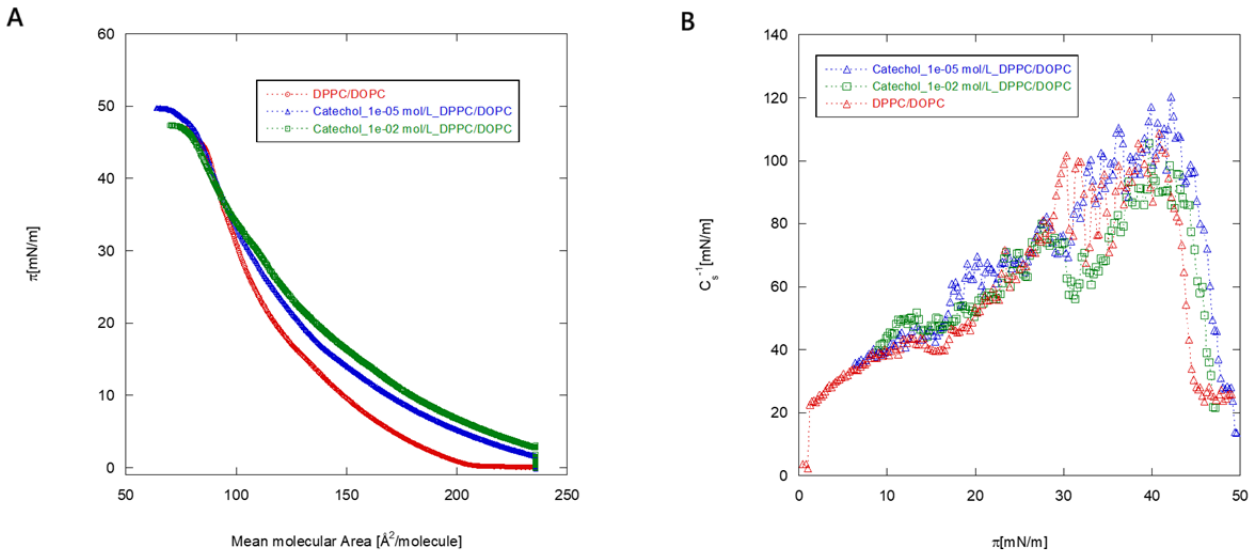

Figure 75. **A**) π-A isotherms of DPPC/DOPC mixture in ultrapure water and with catechol subphase concentrations of $1x10^{-5}$ mol/L and $1x10^{-2}$ mol/L. **B**) Monolayer compressional moduli (C_s^{-1}) of pure DPPC/DOPC mixture (red sign), with $1x10^{-5}$ mol/L and $1x10^{-2}$ mol/L catechol subphase concentrations (blue and green signs, respectively), as a function of surface pressure.

6.3.1.3 Topographic imaging to study the effects of catechol on membrane model

Atomic Force Microscopy (AFM) images were obtained from samples prepared using the Langmuir-Blodgett technique, which involves transferring lipid films onto a solid substrate (mica) at a constant surface pressure of 20 mN/m. The AFM images for both the pure monolayer and the DPPC monolayer in the presence of catechol at two different subphase concentrations are displayed in Figure 76 (A-I)**.** For the bare DPPC monolayer, the topographic images (Figures 76A-C) reveal a well-defined liquid-condensed phase, consistent with previous literature reports (Leonenko, 2004). The darker regions indicate areas where fractures are present, with approximately 20% of the monolayer exhibiting fractures. Upon examining the profile, the lipid film shows an average fracture depth of 0.8 ± 0.1 nm (Figure 77, red sign). For the DPPC monolayer in the presence of catechol at a concentration of 1×10^{-5} mol/L (Figures 76D-F), the AFM images display similar characteristics. The fractures and corresponding profiles (Figure 77A, blue sign) yield a depth of 0.71 ± 0.06 nm, which is slightly less than that observed in the pure DPPC monolayer, though the difference is not statistically significant ($p>0.05$). Therefore, no noticeable condensation effect is observed in the AFM images. When catechol at a concentration of 1×10^{-2} mol/L is introduced into the subphase, a noticeable change in the micrometer-scale morphology occurs compared to the pure DPPC monolayer, leading to increased disorder (Figures 76G-I). In this case, the fracture depth decreases to 0.58 ± 0.01 nm (Figure 77B, blue sign), which is significantly lower ($p < 0.05$) than the depth observed in the pure lipid monolayer.

Additionally, a slight increase in the relative fracture area is observed, reaching around 22%. This suggests that at this higher concentration, catechol interacts with the polar headgroups of the lipid molecules, causing them to expand and create additional space for the alkyl chains. The fractures between the liquid-condensed phase domains become curved rather than straight, indicating a less condensed structure.

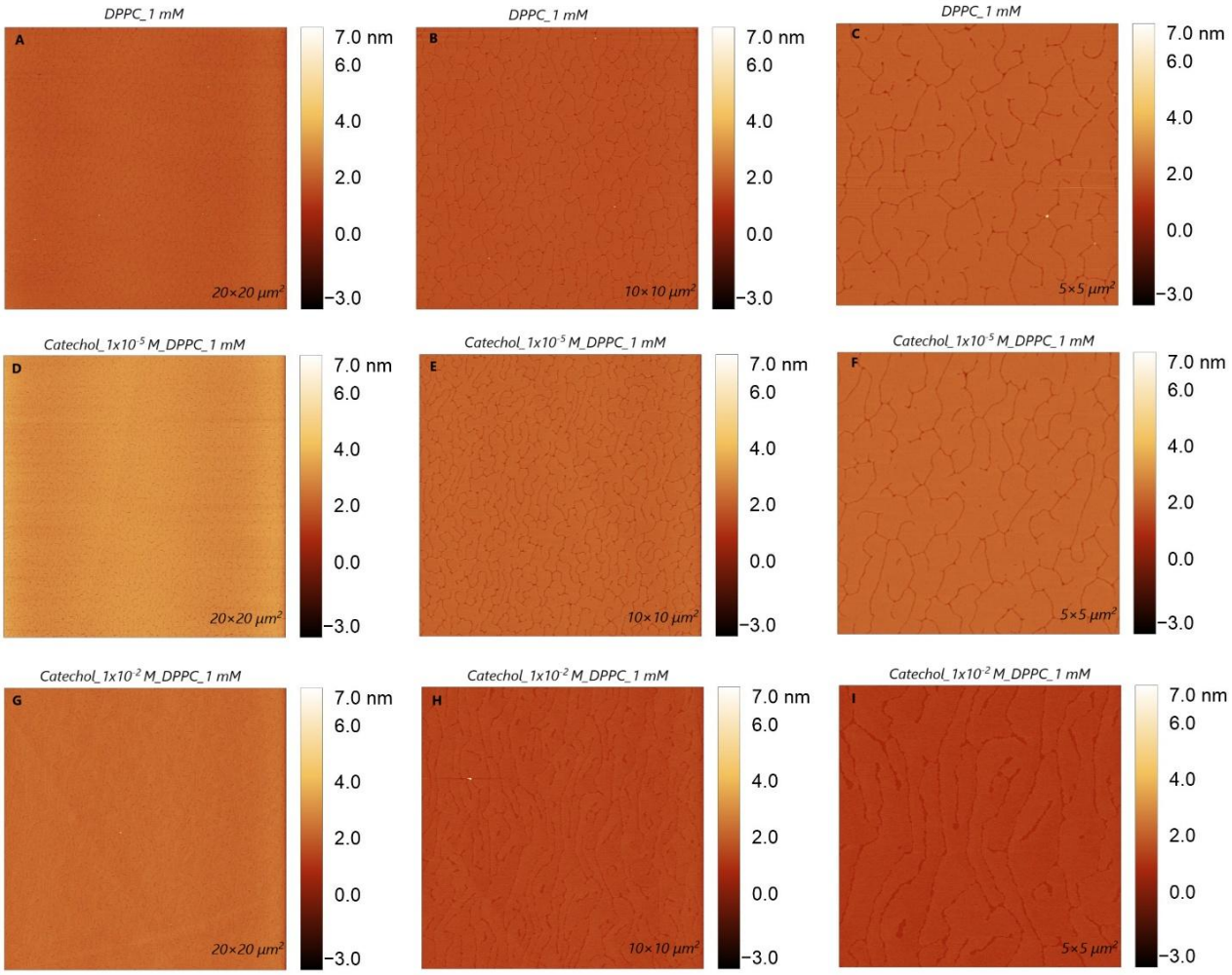

Figure 76. (**A-C**) AFM images of DPPC at three distinct scan sizes (20x20, 10x10 and 5x5 µm^2), (**D-F**) DPPC with 1x10^{-5} mol/L, and (**G-I**) 1x10^{-2} mol/L catechol subphase concentrations.

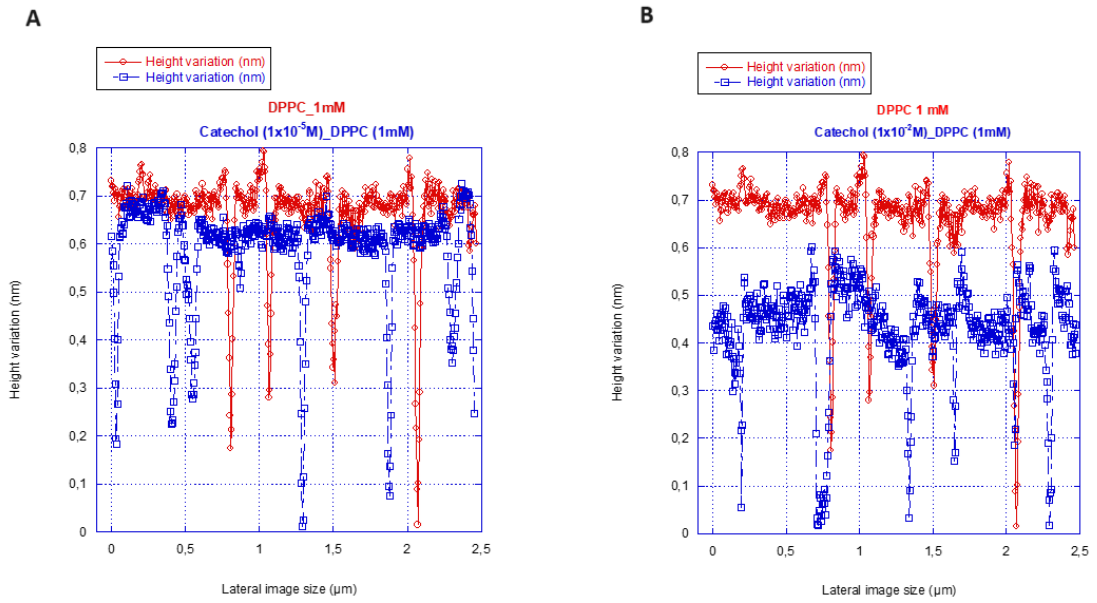

Figure 77. Height variation profiles were obtained from the AFM images of the neat DPPC monolayer (red sign), and with (**A**) 1x10^{-5} mol/L, (**B**) 1x10^{-2} mol/L catechol subphase concentrations (blue sign).

A similar AFM analysis was carried out on DPPC/DOPC monolayers, both in the absence and presence of catechol. The AFM topographic images are shown in Figure 78, highlighting the phase separation in monolayers composed of a 1:1 molar ratio of the two immiscible lipids, DPPC and DOPC. In the DPPC/DOPC control sample (Figures 78A–C), two distinct structural features are observed: the elevated, brighter domains correspond to DPPC regions embedded within the liquid-expanded DOPC matrix, consistent with previous studies that confirm limited miscibility between the two lipid types (Vié, 1998; Guzman, 2012; Bourlieu, 2016). A histogram depicting the size distribution of these domains is presented in Figure 79A, revealing a bimodal pattern. The smaller domains have an average width of 164 ± 3 nm, while the larger domains reach an average size of about 1 µm, a distribution that has also been reported in earlier research (Vié, 1998). Figures 78D–F show the AFM images for the DPPC/DOPC monolayer in the presence of catechol at a subphase concentration of 1×10^{-5} mol/L. The corresponding histogram in Figure 79B also displays a bimodal domain size distribution. However, in this case, the distinction between large and small domains is less pronounced. A reduction in the size of the larger domains is observed, leading to a more uniform distribution, with most domains averaging around 500 nm in width.

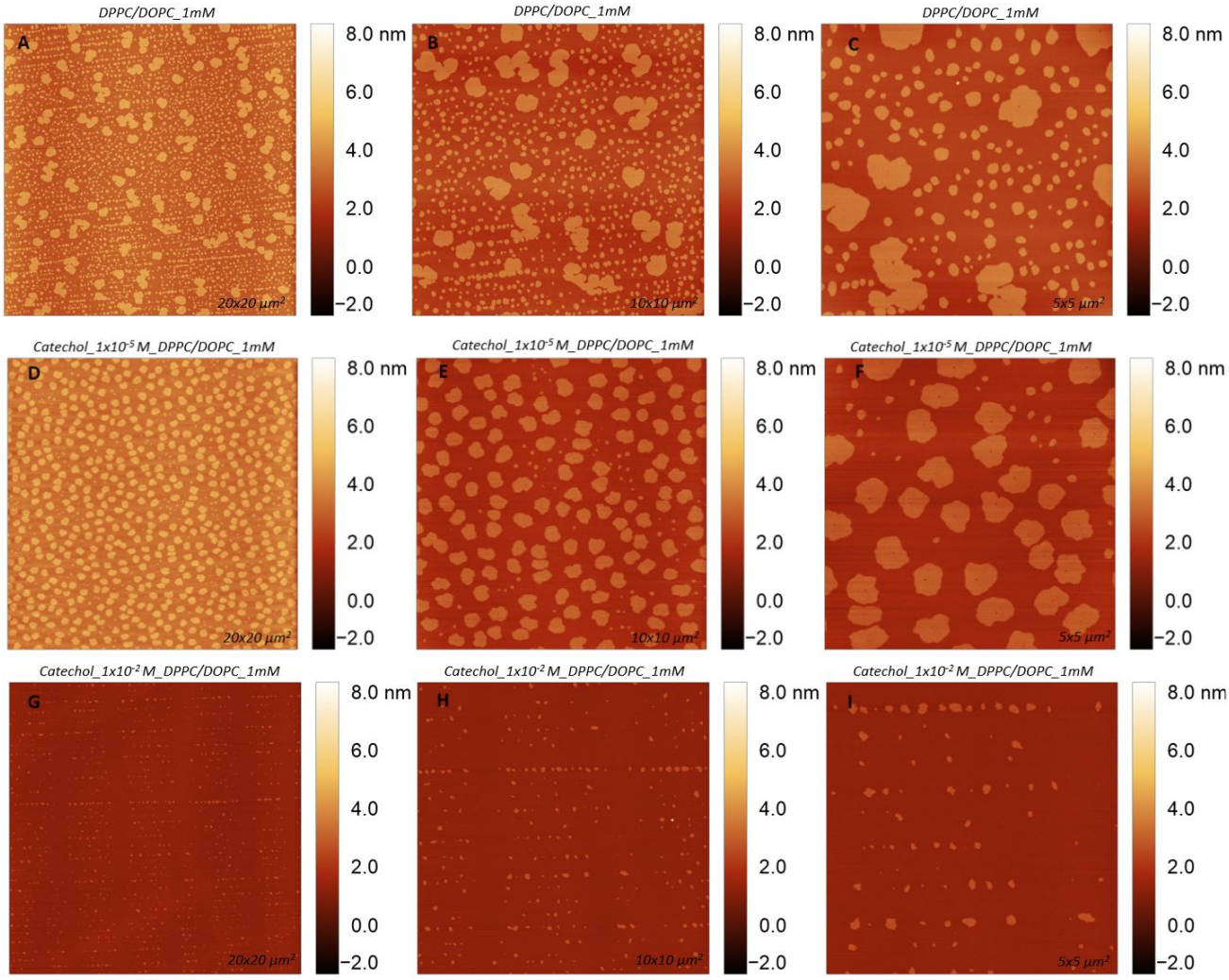

Figure 78. (**A-C**) AFM images of DPPC/DOPC mixture at three distinct scan sizes (20x20, 10x10 and 5x5 µm^2), (**D-F**) DPPC/DOPC with 1x10^{-5} mol/L, and (**G-I**) 1x10^{-2} mol/L catechol subphase concentrations.

Figure 78G-I shows the AFM image for the DPPC/DOPC monolayer with 1x10^{-2} mol/L catechol concentration, where small bright spots appear, but they are not uniformly distributed across the interface. The histogram is presented in Figure 79C, with a monomodal distribution (an average width of 138 ± 2 nm), significantly smaller than that of the bare DPPC/DOPC mixture ($p<0.01$). These findings indicate that, at this specific concentration, catechol enhances the miscibility of DPPC in DOPC, effectively inhibiting the formation of the liquid-condensed (LC) phase. In theory, if catechol molecules integrate more readily into the liquid-expanded (LE) phase, such as that provided by the DOPC matrix, there should be no noticeable alteration in the distribution or quantity of LC domains. However, the data imply that catechol may preferentially localize within DPPC-rich regions, even when DOPC is present.

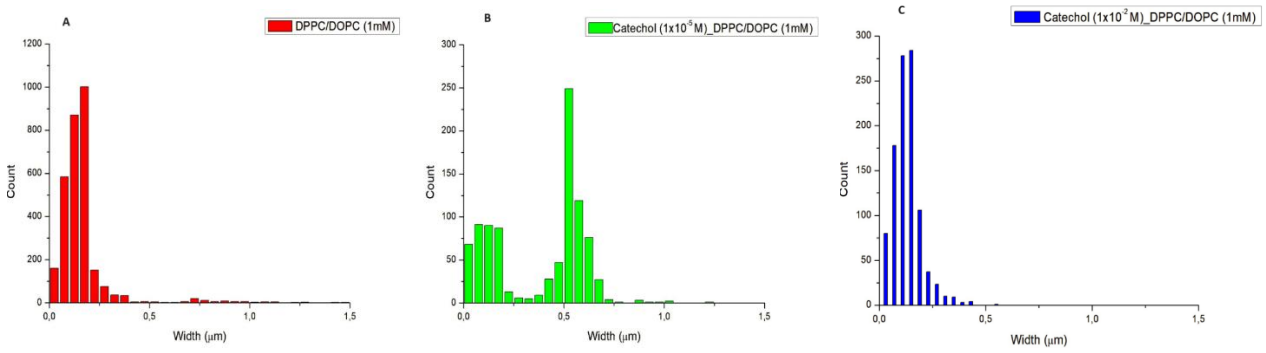

Figure 79. A) Histogram of the domain distribution in the neat DPPC/DOPC mixture, **B**) with $1x10^{-5}$ mol/L, and **C**) $1x10^{-2}$ mol/L catechol subphase concentrations.

In summary, catechol affects lipid monolayers in a concentration-dependent manner, with its impact influenced by lipid composition. In DPPC monolayers, low catechol levels increase compressibility, indicating tighter lipid packing, while high concentrations shift the isotherm, reduce rigidity, and induce fluidization by disrupting lipid order. In DPPC/DOPC mixtures, catechol shows stronger effects due to DOPC's inherent fluidity, promoting intercalation even at low concentrations. At high surface pressures, isotherms converge, suggesting catechol expulsion. AFM imaging confirms increased disorder and morphological changes, including smaller domains and enhanced miscibility. Overall, catechol influences membrane organization and may play a role in modifying the behaviour of cellular membranes. This piece of information about the effects on model membranes of catechol holds potential for designing future detection schemes of catechol in cells, eventually using available or future techniques enabling the monitoring of the observed changes.

CONCLUSIONS

During the PhD project, distinct approaches based on optical schemes for detecting catechol were selected due to their potential advantages in terms of adaptability and cost-effectiveness compared to alternative techniques and investigated. On the one hand, the focus has been on studying optical biosensing schemes based on absorption and fluorescence spectroscopy and, subsequently, on optical sensing approaches based on SERS (Surface-Enhanced Raman Spectroscopy). In the first direction, the use of a laccase-based biosensing scheme, exploiting the optical properties of the laccase from *Trametes versicolor*, was tested for the realisation of catechol detection via absorption and fluorescence techniques. Laccase-based biosensing scheme demonstrated reliable detection through both UV-Vis absorption and fluorescence spectroscopy, exploiting enzymatic oxidation and subsequent optical signal changes to achieve selectivity and sensitivity. Optimisation of experimental conditions, such as incubation time, was a key step of the study that demonstrated the potential of fluorescence spectroscopy, which is less commonly used for phenol detection compared to absorption. This approach could find application in areas such as environmental monitoring and diagnostics. On the other hand, a SERS-based optical sensing scheme was considered and studied. In this context, several commercial and home-made SERS substrates were used to select the best for catechol detection in aqueous matrices. The results showed that one of the commercial substrates, Premium-AgAu substrate, shows good enhancement of catechol features, but signal reproducibility over time proved to be an issue. On the other hand, homemade substrates, although producing lower signal intensities, exhibited higher spectral quality and improved reproducibility, suggesting their suitability for applications where data reliability is critical. In both approaches, the main challenge was to optimise the techniques to ensure accurate and reproducible results. SERS-based approach confirmed its potential, the proposed scheme providing a label-free and highly sensitive detection platform, enabling the identification of catechol at trace levels through its characteristic vibrational signatures. Both fluorescence-based biosensing and SERS-based sensing approaches have distinct advantages but are complementary in that they meet different requirements for sensitivity, reproducibility and practical applicability.

The results of the investigation of catechol effects on lipid monolayers composed of pure DPPC and mixed DPPC/DOPC systems show that catechol acts in a concentration-dependent manner and that its effects are influenced by the lipid composition. In the DPPC monolayer, at low catechol concentration (1×10^{-5} mol/L), the compressibility modulus increases, indicating that catechol interacts at the molecular level, promoting tighter lipid packing and a condensation effect. At higher concentration (1×10^{-2} mol/L), catechol causes a shift of the isotherm toward larger molecular areas,

delays the LE–LC phase transition, reduces monolayer rigidity, the surface disorder increases while fracture depth decreases, and the morphology domain is altered. These results suggest that catechol inserts between lipid molecules, disrupts ordering, and induces fluidization. In the DPPC/DOPC mixed system, where DOPC's unsaturated chains introduce initial disorder and increased fluidity, catechol has a stronger effect. Even at low concentrations, the isotherm shifts, indicating enhanced intercalation. At high surface pressures (~35 mN/m), however, the isotherms converge, suggesting partial expulsion of catechol from the monolayer into the subphase. In DPPC/DOPC monolayers, catechol reduces domain size and indicates improved miscibility between DPPC and DOPC. In conclusion, catechol acts as a modulator of membrane structure, inducing condensation at low concentrations and fluidization at high concentrations, depending on the lipid environment. These results opened the possibility of monitoring catechol directly inside cells, suggesting that catechol could selectively alter the dynamics of biological membranes. In summary, the investigation of catechol's interaction with lipid membrane models offered new insights into its affinity for lipid interfaces, suggesting possible bioaccumulation behaviours and implications for membrane-associated sensing mechanisms.

Together, all the sensing schemes investigated form a multifaceted framework for catechol monitoring, particularly valuable in environmental and bioanalytical applications where precision, biocompatibility, and detection versatility are essential. The single approaches as well as the multi-technique approach hold potential for future development of phenol detection methods in various matrices.

APPENDIX- Summary of activities carried out during the PhD

This PhD thesis entitled "*Optical methods for the detection of phenolic pollutants in aqueous matrices*" has been submitted to the Department of Economics, Engineering, Society and Business Organization (DEIM) at the University of Tuscia to obtain the PhD degree in "Engineering for Energy and Environment", curriculum "Biosystems and Environment".

From November 2022 to March 2023, research was conducted at the A.P.E. Research Company (Basovizza, Trieste, Italy) under the supervision of Stefano Prato, one of the company's founders.

For the periods from April to July 2023 and from August to November 2023, research was conducted at Universitè de Rennes 1 (Institut de Physique de Rennes-IPR), under the supervision of Professor Véronique Vié.

For the remaining periods, the research was conducted at the home institution, within the Optical Spectroscopy laboratory, at the Department of Ecological and Biological Sciences, led by Professor Ines Delfino, supervisor of all the PhD research activity.

The project was fully funded by the program **PON FSE REACT-EU "Ricerca e Innovazione" (2014- 2020)** within the framework of the "Innovation and Green" thematic doctoral programs.

The research paper and manuscripts listed below are outcomes of the work carried out during the PhD project:

- **Conigliaro, P**.; Massaro, F.; Portaccio, M.; Lepore, M.; Delfino, I. Study of Absorbance and Fluorescence Properties of Laccase and Catechol Solutions in the UV Range. *Eng. Proc.* **2022**, *27*, 32. https://doi.org/10.3390/ecsa-9-13333

- **Conigliaro, P**.; Portaccio, M.; Lepore, M.; Delfino, I. Optical Properties of Laccases and Their Use for Phenolic Compound Detection and Quantification: A Brief Review. *Appl. Sci.* **2023**, *13*, 12929. https://doi.org/10.3390/app132312929

- **Conigliaro, P.**; Prato, S.; Troian, B.; Naumenko, A.; Pisano, V.; Delfino, I. Application of SERS Spectroscopy for the Study of Biological Molecules. *Eng. Proc.* **2023**, *58*, 27.

https://doi.org/10.3390/ecsa-10-16164

- **Conigliaro, P.**; Vié, V. et al., Delfino, I.; Impact of Catechol on Membrane Model. Manuscript in preparation.

During my PhD, I was also a co-author of the following work:

- Zippilli, C.; Filippi, S.; Cesarini, S.; Bizzarri, B.M.; **Conigliaro, P.**; De Marchi, E.; Botta, L.; Saladino, R. Synthesis of Artesunic Acid−Coumarin Hybrids as Potential Antimelanoma Agents. *ACS Med. Chem. Lett.* **2023**, *14*, 599−605. https://doi.org/10.1021/acsmedchemlett.3c00019

During PhD project, I participated in International and National Conferences, as listed below:

- 9th International Electronic Conference on Sensors and Applications (**ECSA-9**); 1-15 November 2022| Online.
- 10th International Electronic Conference on Sensors and Applications (**ECSA-10**); 15-30 November 2023| Online.
- XXVII Congresso Nazionale **SIBPA 2024** *(Società Italiana di Biofisica Pura e Applicata); 16-20 giugno 2024, Genova*| Poster session.

REFERENCES

Abdullah, J.; Ahmad, M.; Heng, L.; Karuppiah, N.; Sidek, H. An Optical Biosensor Based on Immobilization of Laccase and MBTH in Stacked Films for the Detection of Catechol. *Sensors* **2007**, *7*, 2238–2250. https://doi.org/10.3390/s7102238

Abin, P.; Kumar, A.R. The Performance Enhancement of Surface Plasmon Resonance Optical Sensors Using Nanomaterials: A Review. *Coord. Chem. Rev.* **2022**, *458*, 214424. https://doi.org/10.1016/j.ccr.2022.214424

Ahmaruzzaman, M.D.; Mishra, S.R.; Gadore, V.; Yadav, G.; Roy, S.; Bhattacharjee, B.; Bhuyan, A.; Hazarika, B.; Darabdhara, J.; Kumari, K. Phenolic Compounds in Water: From Toxicity and Source to Sustainable Solutions – An Integrated Review of Removal Methods, Advanced Technologies, Cost Analysis, and Future Prospects. *J. Environ. Chem. Eng.* **2024**, *12*, 112964. https://doi.org/10.1016/j.jece.2024.112964

Al Mamari, H. Phenolic Compounds: Classification, Chemistry, and Updated Techniques of Analysis and Synthesis, **2022**. https://doi.org/10.5772/intechopen.98958

Albrecht, M.G.; Creighton, J.A. Anomalously Intense Raman Spectra of Pyridine at a Silver Electrode. *J. Am. Chem. Soc.* **1977**, *99*, 5215–5217. https://doi.org/10.1021/ja00457a071.

Albuquerque, B.R.; Heleno, S.A.; Oliveira, M.B.P.P.; Barros, L.; Ferreira, I.C.F.R. Phenolic Compounds: Current Industrial Applications, Limitations and Future Challenges. *Food Funct.* **2021**, *12*, 14–29. https://doi.org/10.1039/D0FO02324H.

Alessandrini, A.; Facci, P. AFM: A Versatile Tool in Biophysics. *Meas. Sci. Technol.* **2005**, *16*, R65–R92. https://doi.org/10.1088/0957-0233/16/6/R01.

Amine, A.; Mohammadi, H.; Bourais, I.; Palleschi, G. Enzyme Inhibition-Based Biosensors for Food Safety and Environmental Monitoring. *Biosens. Bioelectron.* **2006**, *21*, 1405–1423. https://doi.org/10.1016/j.bios.2005.07.012

Ando, T.; Uchihashi, T.; Kodera, N. High-Speed AFM and Applications to Biomolecular Systems. *Annu. Rev. Biophys.* **2013**, *42*, 393–414. https://doi.org/10.1146/annurev-biophys-083012-130324.

Andreu-Navarro, A.; Fernández-Romero, J.M.; Gómez-Hens, A. Determination of Polyphenolic Content in Beverages Using Laccase, Gold Nanoparticles and Long Wavelength Fluorimetry. *Anal. Chim. Acta* **2012**, *713*, 1–6. https://doi.org/10.1016/j.aca.2011.11.049.

Angel, S.; Carrabba, M.; Cooney, T. The Utilization of Diode Lasers for Raman Spectroscopy. *Spectrochim. Acta A Mol. Biomol. Spectrosc.* **1995**, *51*, 1779–1799. https://doi.org/10.1016/0584-8539(95)01443-X

Arregui, L.; Ayala, M.; Gómez-Gil, X.; Gutiérrez-Soto, G.; Hernández-Luna, C.E.; Herrera de los Santos, M.; Levin, L.; Rojo-Domínguez, A.; Romero-Martínez, D.; Saparrat, M.C.N.; Trujillo-Roldán, M.A.; Valdez-Cruz, N.A. Laccases: Structure, Function, and Potential Application in Water Bioremediation. *Microb. Cell Fact.* **2019**, *18*, 200. https://doi.org/10.1186/s12934-019-1248-0.

AtoID. [(accessed on 15 April 2025)]; Available online: http://www.atoid.com/shop/.

Awada, C.; Barbillon, G.; Charra, F.; Douillard, L.; Greffet, J.-J. Experimental Study of Hot Spots in Gold/Glass Nanocomposite Films by Photoemission Electron Microscopy. *Phys. Rev. B* **2012**, *85*, 045438. https://doi.org/10.1103/PhysRevB.85.045438.

Bag, S.; Bhowmik, S. Fluorescence Spectroscopy: A Useful Method to Explore the Interactions of Small Molecule Ligands with DNA Structures. In: Mandal, S. (Ed.) *Reverse Engineering of Regulatory Networks*. Methods in Molecular Biology, vol 2719. Humana, New York, NY, 2024. https://doi.org/10.1007/978-1-0716-3461-5_3

Barveen, N.R.; Wang, T.J.; Chang, Y.H.; Rajakumaran, R. Ultrasensitive and reusable SERS platform based on Ag modified WO_3 nanoflakes for catechol detection. *Mater. Sci. Eng. B* **2022**, *282*, 115753. https://doi.org/10.1016/j.mseb.2022.115753

Baumberg, J.; Bell, S.; Bonifacio, A.; Chikkaraddy, R.; Chisanga, M.; Corsetti, S.; Delfino, I.; Eremina, O.; Fasolato, C.; Faulds, K.; Fleming, H.; Goodacre, R.; Graham, D.; Hardy, M.; Jamieson, L.; Keyes, T.; Królikowska, A.; Kuttner, C.; Langer, J.; Lightner, C.; Mahajan, S.; Masson, J.-F.; Muhamadali, H.; Natan, M.; Nicolson, F.; Nikelshparg, E.; Plakas, K.; Popp, J.; Porter, M.; Prezgot, D.; Pytlik, N.; Schlücker, S.; Silvestri, A.; Stone, N.; Tian, Z.-Q.; Tripathi, A.; Willner, M.; Wuytens, P. SERS in biology/biomedical SERS: general discussion. *Faraday Discuss.* **2017**, *205*, 429–456. https://doi.org/10.1039/c7fd90089a.

Bhushan, B. Biosystems: Investigated by Scanning Probe Microscopy; Fuchs, H. (Ed.); Springer: Heidelberg, Germany, 2010.

Bilir, K.; Weil, M.-T.; Lochead, J.; Kök, F.N.; Werner, T. Construction of an Oxygen Detection-Based Optic Laccase Biosensor for Polyphenolic Compound Detection. *Turk. J. Biol.* **2016**, *40*, 1303–1310. https://doi.org/10.3906/biy-1602-40

Binnig, G.; Gerber, C.; Stoll, E.; Albrecht, T.R.; Quate, C.F. Atomic resolution with atomic force microscope. *Europhys. Lett.* **1987**, *3*, 1281–1286. https://doi.org/10.1209/0295-5075/3/12/006.

Binnig, G.; Quate, C.F.; Gerber, C. Atomic force microscope. *Phys. Rev. Lett.* **1986**, *56*, 930–933. https://doi.org/10.1103/PhysRevLett.56.930

Bocklitz, T.; Walter, A.; Hartmann, K.; Rosch, P.; Popp, J. How to pre-process Raman spectra for reliable and stable models? *Anal. Chim. Acta* **2011**, *704*, 47–56. https://doi.org/10.1016/j.aca.2011.06.043

Borato, C.E.; Leite, F.L.; Oliveira Jr, O.N.; Goy, R.C.; Campanha Filho, S.P.; Vasconcelos, C.L.; da Trindade Neto, C.G.; Pereira, M.R.; Fonseca, J.L.C.; Mattoso, L.H.C. Study of dielectric properties of nanocomposites. *IEEE Trans. Dielec. Elec. Insul.* **2006**, *13*, 1101–1109. https://doi.org/10.1109/TDEI.2006.247838

Bourlieu, C.; Mahdoueni, W.; Paboeuf, G.; Gicquel, E.; Ménard, O.; Pezennec, S.; Bouhallab, S.; Deglaire, A.; Dupont, D.; Carrière, F.; Vié, V. Physico-chemical behaviors of human and bovine milk membrane extracts and their influence on gastric lipase adsorption. *Biochimie* **2020**, *169*, 95–105. https://doi.org/10.1016/j.biochi.2019.12.003

Butler, H.J.; Ashton, L.; Bird, B.; Cinque, G.; Curtis, K.; Dorney, J.; Esmonde-White, K.; Fullwood, N.J.; Gardner, B.; Martin-Hirsch, P.L.; Walsh, M.J.; McAinsh, M.R.; Stone, N.; Martin, F.L.

Using Raman spectroscopy to characterize biological materials. *Nat. Protoc.* **2016**, *11*(4), 664–687. https://doi.org/10.1038/nprot.2016.036

Cacciari, R.D.; Reynoso, A.; Sosa, S.; Parodi, F.; Goldbaum, F.A.; Montejano, H.A.; Biasutti, M.A.; Reynoso, E. Effect of UVB solar irradiation on laccase enzyme: Evaluation of the photooxidation process and its impact over the enzymatic activity for pollutants bioremediation. *Amino Acids* **2020**, *52*, 925–939. https://doi.org/10.1007/s00726-020-02861-0

Caleja, C.; Ribeiro, A.; Barreiro, M.F.; Ferreira, I.C.F.R. Phenolic compounds as nutraceuticals or functional food ingredients. *Curr. Pharm. Des.* **2017**, *23*, 2787. https://doi.org/10.2174/1381612822666161227153906

Camerlingo, C.; Portaccio, M.; Delfino, I.; Lepore, M. Surface-enhanced Raman spectroscopy for monitoring extravirgin olive oil bioactive components. *J. Chem.* **2019**, *2019*, 1–10. https://doi.org/10.1155/2019/9537419

Cano-Raya, C.; Dencheva, N.V.; Braz, J.F.; Malfois, M.; Denchev, Z.Z. Optical biosensor for catechol determination based on laccase-immobilized anionic polyamide 6 microparticles. *J. Appl. Polym. Sci.* **2020**, *137* (38). https://doi.org/10.1002/app.49131

Cantarella, G.; d'Acunzo, F.; Galli, C. Determination of laccase activity in mixed solvents: Comparison between two chromogens in a spectrophotometric assay. *Biotechnol. Bioeng.* **2003**, *82*, 395–398. DOI: 10.1002/bit.10576

Chandra, R.; Chowdhary, P. Properties of bacterial laccases and their application in bioremediation of industrial wastes. *Environ. Sci. Process Impacts* **2015**, *17*, 326–342. https://doi.org/10.1039/C4EM00627E

Chen, C.; Wang, J. Optical biosensors: An exhaustive and comprehensive review. *Analyst* **2020**, *145* (5), 1605–1628. https://doi.org/10.1039/C9AN01998G

Chen, H.; Das, A.; Bi, L.; Choi, N.; Moon, J.I.; Wu, Y.; Park, S.; Choo, J. Recent advances in surface-enhanced Raman scattering-based microdevices for point-of-care diagnosis of viruses and bacteria. *Nanoscale* **2020**, *12*, 21560–21570. https://doi.org/10.1039/D0NR06340A

Clausell, A.; Busquets, M.A.; Pujol, M.; Alsina, A.; Cajal, Y. Polymyxin B-lipid interactions in Langmuir-Blodgett monolayers of *Escherichia coli* lipids: A thermodynamic and atomic force microscopy study. *Biopolymers* **2004**, *75*, 480–490. https://doi.org/10.1002/bip.20165

Cooper, J.B.; Aust, J.; Stellman, C.; Chike, K.; Myrick, M.L.; Schwartz, R.; Longmire, M. Raman spectroscopy with a low-cost imaging CCD array. *Spectrochim. Acta A Mol. Spectrosc.* **1994**, *50*, 567–575. https://doi.org/10.1016/0584-8539(94)80169-X

Dana, K.; Shende, C.; Huang, H.; Farquharson, S. Rapid analysis of cocaine in saliva by surface-enhanced Raman spectroscopy. *J. Anal. Bioanal. Tech.* **2015**, *6*, 1000289. https://doi.org/10.4172/2155-9872.1000289

Davies, J.K.; Rideal, E.K. *Interfacial Phenomena*; Academic Press: New York and London, 1961.

De, A.K.; Chowdhury, P.P.; Chattapadhyay, S. Quantitative analysis of resorcinol from marketed hair tonic using liquid chromatographic technique. *Int. Sch. Res. Notices* **2014**, *2014*, 632591. https://doi.org/10.1155/2014/632591

De, T.; Chettoor, A.M.; Agarwal, P.; Salapaka, M.V.; Nettikadan, S. Immobilization method of yeast cells for intermittent contact mode imaging using the atomic force microscope. *Ultramicroscopy* **2010**, *110* (3), 254–258. https://doi.org/10.1016/j.ultramic.2009.12.003

Debnath, R.; Saha, T. An insight into the production strategies and applications of the ligninolytic enzyme laccase from bacteria and fungi. *Biocatal. Agric. Biotechnol.* **2020**, *26*, 101645. https://doi.org/10.1016/j.bcab.2020.101645

Delfino, I.; Diano, N.; Lepore, M. Advanced optical sensing of phenolic compounds for environmental applications. *Sensors* **2021**, *21*, 7563. https://doi.org/10.3390/s21227563

Delfino, I.; Lepore, M.; Tatè, R.; Portaccio, M. Preparation and characterization of Au nanoparticles for theranostic applications. *Conf. Proc. Sensors Appl.* **2014**. https://doi.org/10.3390/ecsa-1-g008

Delfino, I.; Viola, D.; Cerullo, G.; Lepore, M. Ultrafast excited-state charge-transfer dynamics in laccase type I copper site. *Biophys. Chem.* **2015**, *200–201*, 41–47. https://doi.org/10.1016/j.bpc.2015.03.003

Dencheva, N.; Oliveira, S.; Braz, G.; Getya, D.; Malfois, M.; Denchev, Z.; Gitsov, I. Magnetically responsive PA6 microparticles with immobilized laccase show high catalytic efficiency in the enzymatic treatment of catechol. *Catalysts* **2021**, *11*, 239. https://doi.org/10.3390/catal11020239

Deng, X.; Xiong, F.; Li, X.; Xiang, B.; Li, Z.; Wu, X.; Guo, P.; Li, X.; Li, Y.; Li, G.; Xiong, W.; Zeng, Z. Application of atomic force microscopy in cancer research. *J. Nanobiotechnol.* **2018**, *16*, 102. https://doi.org/10.1186/s12951-018-0428-0

Diagnostic anSERS Inc. (accessed on 15 April 2025); Available online: https://www.diagnosticansers.com/

Ding, S.-Y.; You, E.-M.; Tian, Z.-Q.; Moskovits, M. Electromagnetic theories of surface-enhanced Raman spectroscopy. *Chem. Soc. Rev.* **2017**, *46*, 4042–4076. https://doi.org/10.1039/C7CS00238F

du Plessis, A. Persistent degradation: Global water quality challenges and required actions. *One Earth* **2022**, *5* (2), 129–131. https://doi.org/10.1016/j.oneear.2022.01.005

Dufrêne, Y.; Ando, T.; Garcia, R.; Alsteens, D.; Martinez-Martin, D.; Engel, A.; Gerber, C.; Müller, D.J. Imaging modes of atomic force microscopy for application in molecular and cell biology. *Nat. Nanotechnol.* **2017**, *12*, 295–307. https://doi.org/10.1038/nnano.2017.45

Dufrene, Y.F.; Martinez-Martin, D.; Medalsy, I.; Alsteens, D.; Muller, D.J. Multiparametric imaging of biological systems by force-distance curve–based AFM. *Nat. Methods* **2013**, *10*, 847–854. https://doi.org/10.1038/nmeth.2602

Durazzo, A.; Caiazzo, E.; Lucarini, M.; Cicala, C.; Izzo, A.A.; Novellino, E.; Santini, A. Polyphenols: A concise overview on the chemistry, occurrence, and human health. *Phytother. Res.* **2019**, *33*, 2221–2243. DOI: 10.1002/ptr.6419

Dwivedi, U.N.; Singh, P.; Pandey, V.P.; Kumar, A. Structure–Function Relationship among bacterial, fungal, and plant laccases. *J. Mol. Catal. B Enzym.* **2011**, *68*, 117–128. https://doi.org/10.1016/j.molcatb.2010.11.002

Elderdfi, M.; Sikorski, A.F. Langmuir-monolayer methodologies for characterizing protein-lipid interactions. *Chem. Phys. Lipids* **2018**, *212*, 61–72. https://doi.org/10.1016/j.chemphyslip.2018.01.008

Errico, S.; Bianco, M.; Mita, L.; Migliaccio, M.; Rossi, S.; Nicolucci, C.; Menale, C.; Portaccio, M.; Gallo, P.; Mita, D.G.; Diano, N. Migration of Bisphenol A into canned tomatoes produced in Italy: Dependence on temperature and storage conditions. *Food Chem.* **2014**, *160*, 157–164. https://doi.org/10.1016/j.foodchem.2014.03.085

Escriba, P.V.; Gonzalez-Ros, J.M.; Goni, F.M.; Kinnunen, P.K.; Vigh, L.; Sanchez-Magraner, L.; Fernandez, A.M.; Busquets, X.; Horvath, I.; Barcelo-Coblijn, G. Membranes: A meeting point for lipids, proteins, and therapies. *J. Cell Mol. Med.* **2008**, *12*, 829–875. https://doi.org/10.1111/j.1582-4934.2008.00281.x

Eskandari, V.; Sahbafar, H.; Zeinalizad, L.; Hadi, A. A review of applications of surface-enhanced Raman spectroscopy laser for detection of biomaterials and a quick glance into its advances for COVID-19 investigations. *ISSS J. Micro Smart Syst.* **2022**, *11* (2), 363–382. https://doi.org/10.1007/s41683-022-00103-x

Evans, E. Probing the relation between force—lifetime—and chemistry in single molecular bonds. *Annu. Rev. Biophys. Biomol. Struct.* **2001**, *30*, 105–128. https://doi.org/10.1146/annurev.biophys.30.1.105

Facure, M.H.M.; Andre, R.S.; Cardoso, R.M.; Mercante, L.A.; Correa, D.S. Electrochemical and optical dual-mode detection of phenolic compounds using MnO2/GQD nanozyme. *Electrochim. Acta* **2023**, *441*, 141777. https://doi.org/10.1016/j.electacta.2022.141777

Fălămaș, A.; Rotaru, H.; Hedeșiu, M. Surface-enhanced Raman spectroscopy (SERS) investigations of saliva for oral cancer diagnosis. *Lasers Med. Sci.* **2020**, *35*, 1393–1401. https://doi.org/10.1007/s10103-020-02988-2

Fan, C.; Tang, Y.; Wang, J.; Wang, Y.; Xiong, F.; Zhang, S.; et al. Long non-coding RNA LOC284454 promotes migration and invasion of nasopharyngeal carcinoma via modulating the Rho/Rac signaling pathway. *Carcinogenesis* **2018**, *40* (2), 380–391. https://doi.org/10.1093/carcin/bgy143

Fleischmann, M.; Hendra, P.J.; McQuillan, A.J. Raman spectra of pyridine adsorbed at a silver electrode. *Chem. Phys. Lett.* **1974**, *26*, 163–166. https://doi.org/10.1016/0009-2614(74)85388-1

Frens, G. Controlled nucleation for the regulation of the particle size in monodisperse gold suspensions. *Nature Phys. Sci.* **1973**, *241*, 20–22. https://doi.org/10.1038/physci241020a0

Gami, A.A.; Shukor, M.Y.; Khalil, K.A.; Dahalan, F.A.; Khalid, A.; Ahmad, S.A. Phenol and its toxicity. *J. Environ. Microbiol. Toxicol.* **2014**, *2*, 11–24. https://doi.org/10.54987/jemat.v2i1.89

Ganesan, M.; Nagaraaj, P. Quantum dots as nanosensors for detection of toxics: A literature review. *Anal. Methods* **2020**, *12*, 4254–4275. https://doi.org/10.1039/D0AY01293A

Givaudan, A.; Effosse, A.; Faure, D.; Potier, P.; Bouillant, M.-L.; Bally, R. Polyphenol oxidase in *Azospirillum Lipoferum* isolated from rice rhizosphere: Evidence for laccase activity in non-

motile strains of *Azospirillum Lipoferum*. *FEMS Microbiol. Lett.* **1993**, *108*, 205–210. https://doi.org/10.1111/j.1574-6968.1993.tb06100.x

Grieshaber, D.; MacKenzie, R.; Voros, J.; Reimhult, E. Electrochemical biosensors: Sensor principles and architectures. *Sensors* **2008**, *8*, 1400–1458. https://doi.org/10.3390/s80314000

Gryczynski, Z.; Gryczynski, I. *Practical Fluorescence Spectroscopy* (1st ed.); CRC Press: Boca Raton, FL, **2019**. https://doi.org/10.1201/9781315374758

Guo, Y.; Liu, C.; Ye, R.; Duan, Q. Advances on water quality detection by UV-Vis spectroscopy. *Appl. Sci.* **2020**, *10*, 6874. https://doi.org/10.3390/app10196874

Guzmán, E.; Liggieri, L.; Santini, E.; Ferrari, M.; Ravera, F. DPPC–DOPC Langmuir monolayers modified by hydrophilic silica nanoparticles: Phase behaviour, structure and rheology. *Colloids Surf. A Physicochem. Eng. Aspects* **2012**, *413*, 174–183. https://doi.org/10.1016/j.colsurfa.2011.12.059

Guzmán, E.; Liggieri, L.; Santini, E.; Ferrari, M.; Ravera, F. Mixed DPPC–cholesterol Langmuir monolayers in presence of hydrophilic silica nanoparticles. *Colloids Surf. B Biointerfaces* **2013**, *105*, 284–293. https://doi.org/10.1016/j.colsurfb.2013.01.020

Hachiya, M.; Asanome, N.; Goto, T.; Noda, T. Fluorescence imaging with UV-excitation for evaluating freshness of rice. *Jpn. Agric. Res. Q.* **2009**, *43*, 193–198. https://doi.org/10.6090/jarq.43.193

Haiss, W.; Thanh, N.T.K.; Aveyard, J.; Ferni, D.G. Determination of size and concentration of gold nanoparticles from UV-Vis spectra. *Anal. Chem.* **2007**, *79*, 4215–4221. https://doi.org/10.1021/ac0702084

Hansma, H.G.; Vesenka, J.; Siegerist, C.; Kelderman, G.; Morrett, H.; Sinsheimer, R.L.; Elings, V.; Bustamante, C.; Hansma, P.K. Reproducible imaging and dissection of plasmid DNA under liquid with the atomic force microscope. *Science* **1992**, *256*, 1180–1184. https://doi.org/10.1126/science.256.5060.1180

Helmy, Q.; Kardena, E. Petroleum oil and gas industry waste treatment: A common practice in Indonesia. *J. Pet. Environ. Biotechnol.* **2015**, *6*, 1. https://doi.org/10.4172/2157-7463.1000241

Hoan, B.T.; Thanh, T.T.; Tam, P.D.; Trung, N.N.; Cho, S.; Pham, V.H. A green luminescence of lemon derived carbon quantum dots and their applications for sensing of V5+ ions. *Mater. Sci. Eng. B Adv.* **2019**, *251*, 114455. DOI: 10.1016/j.mseb.2019.114455

Hoegger, P.J.; Kilaru, S.; James, T.Y.; Thacker, J.R.; Kues, U. Phylogenetic comparison and classification of laccase and related multicopper oxidase protein sequences. *FEBS J.* **2006**, *273*, 2308–2326. https://doi.org/10.1111/j.1742-4658.2006.05247.x

Hong-Wei, W.; et al. Determination of resorcinol and phloroglucinol in environmental water samples using ion chromatography with chemiluminescence detection. *Chinese J. Anal. Chem.* **2012**. https://doi.org/10.1016/S1872-2040(11)60588-4

Horiba Scientific. *Available online: http://www.horiba.com/us/en/scientific/products/raman-spectroscopy/accessories/sers-substrates/* (accessed on 15 April 2025).

Hossain, S.; Satter, S.; Kwon, T.-H.; Kim, K.-D. Optical measurement of molar absorption coefficient of HbA1c: Comparison of theoretical and experimental results. *Sensors* **2022**, *22*, 8179. https://doi.org/10.3390/s22218179

Hughes, A.V.; Howse, J.R.; Dabkowska, A.; Jones, R.A.; Lawrence, M.J.; Roser, S.J. Floating lipid bilayers deposited on chemically grafted phosphatidylcholine surfaces. *Langmuir* **2008**, *24*, 1989–1999. https://doi.org/10.1021/la702050b

IARC: Some fumigants, the herbicides 2,4-D and 2,4,5-T, chlorinated dibenzodioxins and miscellaneous industrial chemicals; In *IARC Monographs on the Evaluation of the Carcinogenic Risk of Chemicals to Humans*; IARC: Lyon, France, 1977; pp. 155–175.

İyigündoğdu, I.; Üstündağ, A.; Duydu, Y. Toxicological evaluation of bisphenol A and its analogues. *Turk. J. Pharm. Sci.* **2020**, *17* (4), 457–462. https://doi.org/10.4274/tjps.galenos.2019.58219

Jalili, N.; Laxminarayana, K. A review of atomic force microscopy imaging systems: Application to molecular metrology and biological sciences. *Mechatronics* **2004**, *14*, 907–945. https://doi.org/10.1016/j.mechatronics.2004.04.005

Janusz, G.; Pawlik, A.; Świderska-Burek, U.; Polak, J.; Sulej, J.; Jarosz-Wilkołazka, A.; Paszczyński, A. Laccase properties, physiological functions, and evolution. *Int. J. Mol. Sci.* **2020**, *21*, 966. https://doi.org/10.3390/ijms21030966

Jeanmaire, D.L.; Van Duyne, R.P. Surface Raman spectroelectrochemistry. Part I. Heterocyclic, aromatic, and aliphatic amines adsorbed on the anodized silver electrode. *J. Electroanal. Chem. Interfacial Electrochem.* **1977**, *84*, 1–20. https://doi.org/10.1016/S0022-0728(77)80224-6

Jia, Y.; Liu, B.; Cheng, D.; Li, J.; Huang, F.; Lu, Y. Dyeing characteristics and functionality of tussah silk fabric with oak bark extract. *Text. Res. J.* **2017**, *87*, 1806–1817. https://doi.org/10.1177/0040517516659378

Kaganer, V.M.; Möhwald, H.; Dutta, P. Structure and phase transitions in Langmuir monolayers. *Rev. Mod. Phys.* **1999**, *71*, 779–819. https://doi.org/10.1103/RevModPhys.71.779

Karaki, N.; Aljawish, A.; Muniglia, L.; Bouguet-Bonnet, S.; Leclerc, S.; Paris, C.; Jasniewski, J.; Humeau-Virot, C. Functionalization of pectin with laccase-mediated oxidation products of ferulic acid. *Enzym. Microb. Technol.* **2017**, *104*, 1–8. https://doi.org/10.1016/j.enzmictec.2017.05.001

Karami, C.; Taher, M.A. A catechol biosensor based on immobilizing laccase to Fe3O4@Au core-shell nanoparticles. *Int. J. Biol. Macromol.* **2019**, *129*, 84–90. https://doi.org/10.1016/j.ijbiomac.2019.02.015

Karoui, R. Chapter 7 - Spectroscopic Technique: Fluorescence and Ultraviolet-Visible (UV-Vis) Spectroscopies. In *Modern Techniques for Food Authentication* (Second Edition); Elsevier: 2018; pp. 219–252. https://doi.org/10.1016/B978-0-12-814264-6.00007-4

Karoui, R.; Blecker, C. Fluorescence spectroscopy measurement for quality assessment of food systems—a review. *Food Bioprocess Technol.* **2011**, *4*, 364–386. https://doi.org/10.1007/s11947-010-0370-0

Katata, V.M.; Maximino, M.D.; Silva, C.Y.; Alessio, P. The role of cholesterol in the interaction of the lipid monolayer with the endocrine disruptor bisphenol-A. *Membranes* **2022**, *12*, 729. https://doi.org/10.3390/membranes12080729

Kergomard, J.; Carrière, F.; Paboeuf, G.; Artzner, F.; Barouh, N.; Bourlieu, C.; Vié, V. Interfacial organization and phase behavior of mixed galactolipid-DPPC-phytosterol assemblies at the air-water interface and in hydrated mesophases. *Colloids Surf. B Biointerfaces* **2022**, *217*, 112646. https://doi.org/10.1016/j.colsurfb.2022.112646

Khairy, G.M.; Ali, E.I.; Saad, E.M. Development of an optical sensor for the determination of phenolic compounds in environmental samples. *Anal. Methods* **2023**, *15*, 6425–6434. https://doi.org/10.1039/D3AY01699D

Kim, J.; Jang, Y.; Kim, N.-J.; Kim, H.; Yi, G.-C.; Shin, Y.; Kim, M.H.; Yoon, S. Study of chemical enhancement mechanism in non-plasmonic surface enhanced Raman spectroscopy (SERS). *Front Chem.* **2019**, *7*, 582. https://doi.org/10.3389/fchem.2019.00582

Klotz, I.M. Ultraviolet absorption spectroscopy. *Journal of Chemical Education* **1945**, *22(7)*, 328. https://doi.org/10.1021/ed022p328

Komori, H.; Higuchi, Y. Structure and molecular evolution of multicopper blue proteins. *Biomol. Concepts* **2010**, *1*, 31–40. https://doi.org/10.1515/bmc.2010.004

Krieg, M.; Fläschner, G.; Alsteens, D.; Gaub, B.M.; Roos, W.H.; Wuite, G.J.L.; Gaub, H.E.; Gerber, C.; Dufrêne, Y.F.; Müller, D.J. Atomic force microscopy-based mechanobiology. *Nat. Rev. Phys.* **2019**, *1*, 41–57. https://doi.org/10.1038/s42254-018-0001-7

Kumar, R.; Tripathi, T.; Saudagar, P. Fluorescence spectroscopy-based methods to study protein folding dynamics. In: Saudagar, P., Tripathi, T. (Eds.) *Protein Folding Dynamics and Stability*; Springer: Singapore, 2023. https://doi.org/10.1007/978-981-99-2079-2_2

Lakowicz, J.R. *Principles of Fluorescence Spectroscopy*, 3rd ed.; Springer: Baltimore, Maryland, 2006.

Langer, J.; Jimenez de Aberasturi, D.; Aizpurua, J.; Alvarez-Puebla, R.A.; Auguié, B.; Baumberg, J.J.; Bazan, G.C.; Bell, S.E.J.; Boisen, A.; Brolo, A.G.; Choo, J.; Cialla-May, D.; Deckert, V.; Fabris, L.; Faulds, K.; García de Abajo, F.J.; Goodacre, R.; Graham, D.; Haes, A.J.; Haynes, C.L.; Huck, C.; Itoh, T.; Käll, M.; Kneipp, J.; Kotov, N.A.; Kuang, H.; Le Ru, E.C.; Lee, H.K.; Li, J.F.; Ling, X.Y.; Maier, S.A.; Mayerhöfer, T.; Moskovits, M.; Murakoshi, K.; Nam, J.M.; Nie, S.; Ozaki, Y.; Pastoriza-Santos, I.; Perez-Juste, J.; Popp, J.; Pucci, A.; Reich, S.; Ren, B.; Schatz, G.C.; Shegai, T.; Schlücker, S.; Tay, L.L.; Thomas, K.G.; Tian, Z.Q.; Van Duyne, R.P.; Vo-Dinh, T.; Wang, Y.; Willets, K.A.; Xu, C.; Xu, H.; Xu, Y.; Yamamoto, Y.S.; Zhao, B.; Liz-Marzán, L.M. Present and future of surface-enhanced Raman scattering. *ACS Nano* **2020**, *14*, 28–117. https://doi.org/10.1021/acsnano.9b04224

Langmuir, I. The constitution and fundamental properties of solids and liquids. II. Liquids. *J. Am. Chem. Soc.* **1917**, *39*, 9, 1848–1906. https://doi.org/10.1021/ja02254a006

Leite, F.L.; Mattoso, L.H.C.; Oliveira Jr, O.N.; Herrmann Jr., P.S.P. The atomic force spectroscopy as a tool to investigate surface forces: Basic principles and applications. In *Modern Research and Educational Topics in Microscopy*; A. Méndez-Vilas and J. Díaz, Eds.; Formatex: Badajoz, Spain, **2007**.

Leite, F.L.; Paterno, L.G.; Borato, C.E.; Herrmann, P.S.P.; Oliveira, O.N.; Mattoso, L.H.C. Study on the adsorption of poly(o-ethoxyaniline) nanostructured films using atomic force microscopy. *Polymer* **2005**, *46*, 12503. https://doi.org/10.1016/j.polymer.2005.07.108

Leonenko, Z.V.; Finot, E.; Ma, H.; Dahms, T.E.; Cramb, D.T. Investigation of temperature-induced phase transitions in DOPC and DPPC phospholipid bilayers using temperature-controlled scanning force microscopy. *Biophys. J.* **2004**, *86*, 3783–3793. https://doi.org/10.1529/biophysj.103.036681

Lepore, M.; Delfino, I. Optical sensors technology and applications. *Sensors* **2022**, *22*, 7905. https://doi.org/10.3390/s22207905

Lepore, M.; Portaccio, M. Optical detection of different phenolic compounds by means of a novel biosensor based on sol-gel immobilized laccase. *Biotechnol. Appl. Biochem.* **2017**. https://doi.org/10.1002/bab.1551

Lin, C.H.; Sheu, J.Y.; Wu, H.L.; Huang, Y.L. Determination of hydroquinone in cosmetic emulsion using microdialysis sampling coupled with high-performance liquid chromatography. *J. Pharm. Biomed. Anal.* **2005**, *38*, 414–419. https://doi.org/10.1016/j.jpba.2005.01.031

Lin, L.; Yang, H.; Xu, X. Effects of water pollution on human health and disease heterogeneity: a review. *Front. Environ. Sci.* **2022**, *10*, 880246. https://doi.org/10.3389/fenvs.2022.880246

Liu, J.; Conboy, J.C. Structure of a gel phase lipid bilayer prepared by the Langmuir-Blodgett/Langmuir-Schaefer method characterized by sum-frequency vibrational spectroscopy. *Langmuir* **2005**, *21*, 9091–9097. https://doi.org/10.1021/la051500e

Liu, J.; Qin, L.; Zhang, T.; Li, X.; Kang, S.Z. Al plate supported Mxene films modified with Ag nanoparticles: Highly sensitive and disposable SERS substrate for trace catechol in seawater. *Appl. Surf. Sci.* **2023**, *628*, 157288. https://doi.org/10.1016/j.apsusc.2023.157288

Liu, K.; Zhao, Q.; Li, B.; Zhao, X. Raman spectroscopy: A novel technology for gastric cancer diagnosis. *Front. Bioeng. Biotechnol.* **2022**, *10*, 85659. https://doi.org/10.3389/fbioe.2022.856591

Liu, Y.; Zhang, Y.; Tardivel, M.; Lequeux, M.; Xueping, C.; Liu, W.; Huang, J.; Huiyan, T.; Liu, Q.; Huang, G.; Gillibert, R.; Lamy de la Chapelle, M.; Fu, W. Evaluation of the reliability of six commercial SERS substrates. *Plasmonics* **2020**, *15*, 743–752. https://doi.org/10.1007/s11468-019-01084-8

Loi, M.; Glazunova, O.; Fedorova, T.; Logrieco, A.F.; Mulè, G. Fungal laccases: The forefront of enzymes for sustainability. *J. Fungi* **2021**, *7*, 1048. https://doi.org/10.3390/jof7121048

Mainali, K. Phenolic compounds contaminants in water: A glance. *Curr. Trends Civ. Struct. Eng.* **2020**, *4*, 1–3. https://doi.org/10.33552/CTCSE.2020.04.000593

Manavalan, A.; Manavalan, T.; Murugesan, K.; Kutzner, A.; Thangavelu, K.P.; Heese, K. Characterization of a solvent, surfactant, and temperature-tolerant laccase from *Pleurotus* sp. MAK-II and its dye decolorizing property. *Biotechnol. Lett.* **2015**, *37*, 2403–2409. https://doi.org/10.1007/s10529-015-1937-7

Marian, C.M. Understanding and controlling intersystem crossing in molecules. *Annu. Rev. Phys. Chem.* **2021**, *72*, 617–640. https://doi.org/10.1146/annurev-physchem-061020-053433

Mark, R.; Lyu, X.; Lee, J.J.L.; Parra-Saldívar, R.; Chen, W.N. Sustainable production of natural phenolics for functional food applications. *J. Funct. Foods* **2019**, *57*, 233–254. https://doi.org/10.1016/j.jff.2019.03.016

Marrubini, G.; Calleri, E.; Coccini, T.; Castoldi, A.F.; Manzo, L. Direct analysis of phenol, catechol, and hydroquinone in human urine by coupled-column HPLC with fluorimetric detection. *Chromatographia* **2005**, *62*, 25–30. https://doi.org/10.1365/s10337-005-0570-3

Martin, A.R. Spectroscopic methods in biology, with application to neurophysiology. *Advances in Biological and Medical Physics* **1973**, *14*, 225-284. https://doi.org/10.1016/B978-0-12-005214-1.50009-1

Matousek, P.; Morris, D.M. Emerging Raman Applications and Techniques in Biomedical and Pharmaceutical Fields, Vol. 1. In *Emerging Raman Applications and Techniques in Biomedical and Pharmaceutical Fields*; Matousek, P., Morris, M.D., Eds.; Springer: Berlin, Germany, 2010; pp. 1–24. https://doi.org/10.1007/978-3-642-02649-2

Maver, U.; Velnar, T.; Gaberšček, M.; Planinšek, O.; Finšgar, M. Recent progressive use of atomic force microscopy in biomedical applications. *TrAC Trends Anal. Chem.* **2016**, *80*, 96–111. https://doi.org/10.1016/j.trac.2016.03.014

Maximino, M.D.; Martin, C.S.; Aléssio, P. Bisphenol A exposure induces multiple effects in DOPC membrane models. *J. Mol. Liq.* **2022**, *359*, 119253. https://doi.org/10.1016/j.molliq.2022.119253

Maximino, M.D.; Silva, C.Y.; Cavalcante, D.G.S.M.; Martin, C.S.; Job, A.E.; Oliveira, O.N.; Aléssio, P. Consequences of the exposure to bisphenol A in cell membrane models at the molecular level and hamster ovary cells viability. *Colloids Surf. B Biointerfaces* **2021**, *203*, 111762. https://doi.org/10.1016/j.colsurfb.2021.111762

Mehrzad-Samarin, M.; Faridbod, F.; Dezfuli, A.S.; Ganjali, M.R. A novel metronidazole fluorescent nanosensor based on graphene quantum dots embedded silica molecularly imprinted polymer. *Biosens. Bioelectron.* **2017**, *92*, 618–623. https://doi.org/10.1016/j.bios.2016.10.047

Mesophotonics. *SERS Central*. [Accessed on 15 April 2025]. Available online: http://www.mesophotonics.com/sers_central/index.html

Mita, L.; Bianco, M.; Viggiano, E.; Zollo, F.; Bencivenga, U.; Sica, V.; Monaco, G.; Portaccio, M.; Diano, N.; Colonna, A.; Lepore, M.; Canciglia, P.; Mita, D.G. Bisphenol A content in fish caught in two different sites of the Tyrrhenian Sea (Italy). *Chemosphere* **2011**, *82*, 405–410. https://doi.org/10.1016/j.chemosphere.2010.09.071

Mokra, K.; Kuźmińska-Surowaniec, A.; Woźniak, K.; Michałowicz, J. Evaluation of DNA-damaging potential of bisphenol A and its selected analogs in human peripheral blood mononuclear cells (in vitro study). *Food Chem. Toxicol.* **2017**, *100*, 62–69. https://doi.org/10.1016/j.fct.2016.12.003

Momin, A.; Kondo, N.; Al Riza, D.F.; Ogawa, Y.; Obenland, D. A methodological review of fluorescence imaging for quality assessment of agricultural products. *Agriculture* **2023**, *13*, 1433. https://doi.org/10.3390/agriculture13071433

Morash, M.G.; Soanes, K.H.; Achenbach, J.C.; Ellis, L.D. Assessing the morphological and behavioral toxicity of catechol using larval zebrafish. *Int. J. Mol. Sci.* **2022**, *23*, 7985. https://doi.org/10.3390/ijms23147985

Morita, S.; Giessibl, F.J.; Meyer, E.; Wiesendanger, R. (Eds.) *Noncontact Atomic Force Microscopy: Volume 3*; Springer: Berlin, Germany, 2015.

Morris, V.J. Biological applications of scanning probe microscopies. *Prog. Biophys. Mol. Biol.* **1994**, *61*(2), 131–185. https://doi.org/10.1016/0079-6107(94)90008-6

Moshtaghioun, S.M.; Haghbeen, K.; Sahebghadam, A.L.; Legge, R.L.; Khoshneviszadeh, R.; Farhadi, S. Direct spectrophotometric assay of laccase using diazo derivatives of guaiacol. *Anal. Chem.* **2011**, *83*, 4200–4205. https://doi.org/10.1021/ac200501w

Mosier-Boss, P.A. Review of SERS substrates for chemical sensing. *Nanomaterials* **2017**, *7*, 142. https://doi.org/10.3390/nano7060142

Mosiewicki, M.A.; Schroeder, W.F.; Leite, F.L.; Hermann, P.S.P.; Curvelo, A.A.S.; Aranguren, M.I.; Borrajo, J. AFM fracture surface study of vinylester and unsaturated polyester-based thermosets. *J. Mater. Sci.* **2006**, *41*, 6154. https://doi.org/10.1007/s10853-006-0163-z

Moskovits, M. Surface roughness and the enhanced intensity of Raman scattering by molecules adsorbed on metals. *J. Chem. Phys.* **1978**, *69*, 4159. https://doi.org/10.1063/1.437095

Mou, J.; Yang, J.; Shao, Z. Atomic force microscopy of cholera toxin B-oligomers bound to bilayers of biologically relevant lipids. *J. Mol. Biol.* **1995**, *248*, 507–512. https://doi.org/10.1006/jmbi.1995.0238

Müller, A.; Marschall, S.; Jensen, O.B.; Fricke, J.; Wenzel, H.; Sumpf, B.; Andersen, P.E. Diode laser based light sources for biomedical applications. *Laser Photonics Rev.* **2013**, *7*, 605–627. https://doi.org/10.1002/lpor.201200051

Muller, D.J.; Dufrene, Y.F. Atomic force microscopy as a multifunctional molecular toolbox in nanobiotechnology. *Nat. Nanotechnol.* **2008**, *3*, 261–269. https://doi.org/10.1038/nnano.2008.100

Muller, D.J.; Dufrene, Y.F. Atomic force microscopy: A nanoscopic window on the cell surface. *Trends Cell Biol.* **2011**, *21*, 461–469. https://doi.org/10.1016/j.tcb.2011.04.008

Naresh, V.; Lee, N. A review on biosensors and recent development of nanostructured materials-enabled biosensors. *Sensors* **2021**, *21*, 1109. https://doi.org/10.3390/s21041109

Nezhad, M.R.H.; Alimohammadi, M.; Tashkhourian, J.; Razavian, S.M. Optical detection of phenolic compounds based on the surface plasmon resonance band of Au nanoparticles. *Spectrochim. Acta Part A Mol. Biomol. Spectrosc.* **2008**, *71*, 199–203. https://doi.org/10.1016/j.saa.2008.03.016

Nijegorodov, N.; Ramachandran, V.; Winkoun, D.P. The dependence of the absorption and fluorescence parameters, the intersystem crossing and internal conversion rate constants, on the number of rings in polyacene molecules. *Spectrochim. Acta Part A Mol. Biomol. Spectrosc.* **1997**, *53*, 1813–1824. https://doi.org/10.1016/S1386-1425(97)00071-1

Nilapwar, S.N.; Nardelli, M.; Westerhoff, H.V.; Verma, M. Absorption spectroscopy. In *Methods in Enzymology*; Elsevier: Amsterdam, The Netherlands, 2011; Volume 500. https://doi.org/10.1016/B978-0-12-385118-5.00004-9

Ocean Optics. *SERS*. [Accessed on 15 April 2025]. Available online: https://oceanoptics.com/product/sers/

Olasz, A.; Mignon, P.; De Proft, F.; Veszprémi, T.; Geerlings, P. Effect of the π-π stacking interaction on the acidity of phenol. *Chem. Phys. Lett.* **2005**, *407*, 504–509. https://doi.org/10.1016/j.cplett.2005.03.145

Ondavia. [Accessed on 15 April 2025]. Available online: https://www.ondavia.com/about

Oshina, I.; Spigulis, J. Beer-Lambert law for optical tissue diagnostics: current state of the art and the main limitations. *J Biomed Opt.* **2021**, *26*(10), 100901. https://doi.org/10.1117/1.JBO.26.10.100901

Pan, T.T.; Sun, D.W.; Paliwal, J.; Pu, H.; Wei, Q. New method for accurate determination of polyphenol oxidase activity based on reduction in SERS intensity of catechol. *J. Agric. Food Chem.* **2018**, *66*, 11180–11187. https://doi.org/10.1021/acs.jafc.8b03985

Pasteris, J.D.; Beyssac, O. Welcome to Raman spectroscopy: Successes, challenges, and pitfalls. *Elements* **2020**, *16*, 87–92. https://doi.org/10.2138/gselements.16.2.87

Patel, S.; Raulji, A.; Patel, D.; Panchal, D.; Dalwadi, M.; Upadhyay, U. A review on UV visible spectroscopy. *Int. J. Pharm. Res. Appl.* **2022**, *7*, 1144–1151. https://doi.org/10.35629/7781-070511441151

Peetla, C.; Andrew, S.; Vinod, L. Biophysical interactions with model lipid membranes: Applications in drug discovery and drug delivery. *Mol. Pharmaceutics* **2009**, *6*, 1264–1276. https://doi.org/10.1021/mp9000662

Penner, M.H. Basic principles of spectroscopy. In *Food Analysis*; Nielsen, S.S., Ed.; Springer: Cham, Switzerland, 2017. https://doi.org/10.1007/978-3-319-45776-5_6

Philpott, M.R. Effect of surface plasmons on transitions in molecules. *J. Chem. Phys.* **1975**, *62*, 1812. https://doi.org/10.1063/1.430708

Pilot, R.; Signorini, R.; Fabris, L. Surface-enhanced Raman spectroscopy: Principles, substrates, and applications. In *Metal Nanoparticles and Clusters*; Deepak, F., Ed.; Springer: Berlin/Heidelberg, Germany, 2018.

Piontek, K.; Antorini, M.; Choinowski, T. Crystal structure of a laccase from the fungus *Trametes versicolor* at 1.90-Å resolution containing a full complement of coppers. *J. Biol. Chem.* **2002**, *277*, 37663–37669. https://doi.org/10.1074/jbc.M204571200

Portaccio, M.; Della Ventura, B.; Mita, D.G.; Manolova, N.; Stoilova, O.; Rashkov, I. and Lepore, M. FT-IR microscopy characterization of sol–gel layers prior and after glucose oxidase immobilization for biosensing applications. *J. Sol-Gel Sci. Technol.* **2011**, *57*, 204–211. https://doi.org/10.1007/s10971-010-2343-1

Portaccio, M.; Di Martino, S.; Maiuri, P.; Durante, D.; De Luca, P.; Lepore, M.; Bencivenga, U.; Rossi, S.; De Maio, A.; Mita, D.G. Biosensors for phenolic compounds: The catechol as a

substrate model. *J. Mol. Catal. B: Enzym.* **2006**, *41*, 97–102. https://doi.org/10.1016/j.molcatb.2006.05.002

Pradeep, N.; Anupama, S.; Navya, K.; Shalini, H.; Idris, M.; Hampannavar, U. Biological removal of phenol from wastewaters: A mini review. *Appl. Water Sci.* **2015**, *5*, 105–112. https://doi.org/10.1007/s13201-014-0176-8

Priority Substances and Certain Other Pollutants according to Annex II of Directive 2008/105/EC. European Commission. [Accessed on 15 April 2025]. Available online: http://data.europa.eu/eli/dir/2008/105/2013-09-13

Qu, X.; Tian, M.; Liao, B.; Chen, A. Enhanced electrochemical treatment of phenolic pollutants by an effective adsorption and release process. *Electrochim. Acta* **2010**, *55*, 5367–5374. https://doi.org/10.1016/j.electacta.2010.04.089

Radmacher, M.; Tillmann, R.W.; Fritz, M.; Gaub, H.E. From molecules to cells: Imaging soft samples with the atomic force microscope. *Science* **1992**, *257*, 1900–1905. https://doi.org/10.1126/science.1411505

Raff, R.; Ettling, B.V. Hydroquinone, resorcinol and pyrocatechol, 2nd ed.; In *Encyclopedia of Chemical Technology*; Kirk, R.E., Othmer, D.F., Eds.; Wiley: New York, 1966; pp. 462–492.

Rahmani, M.; Taugeron, P.; Rousseau, A.; Delorme, N.; Douillard, L.; Duponchel, L.; Bardeau, J.F. Highlight on commercial SERS substrates and on optimized nanorough large-area SERS-based sensors: A Raman study. *Appl. Nanoscience* **2023**, *14*, 2013–2015. https://doi.org/10.1007/s13204-023-02972-6

Raj, S.; Alice Alex, A.K. Paulose, S. Shareef, S.K. Sugunan, G. George, L.A. Pothan. Chapter 3 - Spectroscopic and microscopic analysis of biodegradable and biocompatible polymer nanocomposites. In *Biodegradable and Biocompatible Polymer Nanocomposites*; Elsevier: Amsterdam, Netherlands, 2023; pp. 69–112. https://doi.org/10.1016/B978-0-323-91696-7.00013-1

Raman, C.V.; Krishnan, K.S. A new type of secondary radiation. *Nature* **1928**, *121*, 501–502. https://doi.org/10.1038/121501c0

Ramos, R.L.; Moreira, V.R.; Lebron, Y.A.R.; Santos, A.V.; Santos, L.V.S.; Amaral, M.C.S. Phenolic compounds seasonal occurrence and risk assessment in surface and treated waters in Minas Gerais-Brazil. *Environ. Pollut.* **2021**, *268*, 115782. https://doi.org/10.1016/j.envpol.2020.115782

Rodionov, P.V.; Veselova, I.A.; Shekhovtsova, T.N. Optical sensors for determining phenolic compounds with different structures. *J. Anal. Chem.* **2013**, *68*, 931–941. https://doi.org/10.1134/S1061934813110130

Rodríguez-Delgado, M.M.; Alemán-Nava, G.S.; Rodríguez-Delgado, J.M.; Dieck-Assad, G.; Martínez-Chapa, S.O.; Barceló, D.; Parra, R. Laccase-based biosensors for detection of phenolic compounds. *TrAC-Trends Anal. Chem.* **2015**, *74*, 21–45. https://doi.org/10.1016/j.trac.2015.05.008

Rojewska, M.; Smułek, W.; Kaczorek, E.; Prochaska, K. Langmuir monolayer techniques for the investigation of model bacterial membranes and antibiotic biodegradation mechanisms. *Membranes* **2021**, *11*, 707. https://doi.org/10.3390/membranes11090707

Romero-Arcos, M.; Garnica-Romo, M.G.; Martinez-Flores, H.E.; Vázquez-Marrufo, G.; Ramirez-Bon, R.; González-Hernández, J.; Barbosa-Cánovas, G.V. Enzyme immobilization by amperometric biosensors with TiO2 nanoparticles used to detect phenol compounds. *Food Eng. Rev.* **2016**, *8*, 235–250. https://doi.org/10.1007/s12393-015-9129-8

Rostron, R.; Gaber, S.; Gaber, D. Raman spectroscopy, review. *Int. J. Eng. Technol. Res.* **2016**, *6*, 1–5.

Ruiz, G.C.M.; Cruz, M.A.E.; Faria, A.N.; Zancanela, D.C.; Ciancaglini, P.; Ramos, A.P. Biomimetic collagen/phospholipid coatings improve formation of hydroxyapatite nanoparticles on titanium. *Mater. Sci. Eng. C* **2017**, *77*, 102–110. https://doi.org/10.1016/j.msec.2017.03.204

Ruiz, G.C.M.; Pazin, W.M.; do Carmo Morato, L.F.; Oliveira, O.N.; Constantino, C.J.L. Correlating mono- and bilayers of lipids to investigate the pronounced effects of steroid hormone 17_-ethynylestradiol on membrane models of DPPC/cholesterol. *J. Mol. Liq.* **2020**, *311*, 113324. https://doi.org/10.1016/j.molliq.2020.113324

Ryabchykov, O.; Guo, S.; Bocklitz, T. Analyzing Raman spectroscopic data. *Phys. Sci. Rev.* **2019**, *4*, 20170043. https://doi.org/10.1515/psr-2017-0043

Salehi, S.; Abdollahi, K.; Panahi, R.; Rahmanian, N.; Shakeri, M.; Mokhtarani, B. Applications of biocatalysts for sustainable oxidation of phenolic pollutants: A review. *Sustainability* **2021**, *13*, 8620. https://doi.org/10.3390/su13158620

Sanchez-Cortes, S.; Francioso, O.; Garcia-Ramos, J.V.; Ciavatta, C.; Gessa, C. Adsorption and chemical modification of phenols on a silver surface. *J. Colloid Interface Sci.* **2000**, *231*, 98–106. https://doi.org/10.1006/jcis.2000.7101

Sanz, J.; de Marcos, S.; Galbán, J. Autoindicating optical properties of laccase as the base of an optical biosensor film for phenol determination. *Anal. Bioanal. Chem.* **2012**, *404*, 351–359. https://doi.org/10.1007/s00216-012-6061-0

Saoudi, O.; Ghaouar, N.; Othman, T. Fluorescence study of laccase from *Trametes versicolor* under the effects of pH, chemical denaturants and ionic liquids. *J. Mol. Liq.* **2017**, *225*, 56–63. https://doi.org/10.1016/j.molliq.2016.11.050

Savitzky, A.; Golay, M.J.E. Smoothing and differentiation of data by simplified least squares procedures. *Anal. Chem.* **1964**, *36*, 1627–1639. https://doi.org/10.1021/ac60214a047

Schweigert, N.; Zehnder, A.J.B.; Eggen, R.I.L. Chemical properties of catechols and their molecular modes of toxic action in cells, from microorganisms to mammals. *Environ. Microbiol.* **2001**, *3*, 81–91. https://doi.org/10.1046/j.1462-2920.2001.00176.x

Seifert, J.; Rheinlaender, J.; Novak, P.; Korchev, Y.E.; Schaffer, T.E. Comparison of atomic force microscopy and scanning ion conductance microscopy for live cell imaging. *Langmuir* **2015**, *31*, 6807–6813. https://doi.org/10.1021/acs.langmuir.5b01124

SERSitive. [(accessed on 15 April 2025)]; Available online: https://sersitive.eu/about-substrates/

Shi, R.; Liu, X.; Ying, Y. Facing challenges in real-life application of surface-enhanced Raman scattering: Design and nanofabrication of surface-enhanced Raman scattering substrates for rapid field test of food contaminants. *J. Agric. Food Chem.* **2018**, *66*, 6525–6543. https://doi.org/10.1021/acs.jafc.7b03075

Shinde, G.; Godage, R.K.; Jadhav, R.S.; Barhate, M.; Bhagwat, A. A review on advances in UV spectroscopy. *Res. J. Sci. Tech.* **2020**, *12*(1), 47–51. https://doi.org/10.5958/2349-2988.2020.00005.4

Shleev, S.V.; Morozova, O.V.; Nikitina, E.S.; Gorshina, T.V.; Rusinova, V.A.; Serezhenkov, D.S.; Burbaev, I.G.; Gazaryan, A.I.; Yaropolov, A.I. Comparison of physico-chemical characteristics of four laccases from different basidiomycetes. *Biochimie* **2004**, *86*, 693–703. https://doi.org/10.1016/j.biochi.2004.08.005

Silmeco ApS. [(accessed on 15 April 2025)]; Available online: https://silmeco.com/products/

Simkus, R.A.; Laurinavicius, V.; Boguslavsky, L.; Skotheim, T.; Tanenbaum, S.W.; Nakas, J.P.; Slomczynski, D.J. Laccase containing sol-gel based optical biosensors. *Anal. Lett.* **1996**, *29*(11), 1907–1919. https://doi.org/10.1080/00032719608000797

Singer, S.J.; Nicolson, G.L. The fluid mosaic model of the structure of cell membranes. *Science* **1972**, *175*, 720–731. DOI: 10.1126/science.175.4023.720

Sirghi, L.; Nakagiri, N.; Sugisaki, K.; Sugimura, H.; Takai, O. Analysis of atomic force curve data for mapping of surface properties in water. *Langmuir* **2000**, *16*, 7796. https://doi.org/10.1143/JJAP.40.1420

Soto, M.L.; Falqué, E.; Domínguez, H. Relevance of natural phenolics from grape and derivative products in the formulation of cosmetics. *Cosmetics* **2015**, *259–276*. https://doi.org/10.3390/cosmetics2030259

Sugihara, K.; Kumaki, J. Visualization of two-dimensional single chain conformations solubilized in a miscible polymer blend monolayer by atomic force microscopy. *J. Phys. Chem. B* **2012**, *116*(22), 6561–6568. https://doi.org/10.1021/jp303063c

Suresh, S.; Srivastava, V.C.; Mishra, I.M. Adsorption of catechol, resorcinol, hydroquinone, and their derivatives: A review. *Int. J. Energy Environ. Eng.* **2012**, *3*(1), 32. https://doi.org/10.1186/2251-6832-3-32

Taofiq, O.; Heleno, S.A.; Calhelha, R.C.; Fernandes, I.P.; Alves, M.J.; Barros, L.; González-Paramás, A.M.; Ferreira, I.C.F.R.; Barreiro, M.F. Phenolic acids, cinnamic acid, and ergosterol as cosmeceutical ingredients: Stabilization by microencapsulation to ensure sustained bioactivity. *Microchem. J.* **2019**, *147*, 469–477. DOI: 10.1016/j.microc.2019.03.059

Turiel, E.; Martín-Esteban, A. Molecularly imprinted polymers for sample preparation: A review. *Anal. Chim. Acta* **2010**, *668*(2), 87–99. https://doi.org/10.1016/j.aca.2010.04.019

Turkevich, J.; Stevenson, P.C.; Hillier, J. A study of the nucleation and growth processes in the synthesis of colloidal gold. *Discussions of the Faraday Society* **1951**, *11*, 55–75. https://doi.org/10.1039/df9511100055

Vié, V.; Legardinier, S.; Chieze, L.; Le Bihan, O.; Qin, Y.; Sarkis, J.; Hubert, J.F.; Renault, A.; Desbat, B.; Le Rumeur, E. Specific anchoring modes of two distinct dystrophin rod sub-domains interacting in phospholipid Langmuir films studied by atomic force microscopy and PM-IRRAS. *Biochim. Biophys. Acta* **2010**, *1798*(8), 1503–1511. https://doi.org/10.1016/j.bbamem.2010.04.005

Vié, V.; Mau, N.V.; Lesniewska, E.; Goudonnet, J.P.; Heitz, F.; Le Grimellec, C. Distribution of Ganglioside GM1 between two-component, two-phase phosphatidylcholine monolayers. *Langmuir* **1998**, *14*, 4574–4583. https://doi.org/10.1021/la980203p

Vishwanath, M.S.; Swamy, B.E.K.; Vishnumurthy, K.A. Electrochemical detection of bisphenol A in the presence of catechol and hydroquinone at copper oxide modified carbon paste electrode. *Mater. Chem. Phys.* **2022**, *289*, 126443. https://doi.org/10.1016/j.matchemphys.2022.126443

Wang, S.; Xia, P.; Wang, S.; Liang, J.; Sun, Y.; Yue, P.; Gao, X. Packaging films formulated with gelatin and anthocyanins nanocomplexes: Physical properties, antioxidant activity and its application for olive oil protection. *Food Hydrocolloids* **2019**, *96*, 617–624. DOI:10.1016/j.foodhyd.2019.06.004

Wang, Y.; Chen, Z.H. Bioinformatics and enzymatics investigation of Trametes laccase for optical biosensing application. *J. Mater. Sci.* **2019**, *54*, 4970–4983. https://doi.org/10.1007/s10853-018-03187-9

Wang, Y.; Du, H.; Xie, M.; Ma, G.; Yang, W.; Hu, Q.; Pei, F. Characterization of the physical properties and biological activity of chitosan films grafted with gallic acid and caffeic acid: A comparison study. *Food Packag. Shelf Life* **2019**, *22*, 100401. DOI: 10.1016/j.fpsl.2019.100401

Wang, Y.; Wu, N.; Chen, Z.-H. Insight of the optical property of laccase during polymeric formation for application in real-time biosensing. *J. Mater. Sci.* **2021**, *56*, 14368–14380. https://doi.org/10.1007/s10853-021-06186-5

Weber, G. Uses of fluorescence in biophysics: some recent developments. *Annu Rev Biophys Bioeng*. **1972**, *1*, 553-70. https://doi.org/10.1146/annurev.bb.01.060172.003005

Williams, R.T; Bridges, J.W. Fluorescence of solutions: a review. *J Clin Pathol*. **1964**, *17*(4), 371-94. https://doi.org/10.1136/jcp.17.4.371

Wolter, O.; Bayer, T.; Greschner, J. Micromachined silicon sensors for scanning force microscopy. *J. Vac. Sci. Technol. B* **1991**, *9*(2), 1353–1357. https://doi.org/10.1116/1.585195

World Health Organization (WHO). Guidelines for Drinking-Water Quality, 4th ed.; WHO: Geneva, Switzerland, 2017. Available online: http://www.who.int/water_sanitation_health/publications/drinking-water-quality-guidelines-4-including-1st-addendum/en/ (accessed on 15 April 2025).

Wu, H.W.; Chen, M.L.; Shou, D.; Zhu, Y. Determination of Resorcinol and Phloroglucinol in Environmental Water Samples Using Ion Chromatography with Chemiluminescence Detection. *Chinese J. Anal. Chem.* **2012**, *40*, 1747–1751. https://doi.org/10.1016/S1872-2040(11)60588-4

Wu, J.; Zhang, L.; Huang, F.; Ji, X.; Dai, H.; Wu, W. Surface enhanced Raman scattering substrate for the detection of explosives: Construction strategy and dimensional effect. *J. Hazard. Mater.* **2020**, *387*, 121714. https://doi.org/10.1016/j.jhazmat.2019.121714

Wu, N.; Dai, J.; Micale, F.J. Dynamic surface tension measurement with a dynamic Wilhelmy plate technique. *J. Colloid Interface Sci.* **1999**, *215*(2), 258–269. https://doi.org/10.1006/jcis.1999.6270

Xu, F. Oxidation of Phenols, Anilines, and Benzenethiols by Fungal Laccases: Correlation between Activity and Redox Potentials as Well as Halide Inhibition. *Biochemistry* **1996**, *35*, 7608–7614. https://doi.org/10.1021/bi952971a

Xu, Y.; Huang, T.; Wang, S.; Meng, M.; Yan, Y. SiO_2-coated molecularly imprinted sensor based on Si quantum dots for selective detection of catechol in river water. *J. Environ. Chem. Eng.* **2022**, *10*, 106850. https://doi.org/10.1016/j.jece.2021.106850

Yan, F.; Vo-Dinh, T. Surface-enhanced Raman scattering detection of chemical and biological agents using a portable Raman integrated tunable sensor. *Sens. Actuators B Chem.* **2007**, *121*, 61–66. https://doi.org/10.1016/j.snb.2006.09.032

Yaropolov, A.I.; Skorobogat'ko, O.V.; Vartanov, S.S.; Varfolomeyev, S.D. Laccase. *Appl. Biochem. Biotechnol.* **1994**, *49*, 257–280. https://doi.org/10.1007/BF02783061

Yoshida, H. LXIII.-Chemistry of Lacquer (Urushi). Part I. Communication from the Chemical Society of Tokio. *J. Chem. Soc. Trans.* **1883**, *43*, 472–486. https://doi.org/10.1039/CT8834300472

Yue, X.Y.; Zhu, W.X.; Ma, S.Y.; Yu, S.X.; Zhang, Y.H.; Wang, J.; Wang, Y.R.; Zhang, D.H.; Wang, J.L. Highly sensitive and selective determination of tertiary butylhydroquinone in edible oils by competitive reaction induced "On-Off-On" fluorescent switch. *J. Agric. Food Chem.* **2016**, *64*(3), 706–713. https://doi.org/10.1021/acs.jafc.5b05340

Zacharioudaki, D.-E.; Fitilis, I.; Kotti, M. Review of fluorescence spectroscopy in environmental quality applications. *Molecules* **2022**, *27*, 4801. https://doi.org/10.3390/molecules27154801

Zasadzinski, J.A.; Viswanathan, R.; Madsen, L.; Garnaes, J.; Schwartz, D.K. Langmuir-Blodgett films. *Science* **1994**, *263*, 1726–1733. https://doi.org/10.1126/science.8134836

Zeng, P.; Chen, X.; Qin, Y.R.; Zhang, Y.H.; Wang, X.P.; Wang, J.Y.; Ning, Z.X.; Ruan, Q.J.; Zhang, Y.S. Preparation and characterization of a novel colorimetric indicator film based on gelatin/polyvinyl alcohol incorporating mulberry anthocyanin extracts for monitoring fish freshness. *Food Res. Int.* **2019**, *126*, 108604. DOI: 10.1016/j.foodres.2019.108604

Zhang, W.; Wang, W.; Wang, J.; Shen, G.; Yuan, Y.; Yan, L.; Tang, H.; Wang, W. Isolation and characterization of a novel laccase for lignin degradation, LacZ1. *Appl. Environ. Microbiol.* **2021**, *87*, e0135521. https://doi.org/10.1128/AEM.01355-21

Zhang, Z.; Shen, A. Fluorescence and phosphorescence spectroscopies and their applications in gem characterization. *Minerals* **2023**, *13*, 626. https://doi.org/10.3390/min13050626

Zhong, C.J.; Han, L.; Maye, M.M.; Lou, J.; Kariuki, N.N.; Jones Jr, W.E. Atomic scale imaging: A hands-on scanning probe microscopy laboratory for undergraduates. *J. Chem. Educ.* **2003**, *80*, 194. https://doi.org/10.1021/ed080p194

Zhou, Z.P.; Ying, H.Q.; Liu, Y.Y.; Xu, W.Z.; Yang, Y.F.; Luan, Y.; Lu, Y.; Liu, T.S.; Yu, S.; Yang, W.M. Synthesis of surface molecular imprinting polymer on SiO_2-coated CdTe quantum dots as sensor for selective detection of sulfadimidine. *Appl. Surf. Sci.* **2017**, *404*, 188–196. https://doi.org/10.1016/j.apsusc.2017.01.249

Zhu, C.; Palmer, G.M.; Breslin, T.M.; Harter, J.; Ramanujam, N. Diagnosis of breast cancer using fluorescence and diffuse reflectance spectroscopy: A Monte-Carlo-model-based approach. *J. Biomed. Opt.* **2008**, *13*, 034015. https://doi.org/10.1117/1.2931078